NASA/CR-2003-212428

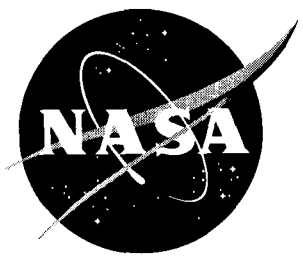

Acoustic Treatment Design Scaling Methods: Phase II Final Report

R. E. Kraft
GE Aircraft Engines, Cincinnati, Ohio

J. Yu, H. W. Kwan, and B. Beer
BFGoodrich, Inc., San Diego, California

A. F. Seybert and P. Tathavadekar
University of Kentucky Research Foundation, Lexington, Kentucky

National Aeronautics and
Space Administration

Langley Research Center
Hampton, Virginia 23681-2199

July 2003

Table of Contents

Summary

Scale model fan rigs that simulate new generation ultra-high-bypass engines at about 1/5 scale are achieving increased importance as development vehicles for the design of low noise aircraft engines. The ability to design, build, and test miniaturized acoustic treatment panels on scale model fan rigs representative of the full scale engine provides not only a cost-saving but an opportunity to optimize the treatment by allowing tests of different designs. To be able to use scale model treatment as a full scale design tool, it is necessary that the impedance of the liner being tested at high sub-scale frequencies be known with confidence. Unavailability of reliable methods of measuring the impedance at high frequencies appears to be the last barrier to being able to use treatment scaling.

This second phase of the Acoustic Treatment Design Scaling Methods Contract has been primarily aimed at developing impedance measurement methods for high frequencies. A normal incidence impedance tube method that extends the upper frequency range to 25,000 Hz. without grazing flow effects has been evaluated. The free field method has been investigated as a potential high frequency technique. The potential of the two-microphone in-situ measurement method was evaluated for impedance measurement in the presence of grazing flow. Difficulties in achieving the high frequency goals were encountered in all methods.

In addition, the time-domain numerical finite difference model for predicting single-degree-of-freedom resonator impedance was upgraded. Results indicate that a re-interpretation of the empirical fluid mechanical models used in the frequency domain model for nonlinear resistance and mass reactance may be required in the time domain. A proposed scale model treatment design that could be tested on the Universal Propulsion Simulator vehicle was defined.

1. Introduction

1.1 Background

The noise suppression provided by acoustic treatment liners in aircraft engine ducts is essential to being able to meet aircraft flyover noise regulations. Testing to validate the performance of acoustic treatment design concepts is an integral part of the suppression system design process. The cost of building and testing treatment designs on full scale engines, however, is prohibitive, and designers are seldom afforded the luxury of more than one attempt at designing and testing the final design that will be used in production.

Scale model fan rigs that simulate new generation ultra-high-bypass engines at about 1/5 scale are achieving increased importance as development vehicles for the design of low noise aircraft engines. Testing at small scale allows the tests to be performed in existing anechoic wind tunnels, which provides an accurate simulation of the important effects of aircraft forward motion on the noise generation. The ability to design, build, and test miniaturized acoustic treatment panels on scale model fan rigs representative of the full scale engine provides not only a cost-saving but an opportunity to optimize the treatment by allowing tests of different designs. To be able to use scale model treatment as a full scale design tool, it is necessary that the designer be able to translate the scale model design and performance to an equivalent full scale design with confidence.

The GEAE Universal Propulsion Simulator (UPS), shown in cross-section in Figure 1-1, is a typical scale model fan rig[1]. The model has the capability of incorporating treatment panels in the inlet duct, fan frame area, and exhaust duct. The treatment is accommodated by removable panels, minimizing hardware cost and configuration change time.

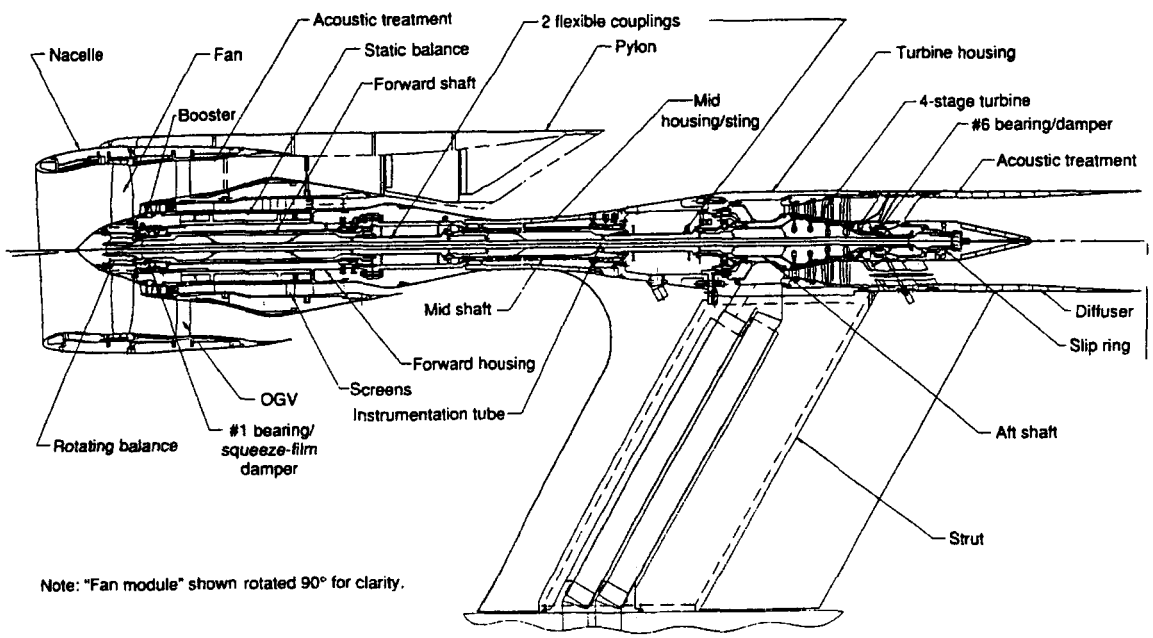

Figure 1-1. Schematic of UPS Scale Model Fan Simulator layout

The key to being able to use sub-scale acoustic treatment results for design and development of full scale liners is the acoustic treatment impedance parameter. Theoretically, the suppression obtained at a full scale frequency for a given treatment impedance value should be the same as that obtained with the same impedance value at the corresponding scaled frequency in the scale model. At that frequency, at least, the impedance design parameter transfers directly from sub-scale to full scale.

When testing acoustic treatment on sub-scale model vehicles, it would be desirable to achieve the same treatment suppression as a function of scaled frequency that would be obtained on the full scale engine. This requires that the source generation characteristics, the engine geometry, and the acoustic impedance scale directly with frequency over the full frequency range of interest. Although sub-scale fan rigs are believed to represent the source characteristics and duct geometry with adequate validity, the treatment impedance representation presents unique problems.

The acoustic impedance for conventionally designed acoustic treatment panels does not scale directly with geometric length and frequency, due to second-order effects. One cannot simply geometrically "shrink" a full scale treatment design and expect the impedance at the scaled frequency to be the same as that at full scale. While the sub-scale treatment can be designed to achieve any impedance at a single frequency, it may not have the same impedance spectrum over the scaled frequency range as the equivalent full scale liner does over its corresponding range.

Thus, the particular impedance characteristics of the sub-scale liner under its particular operating conditions must be accommodated for treatment scaling to be a successful design tool. The key is being able to know what acoustic impedance has been obtained as a function of frequency in the scale model with sufficient assurance that the impedance values can be transferred to the full scale design, if not the physical treatment design parameters. To achieve this, improved impedance models and measurement methods are needed to be able to determine acoustic impedance accurately at high frequencies.

1.2 Synopsis of Prior Study

The primary objective of the overall program was to develop methods that will allow scale model fan rigs to be successfully used as acoustic treatment design tools. The program focused on finding methods to extend the upper limit of the frequency range of impedance prediction models and acoustic impedance measurement methods for sub-scale treatment liner designs The upper limit of impedance measurement for full scale treatment panels has, in the past, been in the range of 6000 Hz. The first phase of the program had as a goal doubling the upper limit of impedance measurement from 6kHz to 12kHz. The program utilized combined analytical and experimental methods to achieve the objectives. The prior phase effort was reported in a series of NASA Contractor Report Volumes, References 2 to 6.

Analytical impedance models were developed to provide a theoretical basis for understanding flow phenomena pertinent to the behavior of treatment panel designs at small scales and the significant differences from full-scale behavior. Laboratory testing conducted included normal incidence impedance measurements, DC flow resistance measurements, and in-duct transmission loss measurements. In some cases, the testing was proven to be inadequate for treatment scaling purposes. The goal of increasing the upper frequency measurement limit for acoustic impedance to above 12,000 Hz was achieved in the case of no grazing flow, but attempts to measure impedance at high frequencies in the presence of grazing flow were unsuccessful. Analytical impedance prediction models were developed that show excellent correlation with the measured normal incidence impedance beyond the 12,000 Hz goal, up to about 13,000 Hz.

A set of guidelines for the utilization of scale model treatment as a full scale engine treatment design tool was established. A procedure for incorporating sub-scale treatment effects into the treatment design optimization was proposed.

1.3 Objectives of Current Study

The major barrier remaining for the ability to successfully implement scale-models as tools for design of full-scale engine acoustic treatment is that of being able to measure the impedance of scaled treatment liners, with and without the effects of grazing flow, up to the highest frequency of interest for the scale model. The treatment impedance is the key scaling

parameter that must be matched at corresponding scale-model and full-scale frequencies for the treatment design. The exact construction of the scaled treatment is not critical, as long at its impedance is known. Even if analytical impedance prediction models are available, these models must be validated by experimental measurements.

Without reliable measurements, one can never be sure precisely what impedance was operating to give a measured suppression at a particular frequency in a treated scale-model vehicle test. For this reason, this phase of the program focused primarily on an exploratory effort to develop advanced impedance measurement methods to achieve the high frequency requirement.

In the first phase of this study, reported in References 2 to 6, methods were developed to extend the impedance measurement frequency for the normal incidence impedance tube method to about 13,000 Hz. It is the objective of this second phase study to double that limit to above 25,000 Hz, for liner impedances without the effects of grazing flow. Methods were also evaluated to attempt to extend the measurement of impedance with the effects of grazing flow to 12,000 Hz.

For the second phase of this program tasks aimed at evaluating the feasibility, problems, and methods of treatment scaling were the following:

1. Develop a multi-modal normal incidence tube impedance measurement method that extends the measurement frequency up to 25,000 Hz.
2. Develop a free-field method to measure impedance of a surface at high frequencies.
3. Identify a measurement concept to account for grazing flow effects.
4. Apply an advanced numerical finite difference scheme to the time-domain impedance prediction model and evaluate results.
5. Define an acoustic treatment configuration for potential future testing on the UPS vehicle.

Details of the results of studies aimed at achieving these objectives are presented in the following sections of this Contractor's Report. Each section is essentially a self-contained report, and the reader will notice some inconsistencies in format from section to section, for which the authors apologize. Nomenclature will vary from section to section, and is defined locally in the text. References for each section are located at the end of the individual sections.

1.4 Summary of Results

1.4.1 High Frequency Normal Incidence Impedance Measurement Methods

As part of the first phase of this contract, a high-frequency normal incidence impedance tube apparatus was developed using a 1.5 cm tube inner diameter, aimed at measuring impedance up to 13,000 Hz. The subsequent effort was an attempt to extend the range of the impedance measurement method up to about 25,000 Hz. The approach to achieving this goal was to modify the 1.5 cm tube to be able to account for higher order mode propagation in the tube. This was

done by increasing the number of sensors along the length of the tube and developing an advanced data analysis algorithm. A description of the device and the analysis used in its operation is included. Problems were experienced in the operation of the tube, and the diagnosis of these problems was unable to be completed within the scope of the program.

1.4.2 Evaluation of Free-Field Method of Determining Acoustic Impedance

In this task the free field method was evaluated for measuring the acoustical impedance of scale-model aircraft engine liner treatments at high frequencies. Such treatments are used in the Ultra-High-Bypass Ratio Propulsion Simulator (UPS) where the frequencies may extend to 25 kHz. A literature search revealed that none of the existing methods for the measurement of impedance, including the free field method, has been used above approximately 8 kHz. A simulation of the free field method using the boundary element method was conducted to determine important experimental parameters such as sample size, source location, and microphone location and size. The simulation showed that at 25 kHz the sample size should be approximately 12 inches square or larger in order to establish a uniform sound field in the vicinity of the microphones. The simulation further showed that the microphones should be no larger than approximately 1/16 inches in diameter to avoid distortion of the sound field due to diffraction at 25 kHz. An experimental test apparatus was constructed based on the results of the simulation. The impedance and absorption coefficient of a single degree of freedom liner and of a sample of DynaRohr® liner were measured in the 0-7 kHz range. Measurements of impedance were made in both a hemi-anechoic chamber and in a typical laboratory room. Impedance data in an impedance tube compared favorably to data measured using the free field method.

1.4.3 Evaluation of In-Situ Methods for Measurement of Acoustic Impedance

The two-microphone "in-situ" measurement technique is designed to measure the acoustic impedance of locally reacting, single-degree-of-freedom (SDOF), resonator type, acoustic liners. This technique has been used, with some success, to measure the effects of grazing flow on the acoustic impedance of full-scale SDOF liners with perforated face sheets. The work presented in this report was undertaken to evaluate the feasibility of this method for measuring acoustic impedance of scaled acoustic treatment at high frequencies. The results of an analysis of the measurement uncertainties show that the accuracy of the measured impedance is very sensitive to the accuracy of the phase difference between the acoustic pressures measured at the face sheet and the back wall. Results of preliminary experiments with this method have confirmed the difficulties predicted by the analysis mentioned above. Consequently, this technique is considered practically unsuitable for application at high frequencies (much greater than 6000 Hz.).

1.4.4 Time-Domain Numerical Method to Predict Acoustic Impedance

The objective of this task was to develop a time-domain numerical model that represents a simple, isolated single-degree-of-freedom (SDOF) acoustic treatment hexcell cavity covered by a perforated faceplate. The time-domain impedance prediction program ZORF has been upgraded by incorporating the dispersion-relation-preserving 7-point stencil finite difference, 4-

level time marching scheme of Tam. The upgrade did not materially change the results obtained from the simpler 3-point stencil finite-difference scheme used previously, but it does converge using far fewer grid points per wavelength and gives confidence that the entire method is computing correctly. In order to obtain agreement between the time-domain impedance prediction method, the frequency-domain method, and the measured data, it is necessary to make adjustments to the effects of nonlinear resistance and mass reactance for the time-domain model. At present, these adjustments to the resistance and reactance parameters must be made by hindsight, and further effort is needed to provide advanced fluid mechanical models for resistance and mass reactance for application to the time-domain prediction. The time domain model has been shown to be capable of closely predicting the measured impedance of single-degree-of-freedom perforated plate resonators up to frequencies of 13,000 Hz. The time-domain model does predict variations of acoustic impedance in spectral shape, although it has not been proven authoritatively that the prediction matches spectral variations in the measured data. It is concluded that the time-domain model meets the objective of correctly determining the effects of variations in the spectral shape and level of the excitation acoustic pressure on the nonlinear resonator impedance.

1.4.5 UPS Nacelle Liner Design

Three different fan configurations were considered for the GEAE Universal Propulsion Simulator (UPS) nacelle acoustic treatment design. The first fan configuration was the baseline, which has high vane count and unswept vanes. The second fan configuration has low vane count and unswept vanes. The last fan configuration has low vane count and swept vanes. The first objective of this task was to demonstrate an analytical approach to design the UPS nacelle acoustic treatment. The second objective was to establish the correlation between the full-scale liner and its 1/5 sub-scale liner under design conditions. Due to limitations in program scope, only the baseline inlet was picked as a demonstration candidate. A two-layer, double-degree-of-freedom (DDOF) 1/5 scale liner design was determined that can possibly be fabricated successfully. The DDOF design would match the full-scale design impedance over a wide frequency range between blade-passing frequency (BPF) and the third harmonic (3BPF). As an alternative treatment design and scaling approach, two separate single layer liner designs with wiremesh facesheets were determined that could provide useful design information in terms of reactance variation over a range of frequencies from BPF to 3BPF, for an arbitrary scale factor.

1.4.6 Assessment of High Frequency Impedance Measurement Methods

None of the impedance measurement methods investigated were able to achieve the goals of measuring impedance at high frequencies with a high degree of accuracy or reliability. It was concluded that the two-microphone in-situ method for measuring impedance with grazing flow would encounter extreme difficulties above about 6000 Hz. Currently, the most reliable method for treatment scaling would require the use of wiremesh single-degree-of-freedom liners limited to a sub-scale upper frequency of around 12,000 Hz. The development of methods to measure impedance at higher frequencies may be conceivable, but it will require an extreme degree of precision in the technique and apparatus, such that the measurement may be beyond the capabilities of existing industrial acoustics laboratories.

1.5 References

1. Balan, C. and Hoff, G. E., "Turbofan Propulsion Simulator", Aerospace Engineering, August, 1993, pp. 11-16.
2. Kraft, R. E. and Yu, J., "Acoustic Treatment Design Scaling Methods. Volume 1: Overview, Results, and Recommendations", NASA CR-1999-209120/VOL. 1, July, 1997.
3. Kraft, R. E., Yu, J., and Kwan, H. W., "Acoustic Treatment Design Scaling Methods. Volume 2: Advanced Treatment Impedance Models for High Frequency Ranges", NASA CR-1999-209120/VOL. 2, July, 1997.
4. Yu, J., Kwan, H. W., Echternach, D. K., Kraft, R. E., and Syed, A. A., "Acoustic Treatment Design Scaling Methods. Volume 3: Test Plans, Hardware, Results, and Evaluation", NASA CR-1999-209120/VOL. 3, July, 1997.
5. Kraft, R. E., "Acoustic Treatment Design Scaling Methods. Volume 4: Numerical Simulation of the Nonlinear Acoustic Impedance of a Perforated Plate Single-Degree-of-Freedom Resonator Using a Time-Domain Finite Difference Method", NASA CR-1999-209120/VOL. 4, July, 1997.
6. Chien, W. E., and Kraft, R. E., "Acoustic Treatment Design Scaling Methods. Volume 5: Analytical and Experimental Data Correlation", NASA CR-1999-209120/VOL. 5, July, 1997.

2. High Frequency Normal Incidence Impedance Measurement Methods

2.1 Mode Propagation in the 1.5 cm Diameter Impedance Tube

As part of the first phase of this contract, a high-frequency normal incidence impedance tube apparatus was developed using a 1.5 cm tube inner diameter, aimed at measuring impedance up to 13,000 Hz[1]. As described in the report, the device was successful in measuring impedance up to the objective frequency.

This effort is an attempt to extend the range of the impedance measurement method up to about 25,000 Hz. The approach to achieving this goal is to modify the 1.5 cm tube to be able to account for higher order mode propagation in the tube. This is done by increasing the number of sensors along the length of the tube and developing an advanced data analysis algorithm.

2.2 Cut-On Modes Analysis

The first cut-on mode is a plane wave mode (0,0). It will propagate unattenuated in the tube over all frequency ranges. The second cut-on mode is the first order circumferential mode (1,0). It will propagate in the tube at frequencies above 13.4 kHz (13461.4 Hz at room temperature). The third cut-on mode is the second radial mode (0,1). It will propagate in the tube at frequencies above 28 kHz (28014.7 Hz at room temperature).

The formula to calculate cut-on mode frequencies can be determined by a simple equation $kR \geq \lambda_{mn}$. Where $k = 2\pi f/c$ is the wave number (f is frequency and c is sound speed), R is the tube radius, and λ_{mn} is the wave mode eigenvalue. From the Bessel function solutions, λ_{00} is equal to 0.0, λ_{10} is equal to 1.84118, and λ_{01} is 3.83171. The propagation constant k_{00} and k_{10} can be defined as

$$k_{00} = k\left((1-(\lambda_{00} / kR)^2\right)^{1/2} = k \tag{2-1}$$

$$k_{10} = k\left((1-(\lambda_{10} / kR)^2\right)^{1/2} = k\left((1-(1.84118 / kR)^2\right)^{1/2} \tag{2-2}$$

and

$$k_{01} = k\left((1-(\lambda_{01} / kR)^2\right)^{1/2} = k\left((1-(3.83171 / kR)^2\right)^{1/2} \tag{2-3}$$

Figure 2-1 shows the impedance measurement methods using two-microphone and four-microphone techniques.

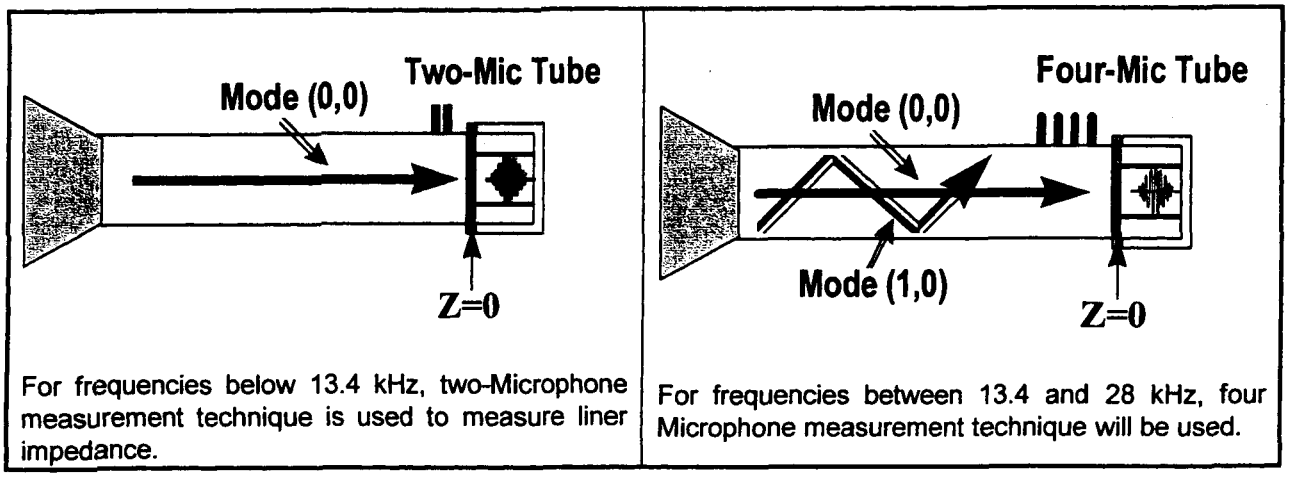

For frequencies below 13.4 kHz, two-Microphone measurement technique is used to measure liner impedance.

For frequencies between 13.4 and 28 kHz, four Microphone measurement technique will be used.

Figure 2-1 Two-microphone and four-microphone impedance measurements for 1.5 cm impedance tube

2.3 Analytical Model For Two-Microphone Method

Sound modes that propagate in the 1.5 cm diameter tube at frequencies under 13.4 kHz can be expressed as follows:

$$P_t = (A_{00}\exp(-ikz)+B_{00}\exp(ikz)) \quad (2\text{-}4)$$

$$V_t = (A_{00}\exp(-ikz)-B_{00}\exp(ikz))/\rho c \quad (2\text{-}5)$$

where,

P_t is In-tube total sound pressure (plane wave) at location z

V_t is In-tube total sound particle velocity at location z

The liner normal incidence impedance is defined as the ratio of plane wave sound pressure to the particle velocity at liner surface, z = 0. Let the reflection coefficient $R_0 = B_{00}/A_{00}$, then the impedance can be expressed as follows:

$$Z_o/\rho c = (P_t / (\rho c\, V_t))_{z=0} = (A_{00}+B_{00}) / (A_{00}-B_{00}) = (1+R_{00})/ (1-R_{00}) \quad (2\text{-}6)$$

If pressure P_t and microphone position z are known parameters, then it requires two microphones, at locations z_1, and z_2, to generate two equations to solve two unknown variables, A_{00}, and B_{00}. These two equations are expressed as follows:

$$P_{t1} = (A_{00}\exp(-ikz_1)+B_{00}\exp(ikz_1)) = A_{00}(\exp(-ikz_1)+R_{00}\exp(ikz_1)) \quad (2\text{-}7)$$

$$P_{t2} = (A_{00}\exp(-ikz_2)+B_{00}\exp(ikz_2)) = A_{00}(\exp(-ikz_2)+R_{00}\exp(ikz_2)) \quad (2\text{-}8)$$

Eliminate A_0 between Equation (2-7) and Equation (2-8) to yield

$$P_{t1}/P_{t2} = (\exp(-ikz_1)+R_{00}\exp(ikz_1)) / (\exp(-ikz_2)+R_{00}\exp(ikz_2)) \quad (2\text{-}9)$$

Rearranging Equation (2-9), the reflection coefficient R_{00} can then be obtained by

$$R_{00} = [(P_{t1}/P_{t2})\exp(-ikz_2) - \exp(-ikz_1)] / [-(P_{t1}/P_{t2})\exp(ikz_2) + \exp(ikz_1)] \quad (2\text{-}10)$$

Substitute Equation (2-10) into (2-6) to yield

$$Z_o/\rho c = i[-\sin(kz_1) + (P_{t1}/P_{t2})\sin(kz_1)] / [-\cos(kz_1) + (P_{t1}/P_{t2})\cos(kz_1)] \quad (2\text{-}11)$$

A_{00} can be obtained by substituting Equation (2-10) into Equation (2-7) or (2-8). The absolute values of plane wave mode sound pressure and particle velocity at liner surface (z=0) can then be calculated by

$$|P_t|_{z=0} = |A_{00}(1+R_{00})| \quad (2\text{-}12)$$

and

$$|V_{00}|_{z=0} = |A_{00}(1-R_{00})/\rho c| \quad (2\text{-}13)$$

If the tube size were reduced to 0.75 cm, then, theoretically, the two-microphone impedance measurement method could extend to frequencies up to 26.8 kHz.

2.4 Analytical Model for Four-Microphone Method

2.4.1 Acoustic Propagation in the Normal Incidence Tube

Sound modes propagating in the 1.5 cm diameter tube at the frequency range between 13.4 kHz to 28 kHz can be expressed as follows:

$$P_t = P_{00} + P_{10} = (A_{00}\exp(-ik_{00}z)+B_{00}\exp(ik_{00}z)) + (A_{10}\exp[(-ik_{10}z)+m\phi]+B_{10}\exp[(ik_{10}z)+m\phi]) \quad (2\text{-}14)$$

for the acoustic pressure, and

$$V_t = V_{00} + V_{10} = A_{00}\exp(-ik_{00}z)-B_{00}\exp(ik_{00}z))/\rho c + (A_{10}\exp[(-ik_{10}z)+m\phi]-B_{10}\exp[(ik_{10}z)+m\phi])/\rho c \quad (2\text{-}15)$$

for the acoustic velocity, where

P_t is the total sound pressure at location z

V_t is total sound particle velocity at location z

P_{00} and P_{10} are mode (0,0) and mode (1,0) sound pressures at location z

V_{00} and V_{10} are mode (0,0) and mode (1,0) sound particle velocities at location z

k_{00} and k_{10} are mode (0,0) and mode (0,1) propagation constants from Equation (2-3)

$m\phi$ is higher order circumferential mode. For the first higher mode, $m = \pm 1$

The liner normal incidence impedance is defined as the ratio of plane wave sound pressure to the particle velocity at liner surface z = 0. This can be expressed as follows:

$$Z_o/\rho c = (P_{00} / (\rho c\, V_{00})_{z=0} = (A_{00}+B_{00}) / (A_{00}-B_{00}) \quad (2\text{-}16)$$

The reflection coefficient is defined by

$$R_{00} = B_{00}/A_{00} \quad (2\text{-}17)$$

Substituting the reflection coefficient into Equation (2-5) yields

$$Z_o/\rho c = (1+R_{00}) / (1-R_{00}) \quad (2\text{-}18)$$

2.4.2 Four Microphone Technique

If pressure P_t and microphone position z are known parameters, then it requires four microphones locations z_1, z_2, z_3, and z_4 to generate four equations to solve four unknown variables, A_{00}, B_{00}, A_{10}, and B_{10}. Let the four microphones be located in a straight line parallel to the tube axis and arbitrarily set the microphone circumferential position to $\phi = 0$. Then, these four equations can be expressed as follows:

$$P_{t1} = (A_{00}\exp(-ik_{00}z_1)+B_{00}\exp(ik_{00}z_1)) + (A_{10}\exp(-ik_{10}z_1)+B_{10}\exp(ik_{10}z_1)) \quad (2\text{-}19)$$

$$P_{t2} = (A_{00}\exp(-ik_{00}z_2)+B_{00}\exp(ik_{00}z_2)) + (A_{10}\exp(-ik_{10}z_2)+B_{10}\exp(ik_{10}z_2)) \quad (2\text{-}20)$$

$$P_{t3} = (A_{00}\exp(-ik_{00}z_3)+B_{00}\exp(ik_{00}z_3)) + (A_{10}\exp(-ik_{10}z_3)+B_{10}\exp(ik_{10}z_3)) \quad (2\text{-}21)$$

$$P_{t4} = (A_{00}\exp(-ik_{00}z_4)+B_{00}\exp(ik_{00}z_4)) + (A_{10}\exp(-ik_{10}z_4)+B_{10}\exp(ik_{10}z_4)) \quad (2\text{-}22)$$

We make the following simplifications in notation:

$\exp(-ik_{00}z_1) = f_{01}$; $\exp(-ik_{00}z_2) = f_{02}$; $\exp(-ik_{00}z_3) = f_{03}$; $\exp(-ik_{00}z_4) = f_{04}$;

$\exp(-ik_{10}z_1) = f_{11}$; $\exp(-ik_{10}z_2) = f_{12}$; $\exp(-ik_{10}z_3) = f_{13}$; $\exp(-ik_{10}z_4) = f_{14}$;

$\exp(ik_{00}z_1) = g_{01}$; $\exp(ik_{00}z_2) = g_{02}$; $\exp(ik_{00}z_3) = g_{03}$; $\exp(ik_{00}z_4) = g_{04}$;

$$\exp(ik_{10}z_1) = g_{11}; \qquad \exp(ik_{10}z_2) = g_{12}; \qquad \exp(ik_{10}z_3) = g_{13}; \qquad \exp(ik_{10}z_4) = g_{14};$$

We eliminate the A_{10} term ($A_{10}\ f_{11}\ f_{12}$) between Equation (2-19) and Equation (2-20) to yield

$$P_{t1}\ f_{12} - P_{t2}\ f_{11} = A_{00}\ (f_{01}\ f_{12} - f_{02}\ f_{11}) + B_{00}\ (g_{01}\ f_{12} - g_{02}\ f_{11}) + B_{10}\ (g_{11}\ f_{12} - g_{12}\ f_{11}) \qquad (2\text{-}23)$$

A similar process is used to eliminate the term $A_{10}\ f_{13}\ f_{14}$ between Equations (2-21) and (2-22); the term $A_{10}\ f_{11}\ f_{13}$ between Equations (2-19) and (2-21); and the term $A_{10}\ f_{12}\ f_{14}$ between Equations (2-20) and (2-22). The rest of equations can be expressed as follows:

$$P_{t3}\ f_{14} - P_{t4}\ f_{13} = A_{00}\ (f_{03}\ f_{14} - f_{04}\ f_{13}) + B_{00}\ (g_{03}\ f_{14} - g_{04}\ f_{13}) + B_{10}\ (g_{13}\ f_{14} - g_{14}\ f_{13}) \qquad (2\text{-}24)$$

$$P_{t1}\ f_{13} - P_{t3}\ f_{11} = A_{00}\ (f_{01}\ f_{13} - f_{03}\ f_{11}) + B_{00}\ (g_{01}\ f_{13} - g_{03}\ f_{11}) + B_{10}\ (g_{11}\ f_{13} - g_{13}\ f_{11}) \qquad (2\text{-}25)$$

$$P_{t2}\ f_{14} - P_{t4}\ f_{12} = A_{00}\ (f_{02}\ f_{14} - f_{04}\ f_{12}) + B_{00}\ (g_{02}\ f_{14} - g_{04}\ f_{12}) + B_{10}\ (g_{12}\ f_{14} - g_{14}\ f_{12}) \qquad (2\text{-}26)$$

The next step is to eliminate all terms with the B_{10} variable between Equation (2-23) and Equation (2-24), and Equation (2-25) and Equation (2-26). The new equations become:

$$\begin{aligned}(P_{t1}\ f_{12} - P_{t2}\ f_{11})\ (g_{13}\ f_{14} - g_{14}\ f_{13}) - (P_{t3}\ f_{14} - P_{t4}\ f_{13})\ (g_{11}\ f_{12} - g_{12}\ f_{11}) \\ = A_{00}\{[(f_{01}\ f_{12} - f_{02}\ f_{11})\ (g_{13}\ f_{14} - g_{14}\ f_{13}) - (f_{03}\ f_{14} - f_{04}\ f_{13})\ (g_{11}\ f_{12} - g_{12}\ f_{11})] \\ + R_{00}[(g_{01}\ f_{12} - g_{02}\ f_{11})\ (g_{13}\ f_{14} - g_{14}\ f_{13}) - (g_{03}\ f_{14} - g_{04}\ f_{13})\ (g_{11}\ f_{12} - g_{12}\ f_{11})]\}\end{aligned} \qquad (2\text{-}27)$$

and

$$\begin{aligned}(P_{t1}\ f_{13} - P_{t3}\ f_{11})\ (g_{12}\ f_{14} - g_{14}\ f_{12}) - (P_{t2}\ f_{14} - P_{t4}\ f_{12})\ (g_{11}\ f_{13} - g_{13}\ f_{11}) \\ = A_{00}\{[(f_{01}\ f_{13} - f_{03}\ f_{11})\ (g_{12}\ f_{14} - g_{14}\ f_{12}) - (f_{02}\ f_{14} - f_{04}\ f_{12})\ (g_{11}\ f_{13} - g_{13}\ f_{11})] \\ + R_{00}[(g_{01}\ f_{13} - g_{03}\ f_{11})\ (g_{12}\ f_{14} - g_{14}\ f_{12}) - (g_{02}\ f_{14} - g_{04}\ f_{12})\ (g_{11}\ f_{13} - g_{13}\ f_{11})]\}\end{aligned} \qquad (2\text{-}28)$$

We make the following simplifications in notation:

$$D_1 = f_{12}\ (g_{13}\ f_{14} - g_{14}\ f_{13}); \qquad D_2 = f_{11}\ (g_{13}\ f_{14} - g_{14}\ f_{13});$$

$$D_3 = f_{14}\ (g_{11}\ f_{12} - g_{12}\ f_{11}); \qquad D_4 = f_{13}\ (g_{11}\ f_{12} - g_{12}\ f_{11});$$

$$E_1 = f_{13}\ (g_{12}\ f_{14} - g_{14}\ f_{12}); \qquad E_2 = f_{11}\ (g_{12}\ f_{14} - g_{14}\ f_{12});$$

$$E_3 = f_{14}\ (g_{11}\ f_{13} - g_{13}\ f_{11}); \qquad E_4 = f_{12}\ (g_{11}\ f_{13} - g_{13}\ f_{11});$$

$$F_1 = (f_{01}\ f_{12} - f_{02}\ f_{11})\ (g_{13}\ f_{14} - g_{14}\ f_{13}) - (f_{03}\ f_{14} - f_{04}\ f_{13})\ (g_{11}\ f_{12} - g_{12}\ f_{11})$$

$$F_2 = (g_{01}\ f_{12} - g_{02}\ f_{11})\ (g_{13}\ f_{14} - g_{14}\ f_{13}) - (g_{03}\ f_{14} - g_{04}\ f_{13})\ (g_{11}\ f_{12} - g_{12}\ f_{11})$$

$$G_1 = (f_{01} f_{13} - f_{03} f_{11}) (g_{12} f_{14} - g_{14} f_{12}) - (f_{02} f_{14} - f_{04} f_{12}) (g_{11} f_{13} - g_{13} f_{11})$$

$$G_2 = (g_{01} f_{13} - g_{03} f_{11}) (g_{12} f_{14} - g_{14} f_{12}) - (g_{02} f_{14} - g_{04} f_{12}) (g_{11} f_{13} - g_{13} f_{11})$$

and rewrite Equations (2-27) and (2-28) to yield

$$P_{t1} D_1 - P_{t2} D_2 - P_{t3} D_3 + P_{t4} D_4 = A_{00} (F_1 + R_{00} F_2) \quad (2\text{-}29)$$

and

$$P_{t1} E_1 - P_{t3} E_2 - P_{t2} E_3 + P_{t4} E_4 = A_{00} (G_1 + R_{00} G_2) \quad (2\text{-}30)$$

Eliminating the term A_{00} between Equation (2-29) and Equation (2-30) yields

$$(P_{t1} D_1 - P_{t2} D_2 - P_{t3} D_3 + P_{t4} D_4) (G_1 + R_{00} G_2) = (P_{t1} E_1 - P_{t3} E_2 - P_{t2} E_3 + P_{t4} E_4) (F_1 + R_{00} F_2) \quad (2\text{-}31)$$

Rearranging Equation (2-31) yields

$$R_{00} [G_2 (P_{t1} D_1 - P_{t2} D_2 - P_{t3} D_3 + P_{t4} D_4) - F_2 (P_{t1} E_1 - P_{t3} E_2 - P_{t2} E_3 + P_{t4} E_4)] = [F_1 (P_{t1} E_1 - P_{t3} E_2 - P_{t2} E_3 + P_{t4} E_4) - G_1 (P_{t1} D_1 - P_{t2} D_2 - P_{t3} D_3 + P_{t4} D_4)] \quad (32)$$

or

$$R_{00} [P_{t1} (G_2 D_1 - F_2 E_1) - P_{t2} (G_2 D_2 - F_2 E_3) - P_{t3} (G_2 D_3 - F_2 E_2) + P_{t4} (G_2 D_4 - F_2 E_4)] = P_{t1} (F_1 E_1 - G_1 D_1) - P_{t2} (F_1 E_3 - G_1 D_2) - P_{t3} (F_1 E_2 - G_1 D_3) + P_{t4} (F_1 E_4 - G_1 D_4)] \quad (2\text{-}33)$$

Make the additional changes in notation,

$Q_1 = (G_2 D_1 - F_2 E_1)$; $Q_2 = (G_2 D_2 - F_2 E_3)$;

$Q_3 = (G_2 D_3 - F_2 E_2)$; $Q_4 = (G_2 D_4 - F_2 E_4)$

$S_1 = (F_1 E_1 - G_1 D_1)$; $S_2 = (F_1 E_3 - G_1 D_2)$;

$S_3 = (F_1 E_2 - G_1 D_3)$; $S_4 = (F_1 E_4 - G_1 D_4)$

Equation (2-33) can then be further simplified to yield

$$R_{00} = (P_{t1} S_1 - P_{t2} S_2 - P_{t3} S_3 + P_{t4} S_4) / (P_{t1} Q_1 - P_{t2} Q_2 - P_{t3} Q_3 + P_{t4} Q_4) \quad (2\text{-}34)$$

Substitute Equation (2-34) into Equation (2-18) to yield

$$\frac{Z_0}{\rho c} = \frac{1+R_{00}}{1-R_{00}} = \frac{P_{t1}(Q_1+S_1)-P_{t2}(Q_2+S_2)-P_{t3}(Q_3+S_3)+P_{t4}(Q_4+S_4)}{P_{t1}(Q_1-S_1)-P_{t2}(Q_2-S_2)-P_{t3}(Q_3-S_3)+P_{t4}(Q_4-S_4)} \tag{2-35}$$

A_{00} can be obtained by substituting Equation (2-34) into Equation (2-29) or (2-30). The absolute values of plane wave mode sound pressure and particle velocity at liner surface (z = 0) can then be calculated from

$$|P_{00}|_{z=0} = |A_{00}(1+R_{00})| \tag{2-36}$$

and

$$|V_{00}|_{z=0} = |A_{00}(1-R_{00})/\rho c| \tag{2-37}$$

2.5 Two-Microphone Method For In-Situ Acoustic Impedance Measurement

In-situ acoustic impedance measurement, using the two-microphone technique, is another option for liner impedance measurements. If the sample core diameter is not greater than 0.75 cm, then the sample impedance can be measured up to 26 kHz. Figure 2-2 illustrates the technique of the in-situ two-microphone impedance measurement.

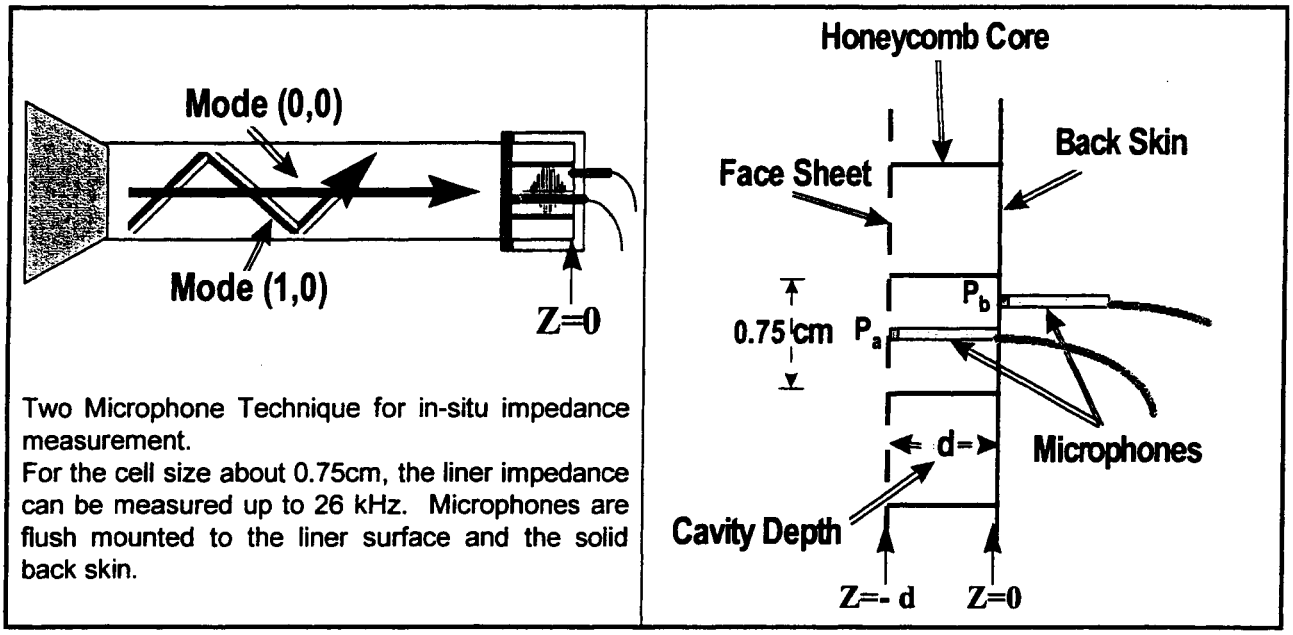

Two Microphone Technique for in-situ impedance measurement.
For the cell size about 0.75cm, the liner impedance can be measured up to 26 kHz. Microphones are flush mounted to the liner surface and the solid back skin.

Figure 2-2 In-situ two-microphone impedance measurement

Let P_a and P_b be the pressure measured by the microphones at the liner facesheet surface and the rear of the cavity, respectively; and let V_a be the particle velocity incident upon the cavity orifice. The normalized impedance at the sample surface is given by

$$\frac{Z}{\rho c} = \left(\frac{P_a}{\rho c V_a} \right)_{z=-d} \tag{2-38}$$

Since P_b is sound pressure measured at the position z=0, the sound pressure P_c inside the cavity can be expressed as:

$$P_C = (0.5\, P_b (\exp(-ikz) + \exp(ikz)) \tag{2-39}$$

and the particle velocity V_c inside the cavity can then be expressed as:

$$V_c = (0.5\, P_b (\exp(-ikz) - \exp(ikz)) / \rho c = -i(P_b \sin(kz)) / \rho c \tag{2-40}$$

At z = -d, particle velocity V_a and V_c are equal. Then V_a can be expressed as:

$$(V_a)_{z=-d} = (V_c)_{z=-d} = i\,(P_b \sin(kd)) / \rho c \tag{2-41}$$

Substitute Equation (2-41) into Equation (2-38) to yield

$$\frac{Z}{\rho c} = \left(\frac{P_a}{\rho c V_a}\right)_{z=-d} = -i\frac{P_a}{P_b \sin(kd)} \tag{2-42}$$

Let ϕ be the phase angle between P_a and P_b. Then this equation can be re-written in the form

$$\frac{Z}{\rho c} = \left(\frac{P_a}{\rho c V_a}\right)_{z=-d} = -\frac{i}{\sin(kd)}\left|\frac{P_a}{P_b}\right| e^{\phi} \tag{2-43}$$

The absolute values of sound pressure and particle velocity at liner surface (z = -d) can then be obtained from $|P_a|$ and $|V_a|_{z=-d}$.

2.6 Instrumentation Setup

After considering the three potential methods discussed in the previous section, BFG decided to design and fabricate a 1.5 cm four-microphone acoustic impedance measuring system. This new system has advantages over the other two methods.

The traditional two-microphone normal incidence tube method would require a tube diameter of approximately 0.75 cm for the impedance measurement up to about 25,000 Hz., which imposes difficulty on hardware design and test sample fabrication. The in-situ method permits use of a larger size tube for the impedance measurement; however, it limits the sample core size. In addition, it is very difficult to mount microphones inside the core. At the same time, the measurement is restricted to a very narrow area.

The new four-microphone method has issues concerning higher order modes. However, plane wave impedance data can be obtained, and higher modes eliminated, with proper hardware set-up and mathematical data processing. BFG has developed a data acquisition system for this four-microphone impedance measuring device. The frequency range of the test is from 5000 Hz to 20,000 Hz with 100 Hz band-width. The design procedure, hardware set-up, and initial check of the system are described in the following sections.

2.6.1 General Design Considerations

ASTM-E1050-90 was used as a guideline to design the high frequency acoustic impedance tube. Several issues that influence the impedance measurement were addressed.

- The tube's wall should be massive and sufficiently rigid so that sound energy transmission through the wall is negligible.
- For a plane wave mode and two microphones only, the diameter of tube (in cm) should be $d < 0.586(c_0/f_m)$, where f_m is the highest frequency of interest in Hz, and c_0 is the speed of sound (cm/s).

- The length of tube should be as short as possible to maintain the required signal-to-noise ratio and to reduce added absorption, yet must be long enough such that the sample is not in the nearfield of the acoustic drivers.
- For the two microphone method, the microphone spacing should be $s << (c_0/2f_m)$.
- Spacing between the test specimen and the nearest microphone should be minimized to maintain the required signal-to-noise ratio and to reduce added absorption, yet must remain large enough such that higher order cut-off modes do not affect measurements..
- In a circular tube, the distance from the test specimen to the nearest microphone should be at least one tube diameter.
- Microphones should be mounted flush with the interior surface of the tube.

As described in the Section 2.2, "Cut-On Modes Analysis", the 1.5 cm diameter impedance tube can support the first three cut-on modes, i.e., the plane wave mode (0, 0) in all frequency ranges, the first order circumferential mode (1, 0) at frequencies above 13.4 kHz, and the second radial mode (0, 1) - at frequencies above 28 kHz. Therefore, only two modes, the plane wave mode and the first order circumferential mode (1, 0), can propagate in the 1.5 cm diameter impedance tube at the frequencies less than 28 kHz. As discussed in the Section 2.4 titled "Analytical Model for Four-microphone Method', four microphones are required to generate the four equations necessary to derive the acoustic impedance of the test sample.

Therefore, the specifications of the impedance tube were determined as follows:

- upper limit of frequency: 20,000 Hz, (due to the bandwidth limitation of a spectrum analyzer),
- diameter of the tube: 1.5 cm,
- length of the tube: 15 cm,
- size of the microphone (pressure transducer): 0.16 cm,
- random noise source: a 40 watt compression driver, and
- material of the tube: stainless steel.

2.6.2 Equipment and Hardware

Figure 2-3 shows a schematic of the new impedance tube measurement system. The tube has thirteen (13) equally spaced holes, since this configuration permits different combinations of four microphone spacings and their distance to the test specimen. A photograph of the installation of the microphones in the impedance tube is shown in Figure 2-4. A compression driver, shown in Figure 2-5, is attached to the tube without a horn and a transition duct, because the opening (1.6 cm in diameter) of the compression driver matches the tube diameter. A signal amplifier for the microphones is mounted on a wooden board which also carries the impedance tube.

Figure 2-6 shows the fully assembled prototype four-microphone high frequency impedance measuring system. A Tektronix 2630 Fourier Analyzer with four (4) input channels and a signal generator was used. The signal generator output is filtered by a bandpass filter and then fed to the compression driver to generate a broadband noise. The frequency response of the analyzer is limited to 20 kHz, which establishes the upper limit for the four microphone impedance measuring system. The Toshiba labtop computer was used for data acquisition and storage.

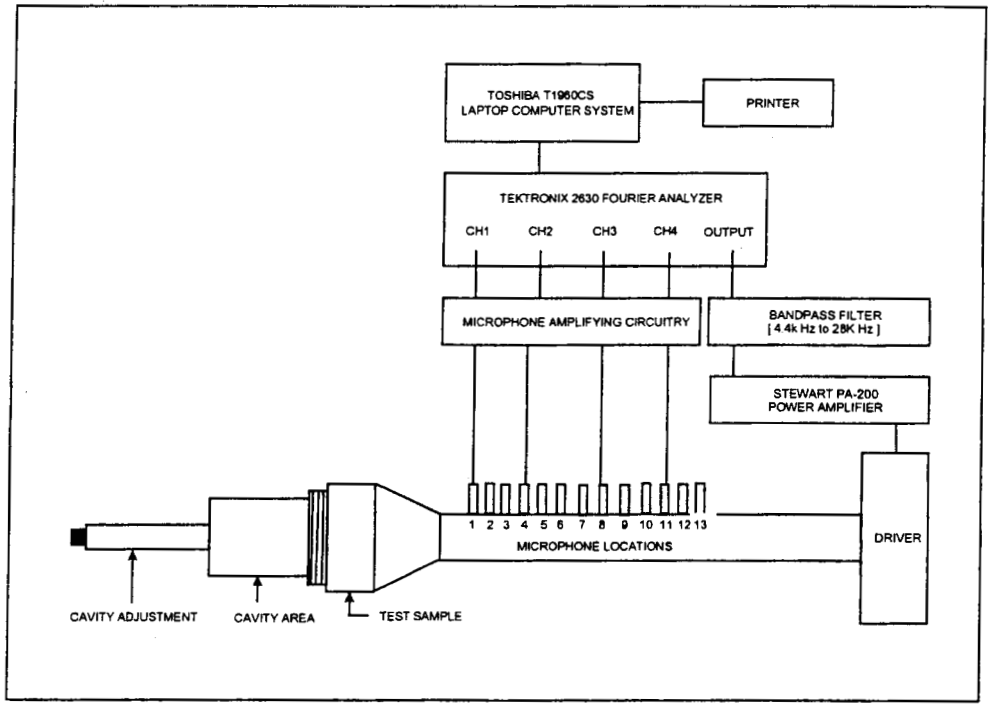

Figure 2-3 Schematic of 1.5 cm four-microphone high frequency impedance measurement system.

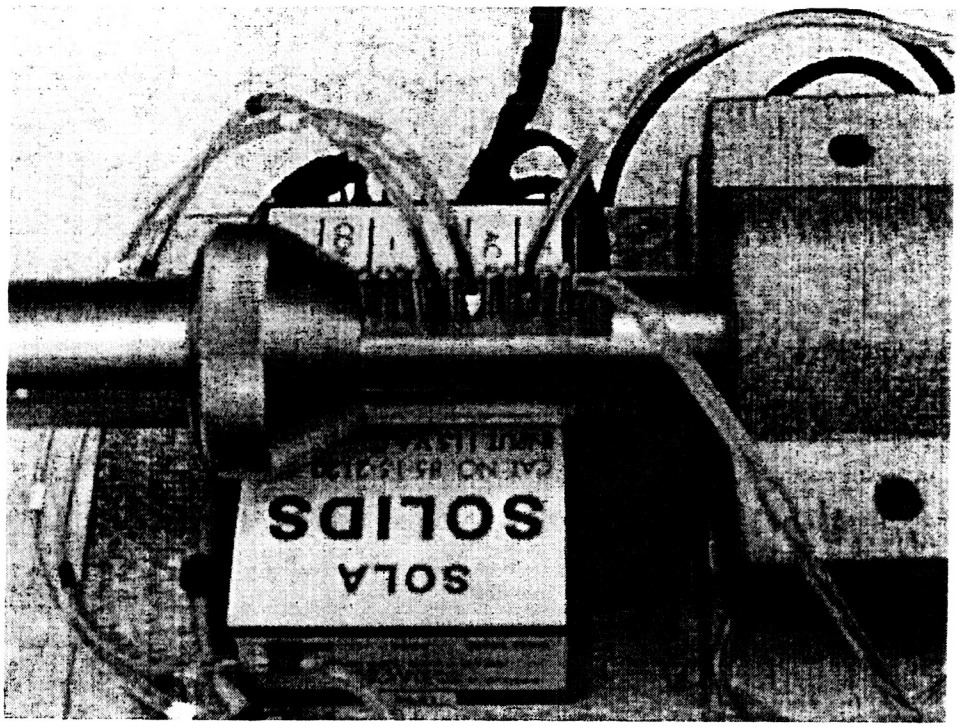

Figure 2-4 **Installation of four microphones in impedance tube.**

Figure 2-5 **40 watt compression driver for four-microphone high frequency impedance measurement system.**

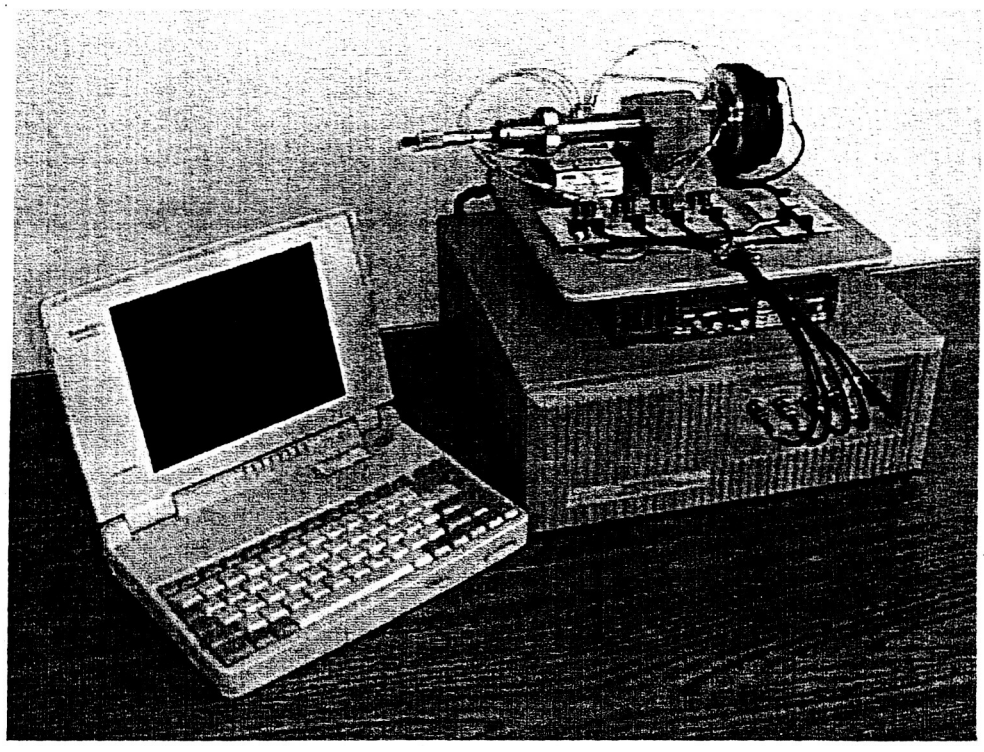

Figure 2-6 Fully-assembled prototype high frequency four-microphone impedance measuring system.

2.6.3 Data Acquisition System

Many different combinations have been checked to determine the optimum spacing and location of the four microphones. First, a calibration factor, i. e., the amplitude and phase mismatch between microphone #1 and the other microphones, was created for each pair of microphones, #1 and #2, #1 and #3, #1 and #4. The procedures based on ASTM -E1050-90 method were adopted as described below:

- use a Kevlar absorber as a test sample to prevent strong acoustic reflections.
- place microphone #1 and microphone #2 in a normal configuration, and then measure the transfer function,

$$H^{i} = |H^{i}| e^{j\phi_1} \tag{2-44}$$

- interchange the locations of microphone #1 and microphone #2, and then measure the new transfer function,

$$H^{ii} = |H^{ii}| e^{j\phi_2} \tag{2-45}$$

- calculate the calibration factor H_{c12} which represents the amplitude and phase mismatches $|H_{c12}|$ and ϕ_{c12}, using the following equation:

$$H_{c12} = (H^{i} \cdot H^{ii})^{1/2} = |H_{c12}| e^{j\phi_c} \tag{2-46}$$

where:

$$|H_{c12}| = (|H^{i}| \cdot |H^{ii}|)^{1/2}, \text{ and } \phi_{c12} = \tfrac{1}{2}(\phi_1 + \phi_2) \tag{2-47}$$

- for standard measurements, place microphone #1 and #2 at their normal locations and using the following equation to correct the mismatch in their responses,

$$H = |H| e^{j\phi} = H_{measured}/H_{c12} \tag{2-48}$$

where:

$$|H| = |H_{measured}| / |H_{c12}|, \quad \phi = (\phi_{measured} - \phi_{c12}) \tag{2-49}$$

- apply the same procedures to the microphones #1 and #3, microphones #1 and #4, to establish their correction factors, H_{c13} and H_{c14}.

The sound pressure levels of each microphone, as well as the amplitude and phase of the corrected transfer function for each pair of microphones, #1 and #2, #1 and #3, #1 and #4 are then measured. The measured data are used to calculate the acoustic impedance from Equation (2-35).

2.7 Test Samples

Four test panels (TP1, TP2, TP3, and TP4) were fabricated, with configurations as shown in Tables 2-1, 2-2, 2-3, and 2-4.

Table 2-1. TP1: 34% POA Perforate Structures with 0.15" Core Depth

Face Sheet		diameter 0.050"	thickness 0.032"	POA 34%	spacing 0.082"
Core & Back Skin	Core Height 0.15"	Core Type 3/16" cell; .003" Al foil, 4.2 lb/ft^3		Back 0.032" thick	Skin Aluminum

Table 2-2. TP2: 34% POA perforate Structure with 0.20" Core Depth

Face Sheet		diameter 0.050"	thickness 0.032"	POA 34%	spacing 0.082"
Core & Back Skin	Core Height 0.20"	Core Type 3/16" cell; .003" Al foil, 4.2 lb/ft^3		Back 0.032" thick	Skin Aluminum

Table 2-3. Bonded Wire Mesh Sandwich Structure TP3

Wire Mesh	33 rayls @ 105cm/s				
Face Sheet	R3 Rayls				
	47 rayls @105 cm/s	NLF: 1.20			
Core & Back Skin	Core Height 0.20"	Core Type 3/16" cell; .003" Al foil, 4.2 lb/ft^3		Back 0.032" thick	Skin Aluminum

Table 2-4. Bonded Wire Mesh Sandwich Structure TP4

Wire Mesh	35.5 rayls @105 cm/s				
Face Sheet	R3 Rayls				
	50.8 rayls @105 cm/s	NLF: 1.19			
Core & Back Skin	Core Height 0.20"	Core Type 3/16" cell; .003" Al foil, 4.2 lb/ft^3		Back 0.032" thick	Skin Aluminum

TP1 and TP2 have the same perforated face sheet, but different core depths. It was originally planned to apply different patterns of microporous PU films on TP1 and TP2, but schedule and budget limitations prevented completion of this task.

TP3 and TP4 are bonded wire mesh sandwich structures with different stainless steel wire meshes. A small core cell (3/16 ") was used to fabricate these panels. A pre-existing 47 rayls DynaRohr sample was the last sample tested.

2.8 Test Results and Discussion

A 3 cm Acoustic Impedance Tube System was used to cover the frequency range from 800 Hz to 6200 Hz. Figures 2-7, 2-8, and 2-9 show the acoustic impedance of 47 rayl DynaRohr samples, TP3 and TP4, but with a core depth increased 0.40 inches, to give more reasonable reactance values over the lower frequency range. The 1.5 cm two-microphone acoustic impedance tube system was then used to cover the frequency range from 2600Hz to 13,500 Hz for the same facesheet but with core lengths of 0.35 inches. Figures 11, 12, and 13 show the acoustic impedance of 47 rayl DynaRohr samples TP3 and TP4, with a core depth of 0.35 inches. Comparing Figures 2-7, 2-8, and 2-9 with Figures 2-10, 2-11, and 2-12, and accounting for the slightly different core depths, indicates good agreement between test results from these two systems.

The 1.5 cm, four-microphone acoustic impedance tube system was finally used to cover the frequency range from 6000 Hz to 20,000 Hz. Test data from the four-microphone system do not have the same smoothness as the other two measurement systems. The four microphone system was not able to easily and reliably obtain the desired high frequency measurements. This unsatisfactory result may be caused by the following factors:

- improper microphone location and spacing,
- data acquisition software - improper calibration procedure
- a bug in the data reduction software.

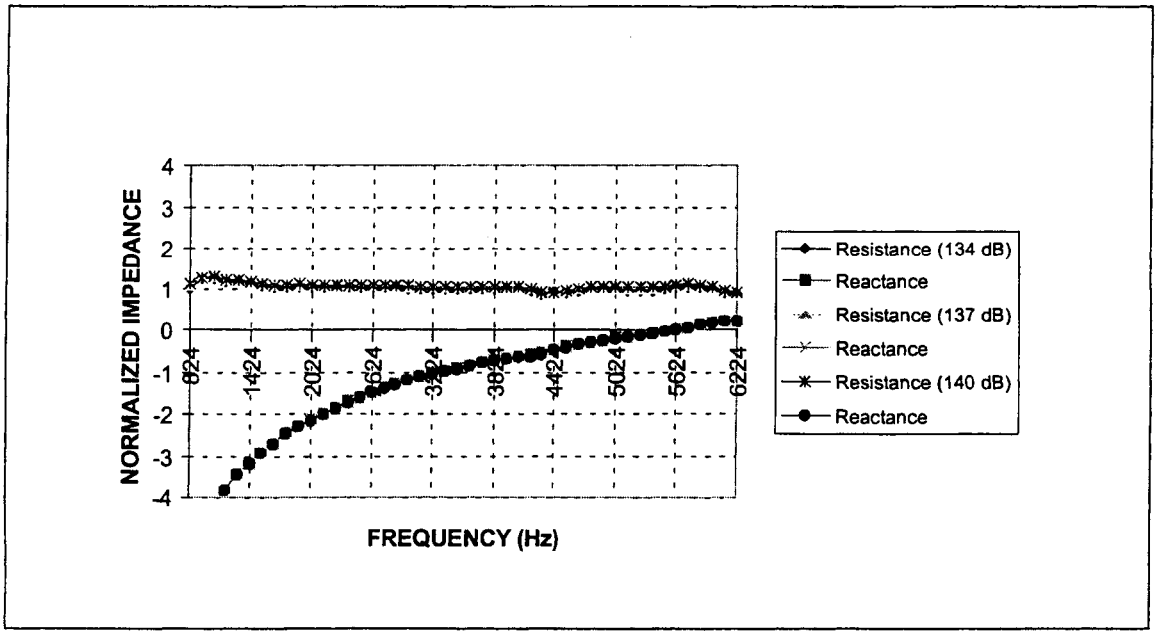

Figure 2-7 Acoustic impedance of 47 Rayl DynaRohr with 0.40 inch core depth, for 3 different SPL measured in 3.0 cm tube.

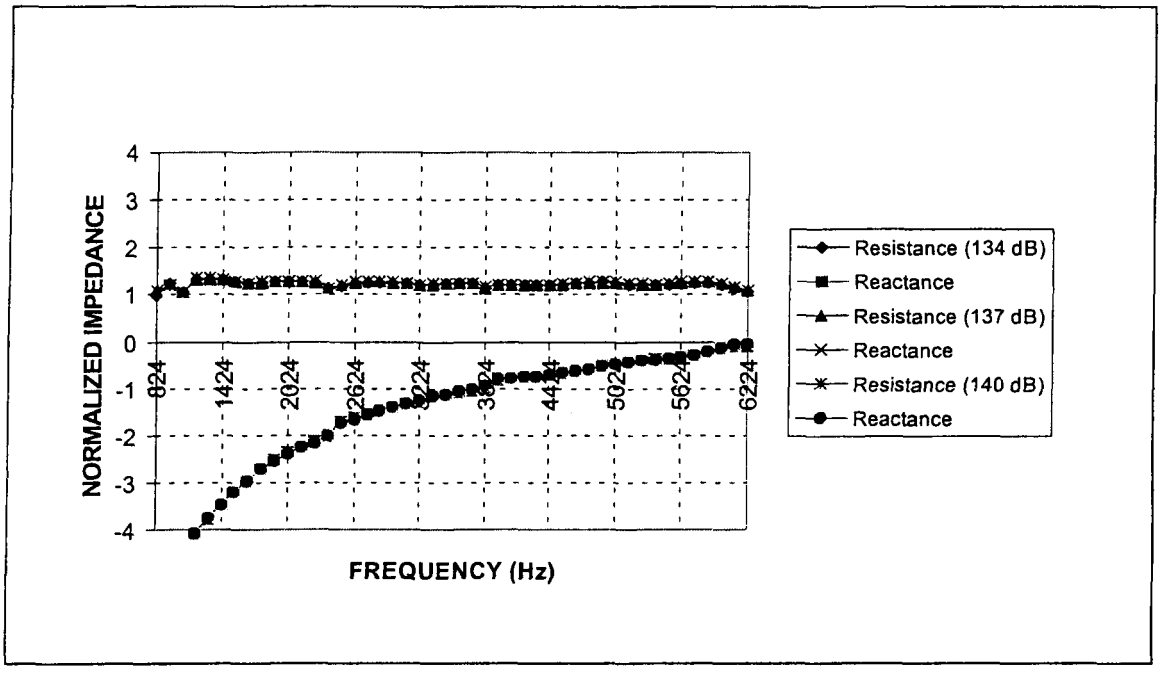

Figure 2-8. Acoustic impedance of TP3 with 0.40 inch core depth, for 3 different SPL measured in 3.0 cm tube.

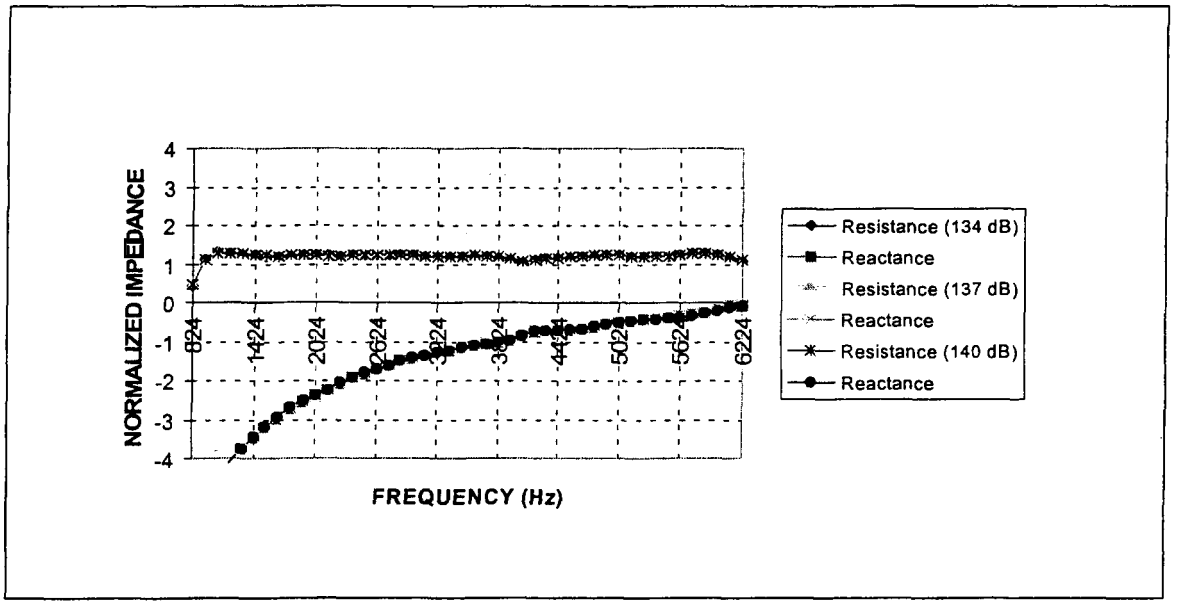

Figure 2-9 Acoustic impedance of TP4 with 0.40 inch core depth, for 3 different SPL measured in 3.0 cm tube.

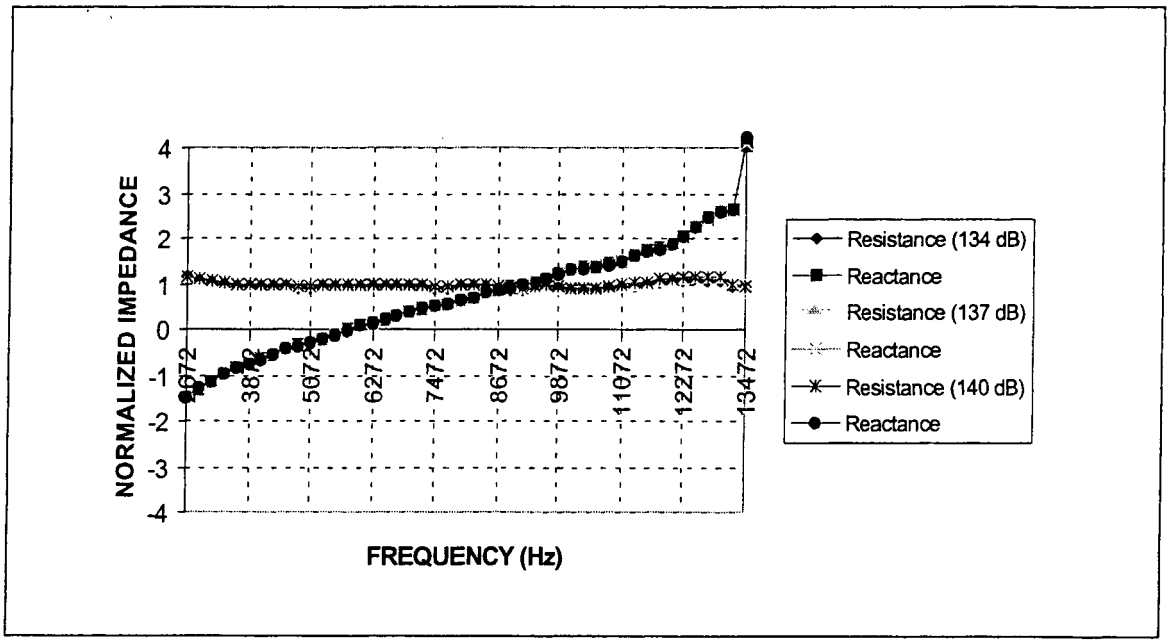

Figure 2-10 Acoustic impedance of 47 Rayl DynaRohr with 0.35 inch core depth, for 3 different SPL measured in 1.5 cm tube.

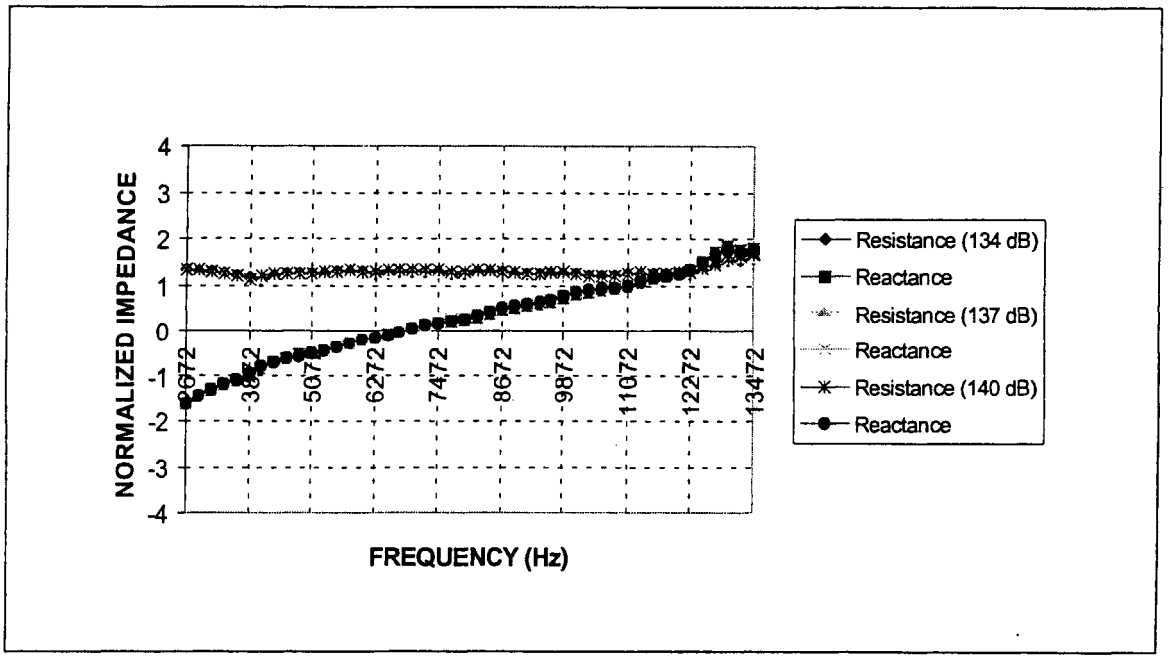

Figure 2-11 Acoustic impedance of TP3 with 0.35 inch core depth, for 3 different SPL measured in 1.5 cm tube.

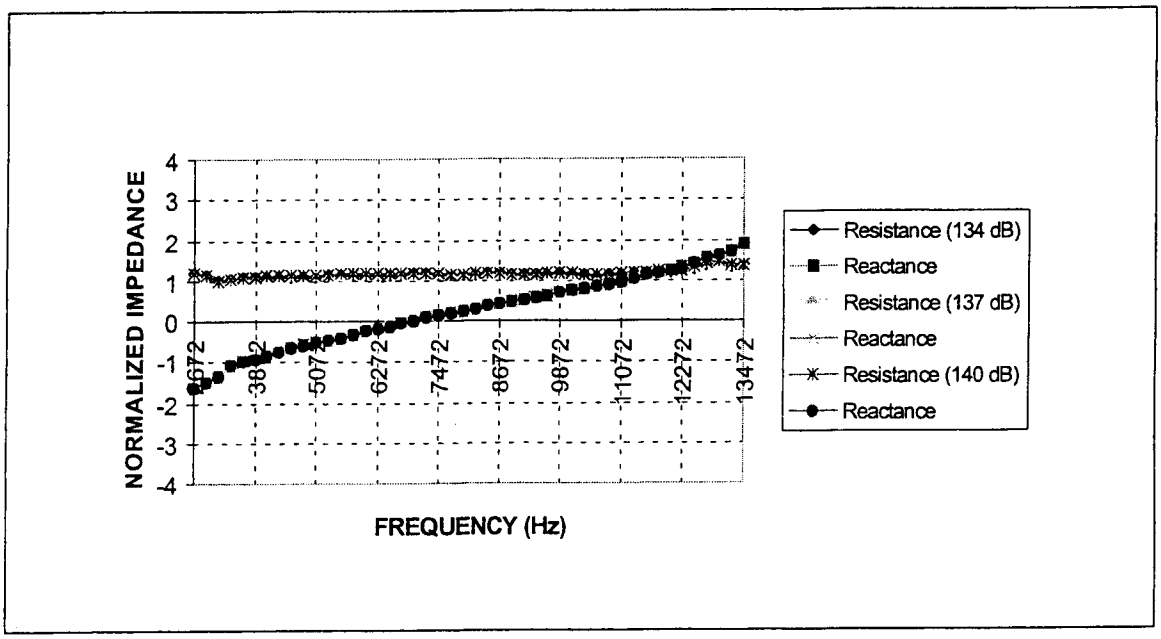

Figure 2-12 Acoustic impedance of TP4 with 0.35 inch core depth, for 3 different SPL measured in 1.5 cm tube.

2.9 Conclusions and Recommendations

The test results indicate that the 1.5 cm four microphone system needs further development. The microphone location and spacing needs to be modified to obtain a smooth curve. A new procedure needs to be developed for calibrating microphones and obtaining correct transfer functions among them. The data reduction program needs to be re-evaluated to meet requirements of Equation (2-35).

2.10 References

[1] Yu, J, Kwan, H. W., Echternach, D. K., Kraft, R. E., and Syed, A. A., "Acoustic Treatment Design Scaling Methods. Volume 3: Test Plans, Hardware, Results, and Evaluation", NASA Contractor Report NASA/CR-1999-209120/VOL. 3, April 1999.

3. Evaluation of Free-Field Method of Determining Acoustic Impedance

3.1 Definition of the problem

3.1.1 Introduction

The use of fractional-scale devices such as the GEAE Universal Propulsion Simulator (UPS) to study the acoustical behavior of aircraft engines requires that the acoustical liner treatment be represented correctly at frequencies up to approximately five times the full-scale frequencies. Full-scale liners are designed to attenuate sound in the 1-5 kHz range and tuned to have a maximum attenuation at approximately 2500 Hz. Consequently, it is necessary to understand how to design liner treatments up to approximately 25 kHz for use in propulsion simulators such as the UPS.

The standard method for the measurement of acoustical properties of materials and systems is the "two-microphone method" in which a sample of the material is located at one end of a closed tube and exposed to a plane-wave sound field created by a loudspeaker or acoustic driver located at the other end (ASTM, 1990). A pair of microphones is used to determine the transfer function at two points in the tube within a few diameters of the sample. From the transfer function the reflection coefficient, acoustical impedance, and sound absorption coefficient of the sample may be obtained.

There are a number of limitations and difficulties of the ASTM method including (1) minimizing errors due to the preparation and mounting of a sample of aircraft liner treatment in a tube, (2) using closely spaced microphones at 25 kHz, (3) determining the impedance at oblique incidence, and (4) incorporating grazing flow in the measurement.

In the free field method, a sample of material is placed on a hard floor in a hemi-anechoic chamber and exposed to sound from a sound source located above the sample. A pair of microphones determines the transfer function and, similar to the ASTM method, the impedance of the material may be determined. The free field method has the potential to overcome many of the limitations of the ASTM method, but to date its use has been limited to the measurement of the sound absorption coefficient of porous materials in the 1-8 kHz range.

3.1.2 Objective and scope

The objective of this project was to determine the feasibility of using the free field method for the measurement of acoustical impedance at frequencies up to approximately 25 kHz. The present scope is limited to no-flow measurements at normal incidence. Some issues related to the use of the free field method include (1) the size of the sample to be tested, (2) the selection and position of the source, (2) the selection and mounting of microphones to minimize diffraction of the sound field, (4) the calibration of the microphones, and (5) the possibility of making "free field" measurements in a laboratory environment.

3.1.3 Report organization

A literature survey of methods to measure acoustical impedance is presented in Section 3.2 of this report. This is followed in Section 3.3 by results of a computer simulation of the free field method to determine the effect of sample size, source location, and microphone location. Section 3.4 describes the experimental test apparatus designed and constructed to implement the free field method, and Section 3.5 contains the results of experiments to determine the impedance of porous materials and two samples of full-scale acoustical liner treatments supplied by BFGoodrich Corporation. Section 3.6 discusses the findings of the project and the recommendations for additional study.

3.2 Literature Survey

3.2.1 Introduction

Historically, sound absorption is one of the most common approaches to reduce the sound intensity level. However, because sound absorbing materials are difficult to model, sound absorption is often determined by experiment. Extensive research has been done in this area over many years. This section is a brief literature survey on high bypass turbofan simulators, sound absorbing liners, different methods used to measure acoustic impedance and their advantages and disadvantages.

3.2.2 Turbofan propulsion simulator

Aircraft engines must meet ever increasing gross weight requirements as well as environmental concerns of noise and emissions. Continuing requirements for performance improvement of higher thrust turbofans are met by increased bypass ratios, but the success of this new generation of high bypass ducted turbofans depends on understanding the acoustic impact from reduced treatment areas, inlet-fan coupling and operability, as well as overall system performance. To achieve these goals, a versatile scale model ultra-high-bypass turbofan propulsion simulator (UPS)(Balan, 1993) large enough to operate as a fan rig, yet small enough to be installed in a wind tunnel for evaluating overall acoustic, operability, and system performance was developed. The simulator is not intended to be a scale model of a full scale very high bypass engine but rather a tool to understand engine generated noise (Hodges, 1994). However, the model fan pressure ratio and mass flow rate are consistent with those parameters expected from the full scale engine. This similarity lends credence to the applicability of model results to full scale. The basic layout of the simulator is shown in Figure 3-2.1.

There are three basic modules, the fan, turbine, and mid-housing or sting. The metric fan module is cantilevered from the sting module, and the sting module is mounted on the turbine module. The fan module can be installed with the pylon of the engine to be simulated. The drive turbine consists of four stages, with the blade vane count chosen for acoustic cutoff. The turbine is driven by high-pressure heated air. Acoustic treatment panels are mounted on the inner wall of the nacelle. The exhaust duct of the turbine is also acoustically treated to reduce the turbine

noise, which otherwise could contaminate the aft-radiated, fan-noise measurements (Balan, 1993). Table 3-2.1 presents operating points of the full scale GE90 engine.

Table 3-2.1. Turbine operating points (Balan, 1993).

Fan	Speed (rpm)	Power (hp)	P_{tin} (psi)	T_{tin} (^{0}R)	Flow (lbm/sec)
GE90	23,000	730	645	529	8.5
GE90	25,500	1,000	866	529	11.4

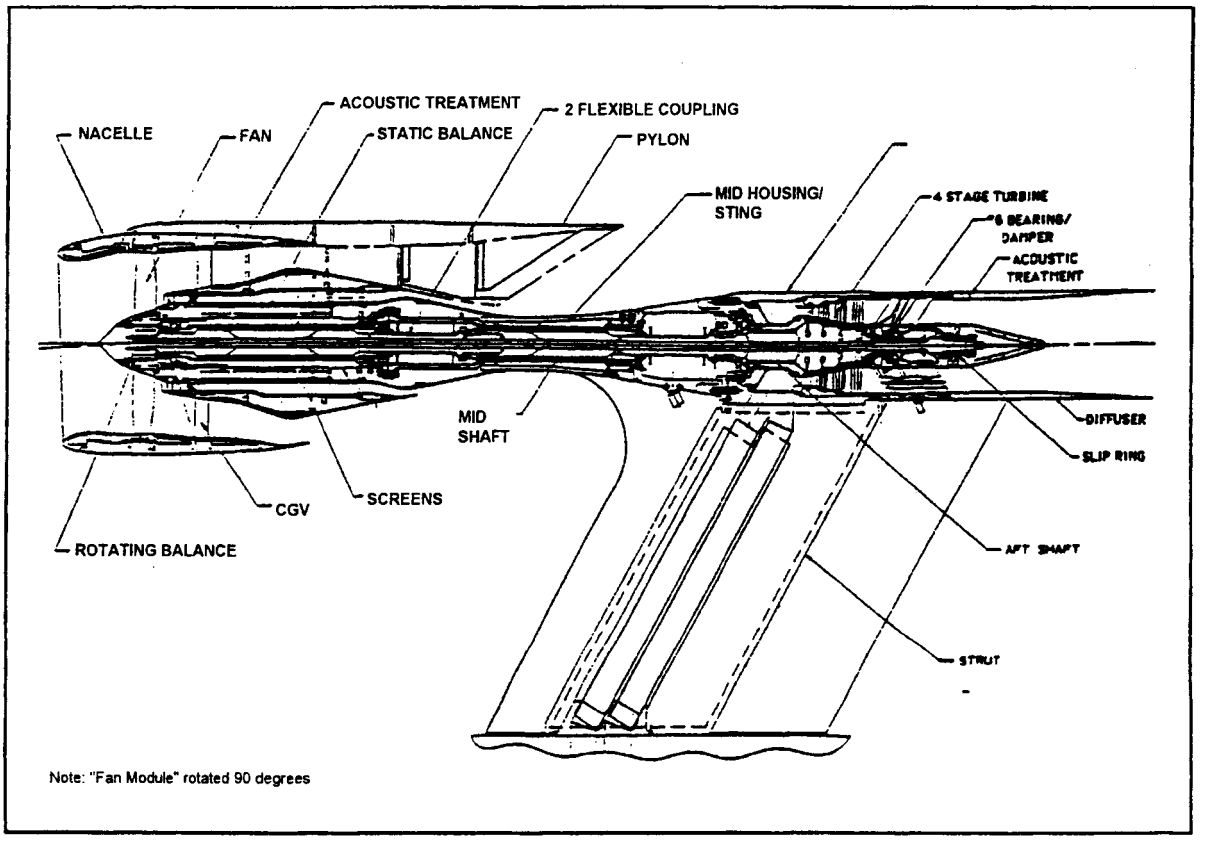

Figure 3-2.1 Ultra high bypass propulsion simulator schematic layout (Balan, 1993).

3.2.3 Parallel-element liner impedances for improved absorption

The need to reduce noise emissions from aircraft operating near communities adjacent to airports continues to motivate intensive research to improve the sound suppressing efficiency of acoustically treated turbo-machinery ducts carrying high speed subsonic air flows and multiple high-order acoustic modes. Aircraft duct liner designs for turbofan engines are required to be

concerned with safety, durability, and aerodynamic performance, along with the need to attenuate discrete-frequency sound caused by interactions between the wakes of fan blades and outlet guide vanes. This sound, with spectral peaks at the fan-blade passage frequency and its harmonics, typically exhibits a narrow-band character (Parrott, 1995).

Sound-absorbing liners consisting of thin porous sheets bonded to honeycomb cores, shown in Figure 3-2.2(a), are used to suppress discrete-frequency fan sound. Such liners are characterized as lumped parameter systems having a single degree of freedom (SDOF). The porous face sheet provides the dominant portion of the acoustical resistance; the honeycomb core provides most of the acoustical reactance. Because the individual honeycomb cells are usually acoustically isolated from one another, these liners exhibit *locally reacting* behavior (Parrott, 1995, Allard, 1993). The ability to "tune" the attenuation enables the designer to make the liners effective for attenuation of relatively narrow-band noise. Figure 3-2.2(b) shows a ceramic honeycomb material, which is currently under development. It is too heavy and fragile to be of practical use for aircraft duct-liner applications (Parrott, 1995).

3.2.4 Liner impedance

Current liner design models capture the essential physics of these systems as a lumped resistive element, supplied by the thin face sheet, in series with a reactance supplied by a partitioned backing cavity (see Figure 3-2.2(a)). Generally, dissipation of acoustic energy in the partitioned cavities is assumed to be negligible relative to the energy dissipated in the resistive face sheet. This assumption is based on the fact that cavity dissipation occurs mainly in the viscous layer at the cell walls. The normal-incidence impedance Z can be written as

$$Z = Z_{fs} + Z_{cav} = R_{fs} + j(X_{fs} + X_{cav}) \tag{3-2.1}$$

where

Z_{fs} = impedance of the face sheet
Z_{cav} = impedance of the cavity
R_{fs} = resistance of the face sheet
X_{fs} = reactance of the face sheet
X_{cav} = reactance of the cavity

The absorption coefficient for an acoustic ray incident at an angle ϕ on a locally reacting surface underneath a grazing flow of Mach number M is given by (Parrott, 1995)

$$\alpha = \frac{4R(\cos\phi)(1 + M\sin\phi)}{[1 + R(\cos\phi)(1 + M\sin\phi)]^2 + [X(\cos\phi)(1 + M\sin\phi)]^2} \tag{3-2.2}$$

where

R = acoustic resistance normalized by ρc

X = acoustic reactance normalized by ρc

In another type of liner, a sheet divides the backing cavity channels into coupled resonant systems with the septa resistances serving as coupling elements, thus providing an additional degree of freedom. This design, called a multi-degree of freedom absorber, has additional design parameters that may generate a composite impedance with a greater absorption bandwidth.

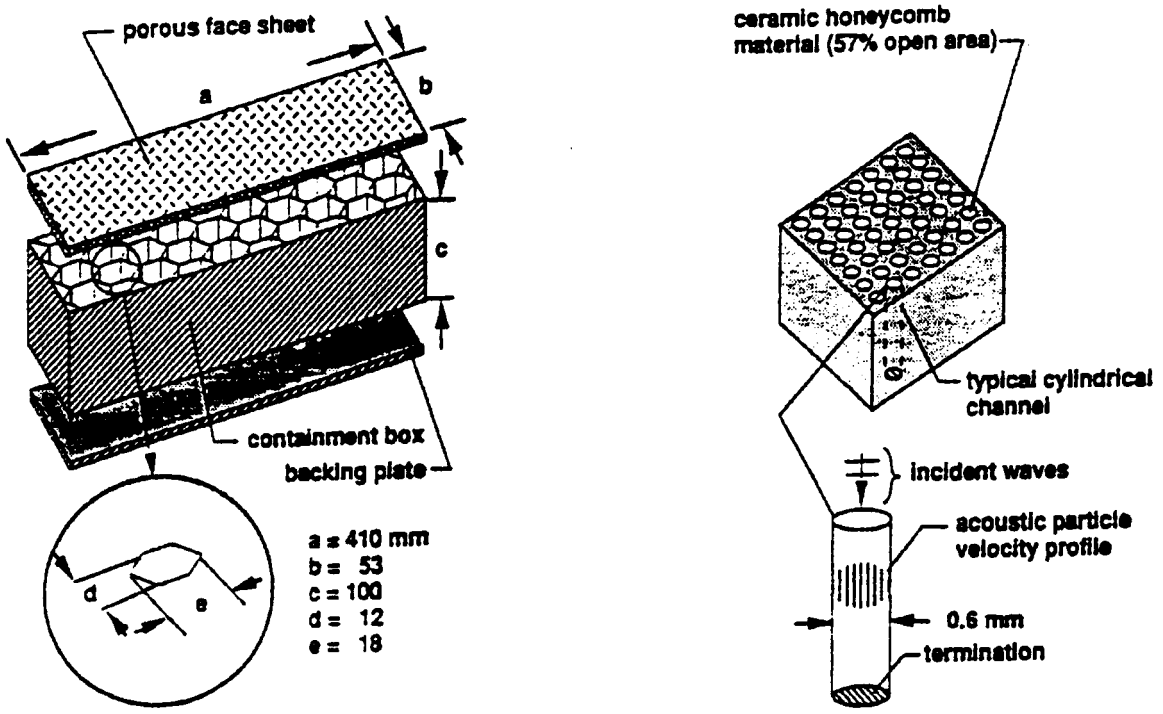

Figure 3-2.2 (a) Conventional single degree of freedom liner test specimen and (b) Ceramic honeycomb material (Parrott, 1995)

3.2.5 Acoustic impedance measurement

Commonly, impedance is measured by using an impedance tube and a pair of microphones (ASTM, 1990). The impedance tube method is used extensively for homogeneous samples in the low to medium frequency range. Another approach is to generate a sound field in a free field, allow the sound waves to reflect from the test sample and make free field transfer function measurements from which the reflection coefficient may be determined. Both methods have advantages and limitations. The impedance tube method and the free field method are briefly described in the following sections.

3.2.5.1 Impedance tube and two microphone method

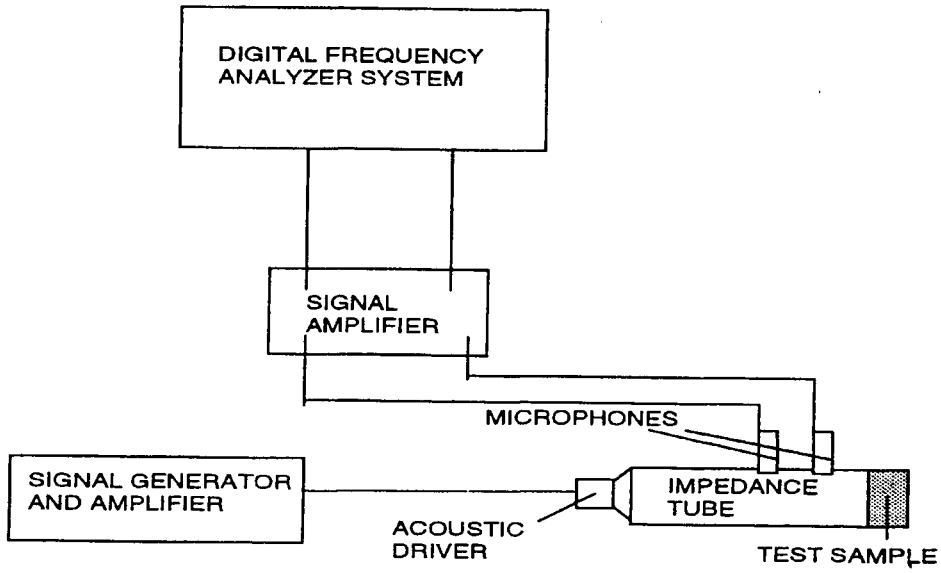

Figure 3-2.3 Impedance tube method, schematic layout

In the impedance tube method, plane waves are generated in a tube by a random noise source, and the decomposition of the standing wave is achieved with measurement of acoustic pressures at two fixed locations close to the sample using wall-mounted microphones. Using a digital frequency analysis system, the complex acoustic transfer function between the two microphone signals is determined and used to compute the normal incidence absorption and impedance ratios of the acoustic material (ASTM, 1990), as shown in Figure 3-2.3.

3.2.5.2 Limitations of the impedance tube method

The upper limit of the frequency of analysis is governed by the diameter of the tube and the microphone spacing. For a given tube diameter, the onset of cross modes determines one limiting value of the frequency of analysis. Also, the analysis on which the theory is based breaks down for a frequency whose wavelength is double the microphone spacing, thereby defining a second limiting value of the frequency of analysis. The upper frequency limit of the analysis is the lesser of the two. These limiting values of frequency f_1 and f_2 can be determined from the following relations (ASTM, 1990).

$$f_1 < 0.586\, c/d \qquad \text{or} \qquad f_2 << c/2s$$

where

c = speed of sound in the tube (m/s)

d = diameter of the tube (m)

s = microphone spacing (m)

To extend the impedance tube method to frequencies where the scale model liners must be tested (10-25 kHz) requires that the tube diameter and microphone spacing be unrealistically small. The ASTM method also is limited to normal incidence and no flow.

3.2.6 Free field acoustic impedance measurement

For high frequency and oblique incidence situations, the free field method appears to have advantages over the impedance tube method because the f_l limit above is not a factor. In the free field method, a sound field is generated using a sound source placed a known distance from a reflecting surface. As the sound waves are reflected from the impedance surface, a standing wave is generated in the free field. If acoustic pressure is measured at two different points in the sound field, a transfer function can be calculated by dividing one complex pressure by the other and used to determine the reflection coefficient, as will be shown below. If the source is placed far away from the impedance plane, then the sound field is approximately plane; otherwise, the sound field is spherical in nature.

3.2.6.1 Surface impedance at normal incidence using two-microphone technique

Figure 3-2.4 shows the setup for the free field impedance measurement technique. Theoretically the test specimen should be infinite in extent.

3.2.6.1.1 Spherical wave hypotheses

The reflection coefficient is given by (Allard, 1989),

$$R_e = \frac{\dfrac{e^{jkr_2}}{r_2} - H_{12}\dfrac{e^{jkr_1}}{r_1}}{H_{12}\dfrac{e^{jkr_{11}}}{r_{11}} - \dfrac{e^{jkr_{22}}}{r_{22}}} \qquad (3\text{-}2.3)$$

where the distances r_1, r_2, r_{11} and r_{22} are shown in Figure 3-2.4, and H_{12} is the complex transfer function ratio of sound pressures P_2/P_1 between the two microphones M_2 and M_1.

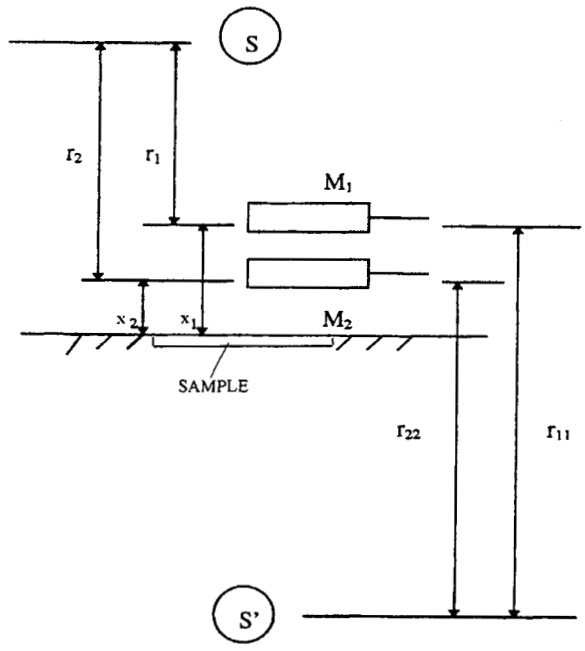

Figure 3-2.4 Normal incidence impedance measurement

3.2.6.1.2 Plane wave hypotheses

When a spherical source is placed far away from the reflecting surface, i.e., the distances

$$r_1 \cong r_2 \cong r_{11} \cong r_{22}$$

the denominators of the exponential terms may be canceled in Eq. (3-2.3). Further, the exponents can be rearranged to yield

$$R_e = \frac{e^{-jkx_2} - H_{12}e^{-jkx_1}}{H_{12}e^{jkx_1} - e^{jkx_2}} \tag{3-2.4}$$

Eq. (3-2.4) is the same result used in the ASTM method (ASTM, 1990).

3.2.6.2 Measurement of acoustic impedance at oblique incidence

The reflection coefficient for oblique incidence is given by (Allard, 1985)

$$R_e(\phi) = \frac{e^{jkd_1\cos\phi} - H_{12}e^{jkd_2\cos\phi}}{H_{12}e^{jkd_2\cos\phi} - e^{-jkd_1\cos\phi}} \tag{3-2.5}$$

where the variables are shown in Figure 3-2.5. The term $d_1\cos\phi$ is the normal component of the distance between the source S and M_1, i.e., Eq. (3-2.5) reduces to Eq. (3-2.4), when $\phi=0$. This analysis assumes that the source is placed far away from the sample, so that the plane wave assumption holds good at the sample.

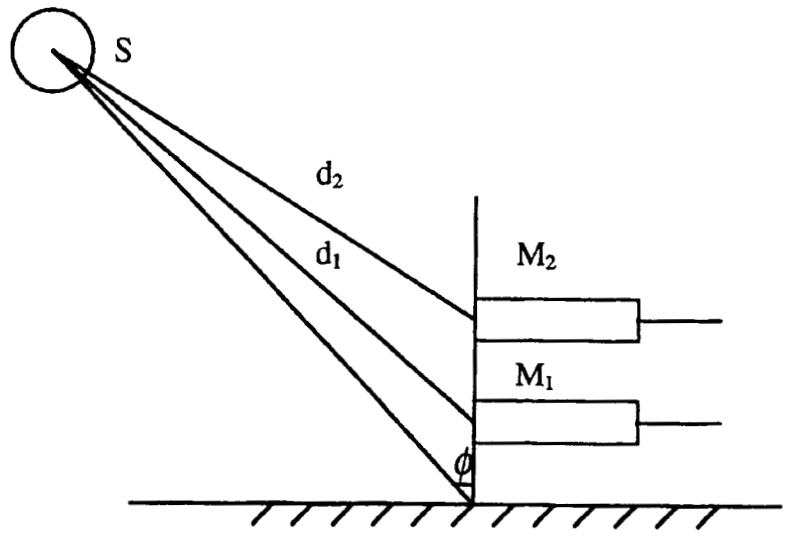

Figure 3-2.5 Oblique incidence, loudspeaker S, microphones M_1 and M_2

3.2.6.3 Finite difference approximation

In the free field method described above, the reflection coefficient of the material is expressed directly as a function of the ratio of two pressures measured at two close positions. In the finite difference approximation, the impedance at the midpoint M of the microphones is estimated by a finite difference approximation of the sound pressure and particle velocity, as shown in Figure 3-2.6.

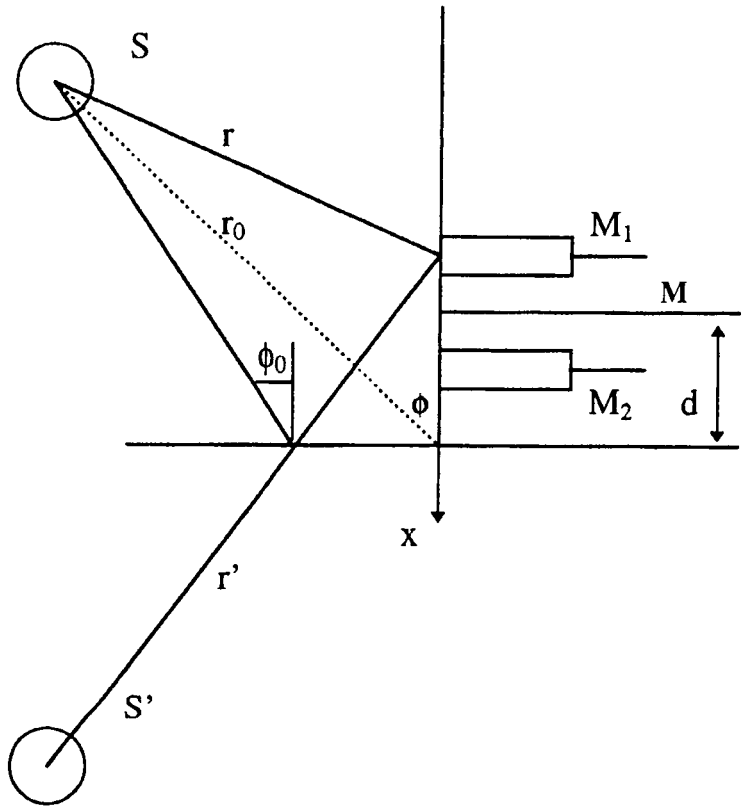

Figure 3-2.6 Finite difference approximation

The acoustic impedance at the midpoint M between two measurement points M_1 and M_2 is given by following formula (Li, 1996),

$$Z_M = \frac{\rho c}{\cos\phi_0}\left[\frac{e^{jkr}}{r} + R_e(\phi_0)\frac{e^{jkr'}}{r'}\right]\left[e^{jkr}\left(1+\frac{j}{kr}\right)\frac{\beta}{r} - R_e(\phi_0)e^{jkr'}\frac{\left(1+\frac{j}{kr'}\right)}{r'}\right]^{-1} \quad (3\text{-}2.6)$$

From the measured estimate of Z_M, the reflection coefficient of the sample $R_e(\phi)$ may be determined from Eq. (3-2.6). Comparing the $R_e(\phi)$ obtained by the finite difference approximation method with the transfer function method, an error function F can be determined (Li, 1996):

$$F(\phi_0) \cong \frac{\gamma}{\tan\gamma} - j\frac{\gamma^2}{kr_0} \qquad \gamma = ka\cos\left(\frac{\phi_0}{2}\right)$$

where *a* is the microphone spacing. Using the error function, the sample impedance Z' determined from Eq. (3-2.6) may be corrected to yield

$$Z = Z' F(\phi_0) \tag{3-2.7}$$

3.2.7 Three point method

The three point method (TPM) is an impedance tube method (Wuzhou, 1996) which is claimed to be better than the ASTM method based on two microphones. The TPM eliminates the limitation (see Section 2.4.2) when the microphone spacing is one half the wavelength. Two transfer functions are measured using the TPM, one (H_{12}) between microphones M_1 and M_2 , and the other (H_{23}) between microphones M_2 and M_3, as shown in Figure 3-2.7. If s_1 and s_2 are the distances between pair M_1 and M_2 , and pair M_2 and M_3 , respectively, then the reflection coefficient is given by (Wuzhou, 1996)

$$R_e = \frac{\left(H_{12} - e^{-jks_1}\right)e^{2jkL_2}\left(e^{jks_1} - H_{12}\right)^* + \left(H_{23} - e^{-jks_2}\right)e^{2jkL_3}\left(e^{jks_2} - H_{23}\right)^*}{\left(e^{jks_1} - H_{12}\right)\left(e^{jks_1} - H_{12}\right)^* + \left(e^{jks_2} - H_{23}\right)\left(e^{jks_2} - H_{23}\right)^*} \tag{3-2.8}$$

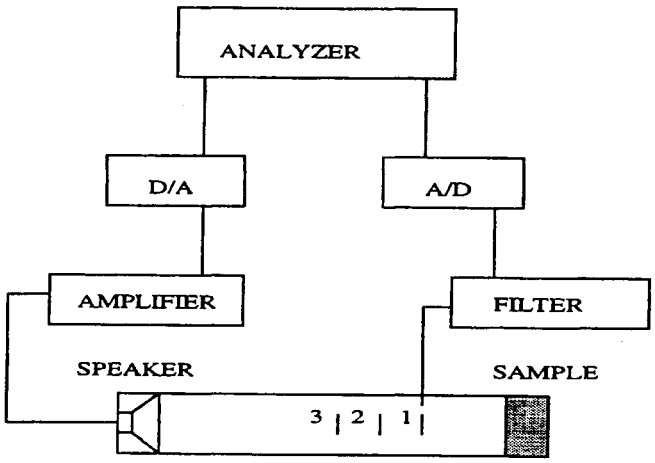

Figure 3-2.7 Three point method for determining impedance

3.2.8 Cepstral techniques for the measurement of acoustic reflection coefficients

The cepstral technique (Bolton, 1984) for the measurement of the normal incidence plane wave reflection properties of plane, layer-wise homogeneous surfaces makes use of cepstral methods of signal analysis. The cepstrum is defined as the Fourier transform of the logarithm of the power spectrum of a signal. The presence of echo in a signal causes the spectrum to be modulated by a function which is periodic in the frequency domain. By Fourier transforming the power spectrum, periodic features are transformed into line features. In the absence of other effects, such as sound absorption or dispersion in the propagation medium, the only source of channel distortion along a reflected path is the reflecting surface itself. The structure of the cepstrum of a signal containing a single echo is such that the impulse response of the reflector appears as a prominent feature. If experimental conditions are arranged so that the impulse

response appears in isolation, it is possible to extract it from the cepstrum, and, by Fourier transforming it, deduce the surface reflection coefficient.

A source and receiver are placed a distance above a reflecting plane, as shown in Figure 3-2.8, and the reflected sound is assumed to appear to originate at the image source location as shown. The source is assumed to be omnidirectional. The total acoustic pressure at the receiver $p_T(t)$, in terms of the contribution arriving directly from the source p(t) and the reflected component is

$$p_T(t) = p(t) + \left(\frac{r_1}{r_2}\right) p(t) * h(t - \tau) \tag{3-2.9}$$

where h(t) is the surface impulse response of the reflecting surface at a given angle of incidence, r_1 and r_2 are, respectively, the distances from the source to the receiver and from the image source to the receiver, τ is the delay resulting from the path length difference between the direct and reflected signals (equal to $(r_2 - r_1)/c$, where c is the speed of sound), and * indicates convolution. If Eq. (3-2.9) is Fourier transformed it becomes,

$$p_T(\omega) = p(\omega)\left[1 + \left(\frac{r_1}{r_2}\right) H(\omega) e^{-j\omega\tau}\right] \tag{3-2.10}$$

where $p_T(\omega)$, $p(\omega)$ and $H(\omega)$ are the Fourier transforms of $p_T(t)$, p(t) and h(t), respectively, and ω is the radian frequency.

Thus, the cepstral method for the measurement of acoustical reflection coefficients is a transient technique which uses a sound source to produce a finite duration test signal. Once the surface impulse response has been determined it is only necessary to Fourier transform it to obtain the reflection coefficient, from which the surface normal impedance can be calculated, if desired.

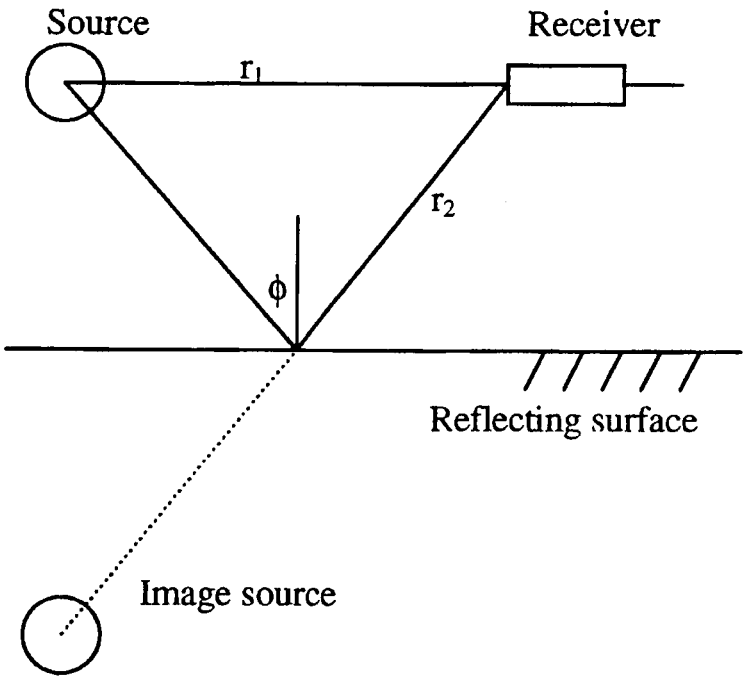

Figure 3-2.8 Experimental geometry used for the cepstral method (Bolton, 1984)

3.2.9 Comparison method

An *in situ* method for the measurement of impedance and absorption coefficient of a wind tunnel wall treatment was used by Dahl (Dahl, 1990). The method requires one acoustic source, located a distance away from the treatment and one microphone placed on the surface to measure the acoustic signal. A sound pressure measurement is taken with a hard surface that defines, for reference, the amplitude and phase characteristics of the incoming acoustic wave. The measurement is then repeated with a soft surface. By comparing the two measurements, the source characteristics can be eliminated (Dahl, 1990), leaving the data in a form that represents only the effect of the soft surface on an incoming acoustic wave.

3.2.10 Summary

Table 3-2.2 is a summary of the strengths and weaknesses of the various methods used for the measurement of the acoustic impedance.

Table 3-2.2. Strengths and weaknesses of commonly used methods (Jones, 1997).

Method	Strengths	Weaknesses
Standing Wave Method (SWM)	Good accuracy over 0.1 to 10 ρc impedance range Can automate via probe and SWR and null-searching probe Standing wave parameters directly measured	Accuracy is limited by SWR and null location resolution. Not suited to grazing incidence/mean flow environments. Tedious-time consuming.
Two-microphone method without microphone switching (TMM)[a]	Significant time saving No hardware movement Ideal for quick screening tests with random noise source	Assumes 1-D wave propagation model Accurate microphone amplitude and calibrations required Accuracy degrades at microphone separation near half-wavelength Accuracy degrades for large wavelengths
Two microphone method with microphone switching (TMM)[b]	Same as above Precise microphone calibrations not required	Same as above except second point
Cepstral technique (impulse technique)	Test can be conducted in non-anechoic environments without disturbing test sample. Other methods need to have the test specimen cut to the size of the tube which may not be representative surface as a whole. This measurement can be taken directly over the test surface.	Requires very short duration signals. Iterative solution.
Comparison method	This method requires only one microphone to be used to make measurements. It eliminates the source characteristics from the measurements.	Time consuming.

[a] Original implementation

[b] Modified implementation, currently in use in NASA Langley Research Center. (Jones, 1997)

3.2.11 High intensity, high frequency source of sound

A device has been developed (Salikuddin, 1987) to generate high frequency noise with low frequency acoustic drivers. The principle behind this mechanism is the use of non-linear propagation effects of high intensity sound waves inside hard-walled ducts which alter the shape of the sound waves as shown in Figure 3-2.9. For a fixed acoustic power level, the intensity of the sound increases as the duct cross-sectional area decreases (Salikuddin, 1987). In turn, a strong non-linear effect is obtained. Thus, the larger the contraction ratio, the stronger the non-linear effect and the broader will be the frequency range. In the second case, a reasonably intense sound wave emanating from the driver propagates through the long duct, and, thereby experiences non-linear propagation for a longer time. Therefore, the longer the duct, the greater the non-linear effect and the larger the frequency range. A combined contraction plus straight-duct-device gives qualitatively similar results, except that now the waveform steepens faster with increasing tube length.

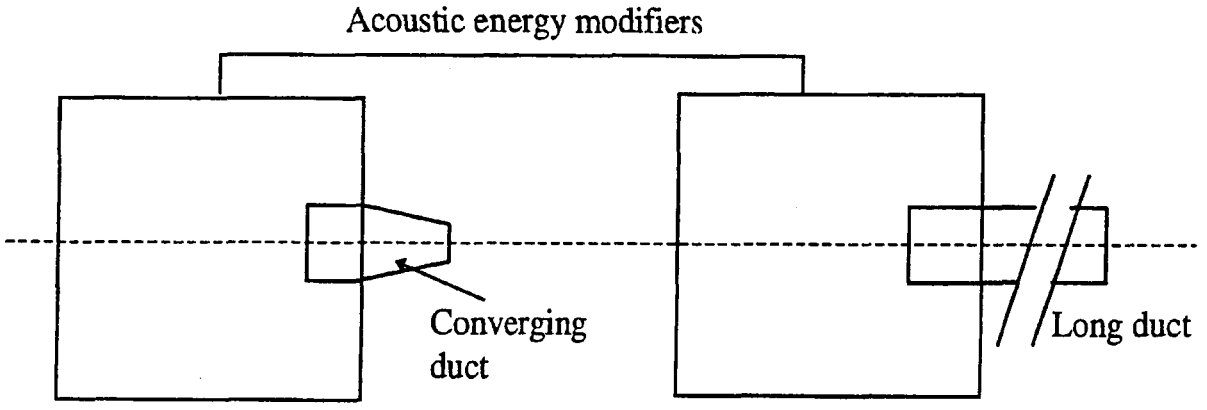

Figure 3-2.9 High frequency source of sound (Salikuddin, 1987)

3.3 Simulation Techniques

3.3.1 Introduction

The primary objective of this project is to determine whether the free field impedance measurement technique can be extended to frequencies up to 24 kHz. To answer this question, it is important to obtain an understanding of the relevant design parameters required to design and construct the experimental testing apparatus (ETA). The three most important considerations are the minimum required sample size, the maximum allowable size of the microphones, and the distance of the microphone pair from the plane of reflection. Once these factors are determined, the ETA can be built and used for experiments.

In this section, a numerical solution is used to gain a better understanding of the free field method. The boundary element method (BEM) has been successfully used to simulate noise in different situations and has been found to yield accurate results in the past. In essence, a free field reflection problem is a 'scattering' problem. The BEM can be used effectively to determine the minimum sample size required to establish a steady standing wave above the reflecting plane. The BEM can also determine how the sound field is affected by the scattering of sound from microphone tips.

3.3.2 Determination of sample size

Using the BEM program BEMAP, a model was made in which a square grid of boundary elements having a known impedance z was placed on an otherwise rigid, infinite plane, as shown in Figure 3-3.1. A spherical point source was located a distance r from the plane.

An infinite reflecting plane will produce a perfectly uniform standing wave, but, due to limitations on the sample size, irregularities are expected. A 16 X 16 cm^2 sample grid was used to simulate a standing pressure wave above the sample using the BEM, as shown in Figure 3-3.1. The acoustical impedance of the sample was selected as $z/\rho_0 c = 1.5 - 1.5j$. The standing wave pattern predicted by the BEM at 25 kHz with $r = \infty$ (plane wave source) is shown in Figure 3-3.2. It can be noted from Figure 3-3.2 that the standing wave is not quite uniform. The origin of the coordinate system for the computation is at the sample surface, located at the center of the sample.

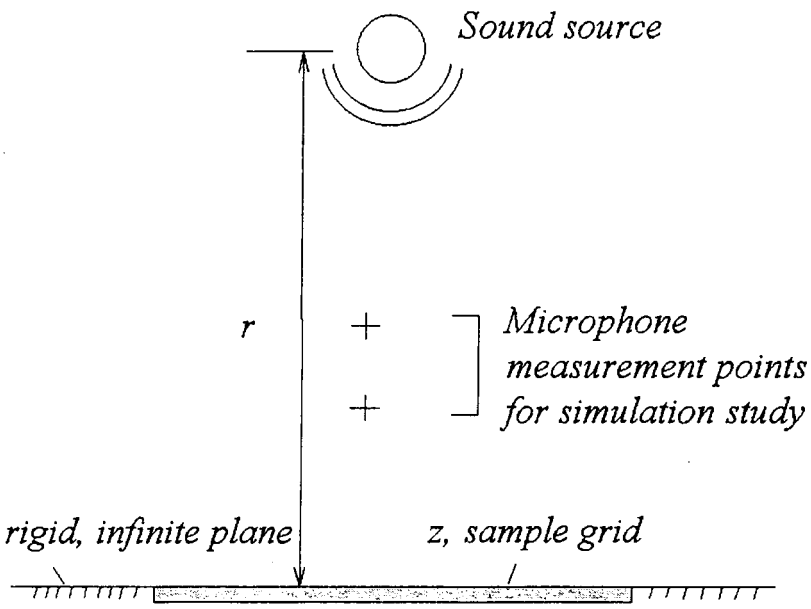

Figure 3-3.1 BEM method for determination of sample size

The impedance of the sample can be determined by picking up two arbitrary points in the standing wave. These two points can be treated as acoustic centers of two microphones, and the distances of these points from the sample and the acoustic pressure predicted at these locations by the BEM will yield the impedance of the sample by using Eq. 3-2.4.

Figure 3-3.3 shows the impedance variation with distance of the microphones from the sample and with microphone spacing. When the microphone spacing is 0.7 cm, the variation in the impedance measured along the direction of travel of the reflected wave is erratic; 0.7 cm is approximately one-half the wavelength at 25 kHz, and the impedance is indeterminate. (see Eq. 3-2.4).

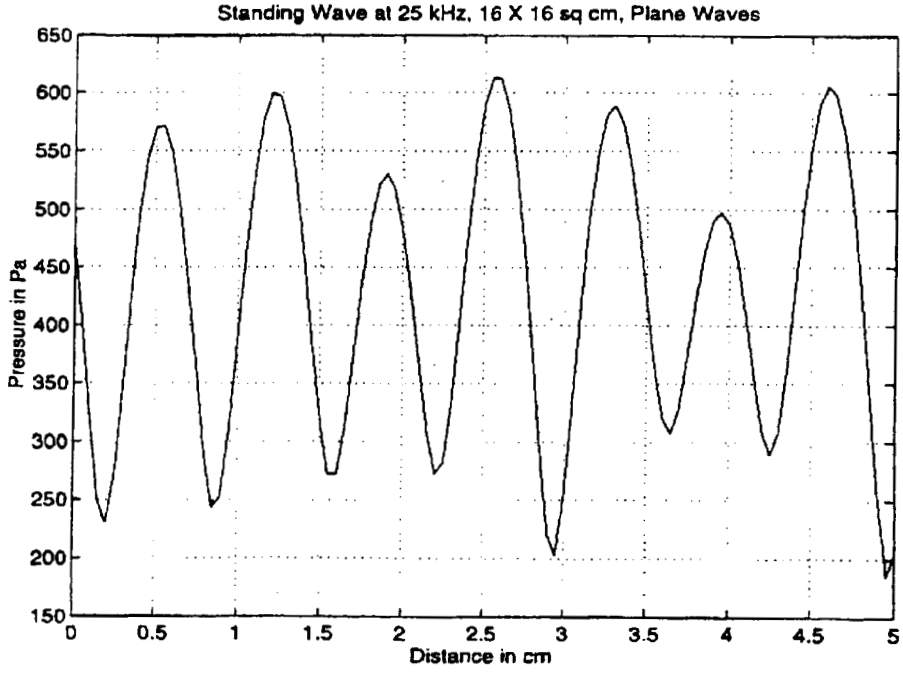

Figure 3-3.2 Standing wave at 25 kHz for 16 X 16 cm^2

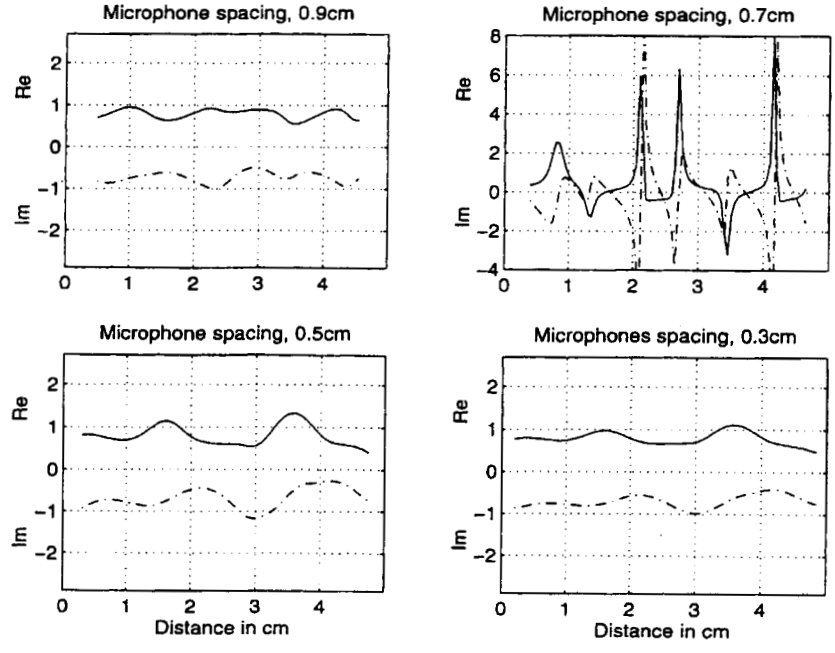

Figure 3-3.3 Variation in impedance measurement with distance and microphone spacing. Target impedance = 1.5 -1.5j

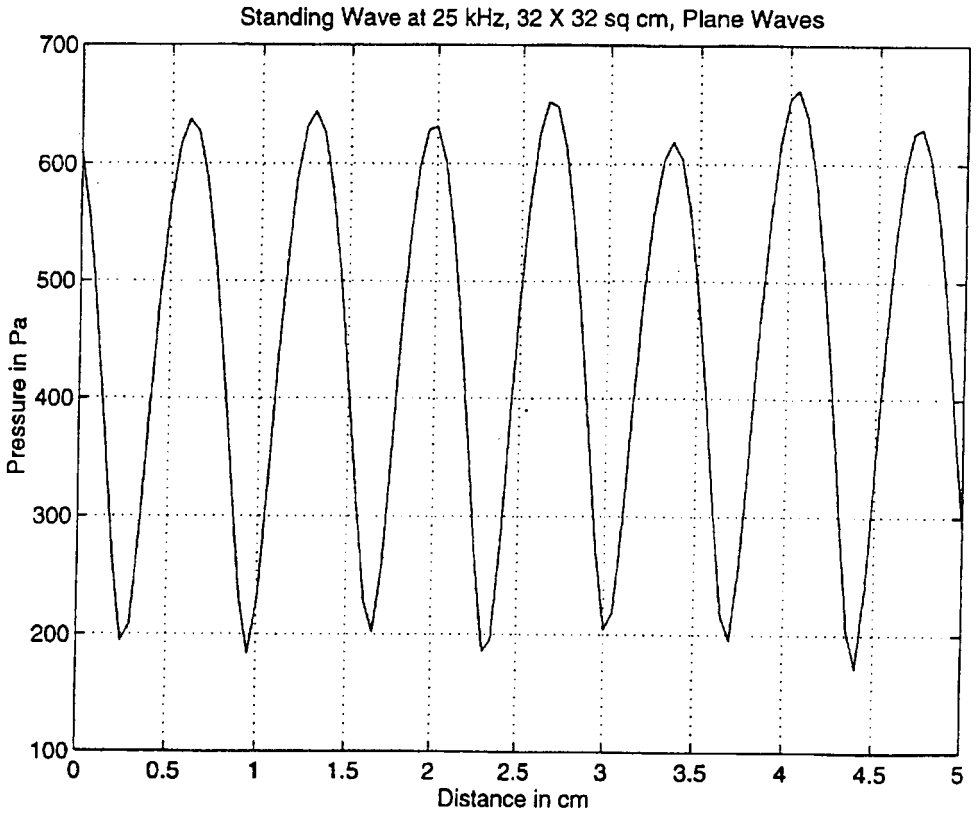

Figure 3-3.4 Standing wave at 25 kHz for 32 X 32 cm^2

These results show that the 16 X 16 cm^2 grid is not sufficiently large to yield a uniform standing wave above the reflecting plane. To understand the problem of insufficient size, a grid of 32 X 32 cm^2 was modeled and the analysis was repeated keeping the other system parameters constant. Figure 3-3.4 shows the results for the 32 X 32 cm^2 grid.

The standing wave obtained for the 32 X 32 cm^2 grid is more uniform than the one shown in Figure 3-3.2. Figure 3-3.5 shows the impedance obtained for the standing wave in Figure 3-3.4. The impedance obtained using Eq. 3-2.4 is approximately equal to the chosen value of 1.5 -1.5j. Furthermore, it can be seen that the results improve if the points that are chosen for impedance calculation are closer to the sample. Also, the impedance gets better as the distance between the two probes is decreased. This analysis verifies that the 32 X 32 cm^2 grid establishes a steady standing wave and reliable measurements can be made using a plane wave source.

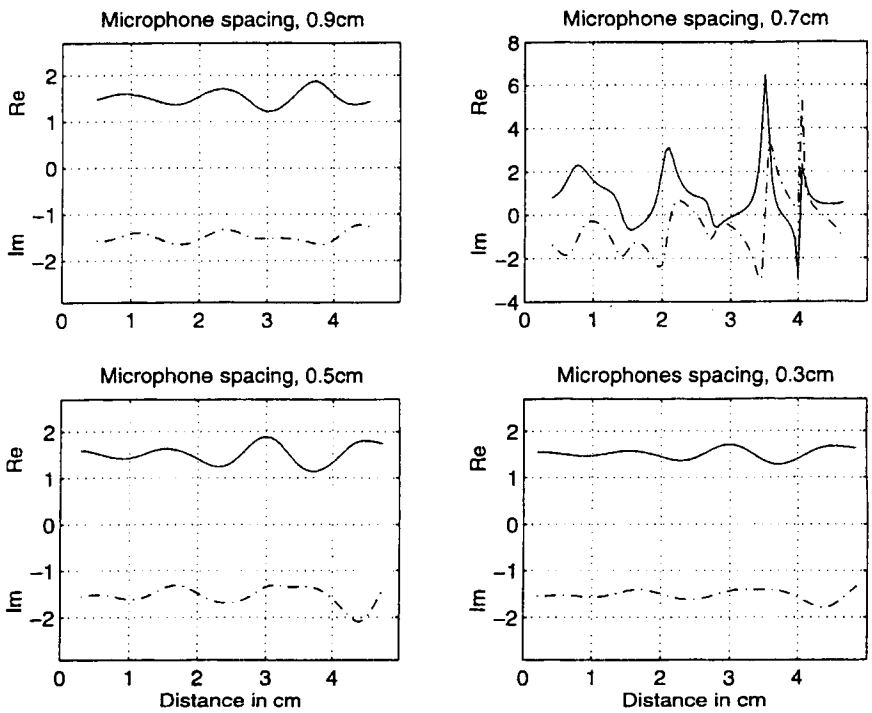

Figure 3-3.5 Variation in impedance with distance and microphone spacing. Target impedance = 1.5 - 1.5j.

Similar simulations were carried out on the 32 X 32 cm^2 grid by replacing the plane wave source with a spherical wave source. The effect of the distance of the sound source from the reflecting plane is an important consideration for a spherical wave source. Far from the source, the sound wave approximates a plane wave. However, when the source is near to the grid, the grid may experience a nonuniform sound pressure due to the sound directivity. In addition, as the sound source is moved away from the reflecting plane, the sound pressure level (SPL) decreases which, in turn, changes the measured impedance for non-linear samples. Thus, it becomes necessary to determine the effect of distance of the sound source from the sample such that the source directivity and distance will not affect the measurement and yet achieve a high SPL.

Two separate simulations were carried out with the sound source placed 50 cm and 150 cm from the reflecting plane. Figure 3-3.6 shows the standing wave obtained for the simulation with the sound source placed 50 cm away from the 32 X 32 cm^2 grid with z=1.5-j1.5.

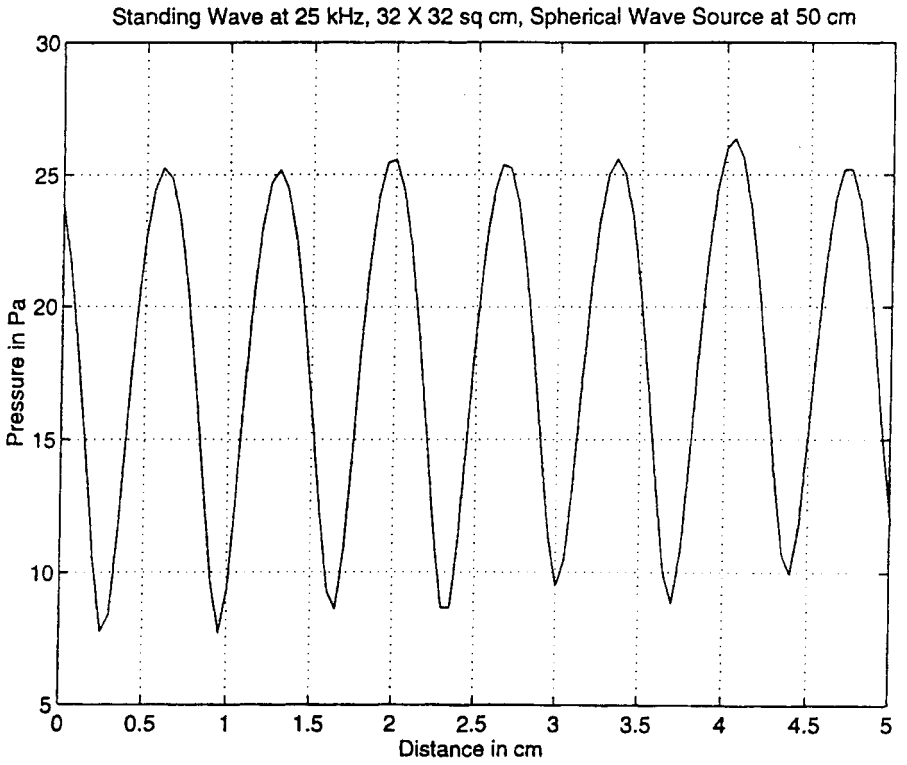

Figure 3-3.6 Standing wave at 25 kHz for 32 X 32 cm^2 sample, source at 50 cm

It can be seen that the standing wave is very uniform. Figure 3-3.7 shows the impedance calculated from this standing wave. From the results of this simulation, it can be concluded that a source-to-sample distance of at least 50 cm is sufficient to yield good results for impedance.

Figure 3-3.8 and 3-3.9 show the results of the simulation with the sound source placed 150 cm away from the reflecting plane. The standing wave obtained for the 32 X 32 cm^2 grid is very uniform. The impedance obtained using Eq. 2.4 for the standing wave shown in Figure 3-3.8 is approximately equal to the chosen value of 1.5 - 1.5j. The results shown in Figures 3-3.7 and 3-3.9 with the sound source placed at 50 cm and 150 cm from the sample respectively, are comparable. Thus, the results are not affected if the sound source is placed within 50 cm to 150 cm of the sample.

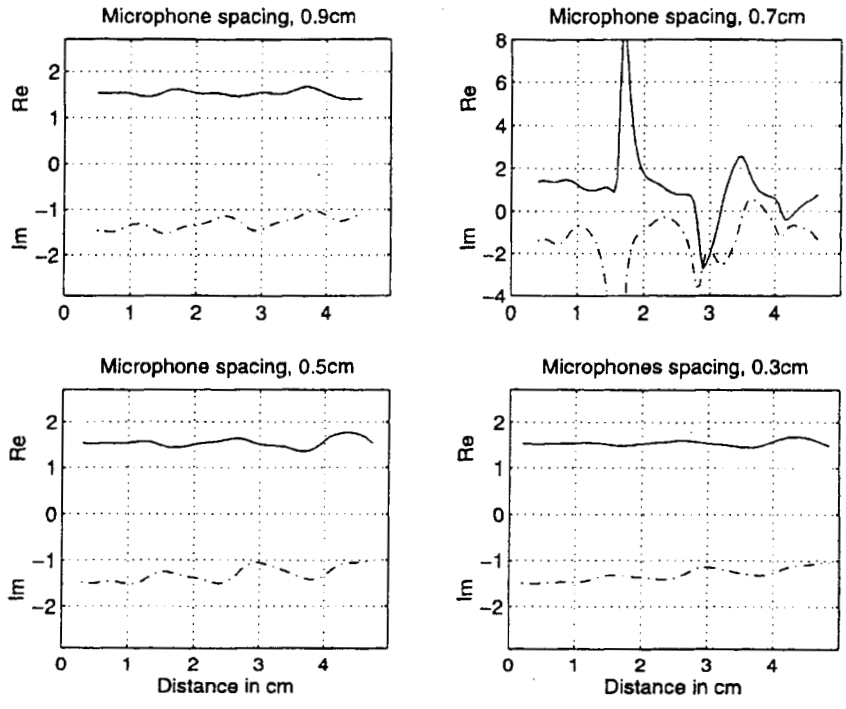

Figure 3-3.7 Variation with impedance with distance and microphone spacing

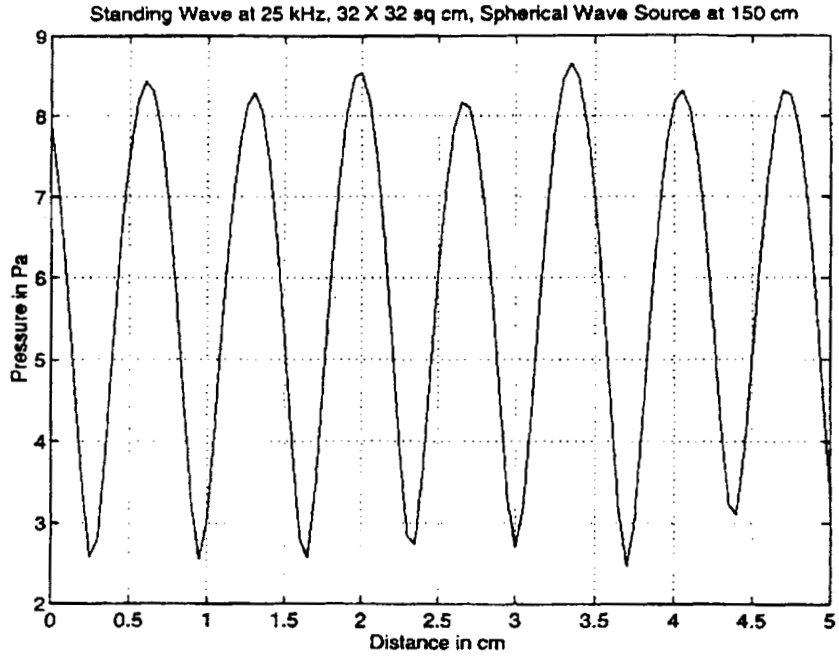

Figure 3-3.8 Standing wave at 25 kHz for 32 X 32 cm^2 sample, source at 150 cm

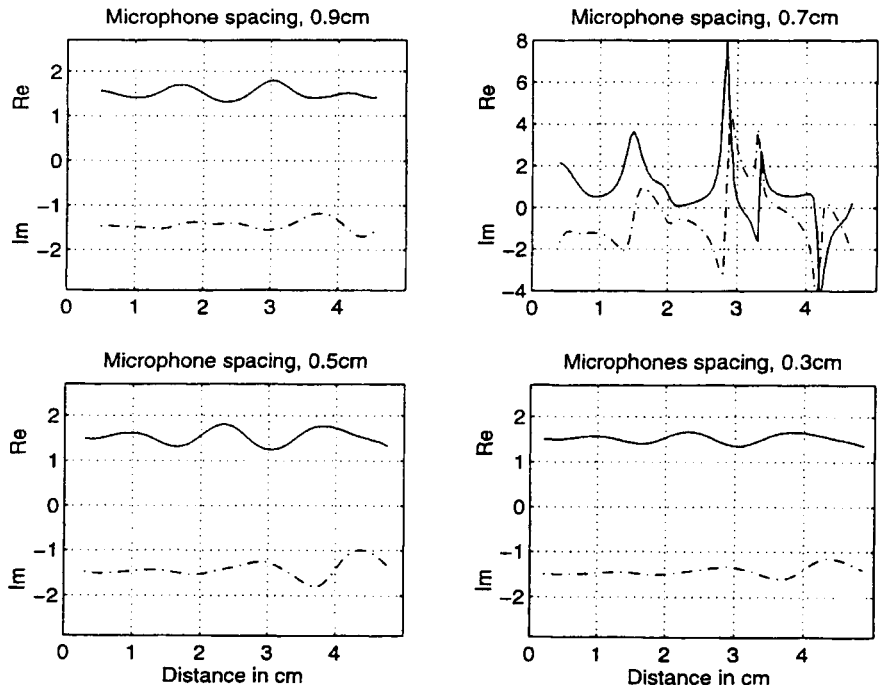

Figure 3-3.9 Variation in impedance with distance and microphone spacing

3.3.3 Scattering of sound

At very high frequencies, the scattering of sound from the microphone can alter the sound field which will result in erroneous measurements. One-quarter inch microphones used for making the measurements in the frequency range of 0-12 kHz will scatter sound at higher frequencies (12-25 kHz). It is desired to use microphone probes that are as small as possible to minimize the effect of scattering of the sound on the sound field. Special microphone probes could be designed to fit on the tips of one-quarter inch microphones to reduce the effective diameter of the microphones.

A boundary element model was made for two hypothetical microphone probes placed 0.6 cm from each other and at a distance of 3 cm from a rigid plane. A spherical wave sound source was placed at a distance of 50 cm from the reflecting plane. The sound field predicted by the BEM at 25 kHz is shown in Figure 3-3.10. The results show that the scattering of sound from the microphone probes at 25 kHz has little effect on the standing wave pattern.

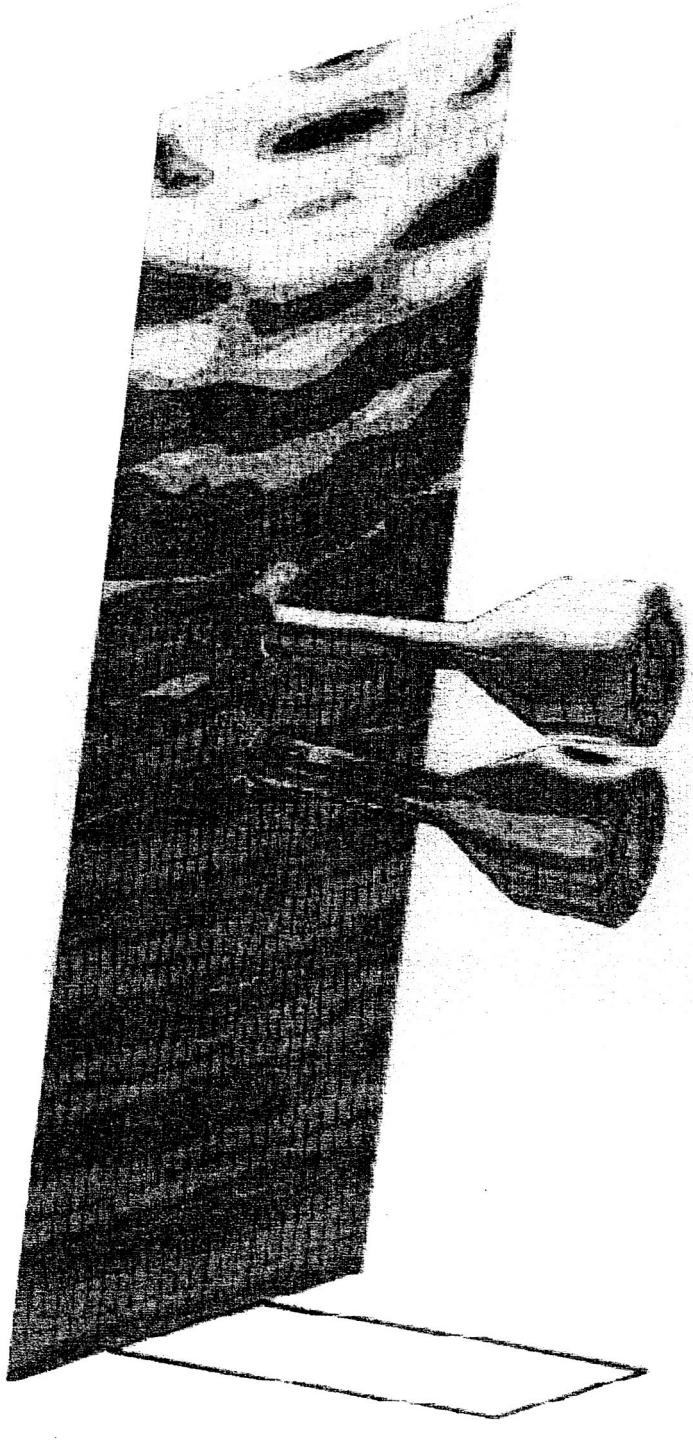

Figure 3-3.10 Scattering of sound from the microphone probes at 25 kHz.

3.4 Experimental test apparatus

The results of the simulations in Section 3 were used to design an experimental test apparatus (ETA). In this section the ETA is described. The ETA is shown in Figure 3-4.1

3.4.1 Sources and source level

A simple truss-structure with two columns supporting a beam was assembled. The simulation results for a spherical wave sound source revealed that if the sound source was placed at least 0.5 m from the sample the impedance results are reliable. The distance of the sound source from the sample was chosen as 1 m as shown in Figure 3-4.1.

A bracket hanging from a ball-in-socket joint was designed to hold the loudspeaker which was attached to a beam through a collar as shown in Figure 3-4.2. The ball-in-socket joint allowed the sound source to be oriented in any direction, which was necessary to make the directivity measurements of the sound source. The two end-columns were provided with solid footing to take the weight of the assembly and hold it upright on its own.

Two sound sources were used in the tests. The first was a 30 watt modified "bookshelf speaker" with a diaphragm diameter of 3 inches. This source produced an overall sound level of approximately 95 dB (Lin) at the sample. A second sound source, a JBL driver having a diaphragm diameter of 1 inch and a capacity of 50 watts was also used. The JBL driver, shown in Figure 3-4.3, produced a sound level of approximately 100 dB at the sample.

The relationship between the sound power W of a point source and the sound pressure p_{rms} produced at a distance r in a free field is

$$W = \frac{4\pi r^2 p_{rms}^{\ 2}}{\rho_0 c} \tag{3-4.1}$$

At a distance of r = 1 m, a source having 40π watts of acoustical power could be expected to produce a sound pressure level of approximately 130 dB, a typical level reached in aircraft engine applications. Because the conversion of energy to sound is quite inefficient (loudspeakers have efficiencies in the 1-10 percent range), mechanical or electrical input power must be 5 to 10 times this value to achieve levels of approximately 130 dB.

3.4.2 Microphone holder

In the free field measurement technique, the microphones are held a few centimeters above the reflecting plane with the distance between the two microphones constant. A fixture was designed such that a column bar supporting a cantilever beam stands upright on the floor, as shown in Figure 3-4.1. At the free end, the cantilever bar supports the microphone holder, which holds the microphones separated through a fixed distance. Two such microphone holders were designed to make measurements for two different frequency ranges. The first microphone holder had a spacing of one inch, and the second had a spacing of 0.236 inch.

3.4.3 Microphones

To overcome the problem of sound scattering from the microphones at high frequencies, the microphone diameter should be as small as possible; however, microphone sensitivity decreases with size. Initially, microphones with 1/16 inch diameter were considered, but due to their very low sensitivity, reliable results could not be obtained using the two sound sources available for the tests. One-quarter inch microphones fitted with special microphone probes were also used. The probes used are shown in Figure 3-4.4. The probe used consisted of a conical section fitted to a one-quarter inch microphone and connected to a 1/8 inch diameter tube.

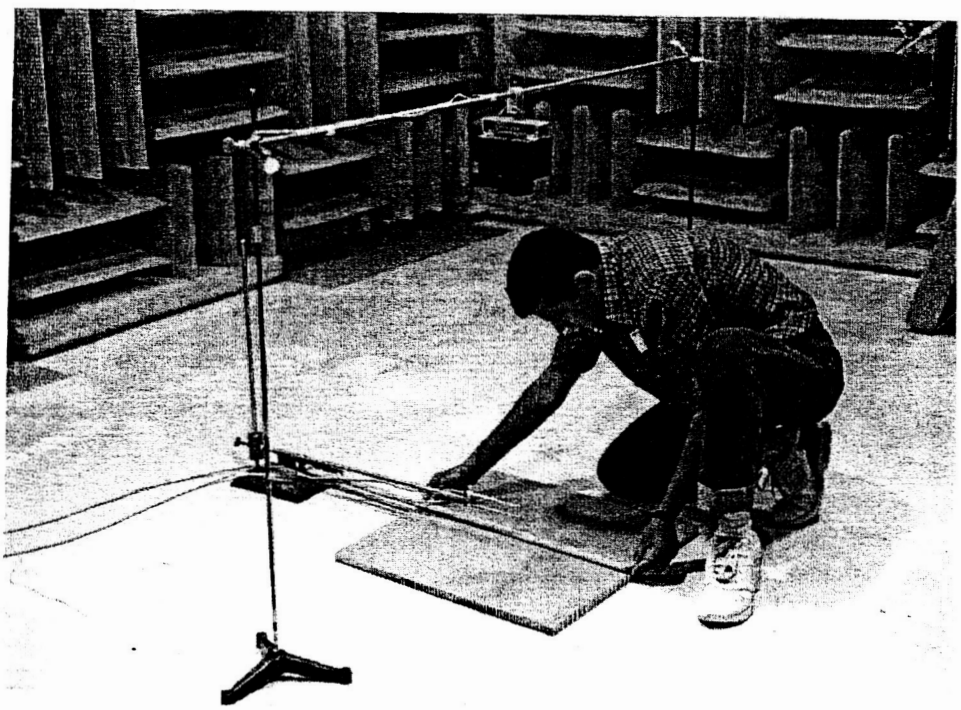

Figure 3-4.1 Experimental setup for a test on a single degree of freedom liner in a hemi-anechoic chamber

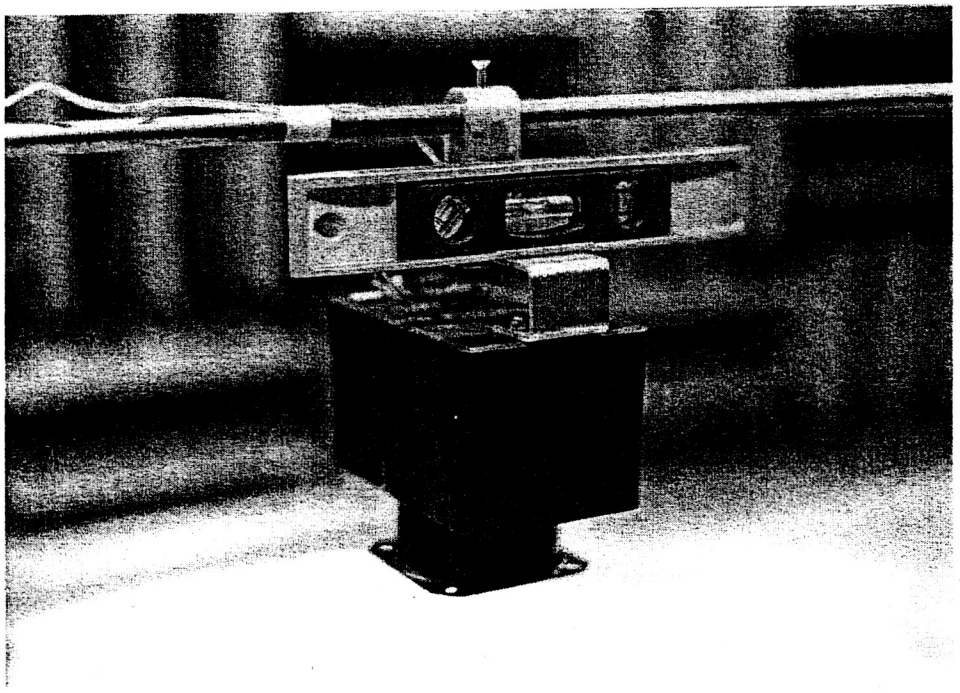

Figure 3-4.2 A 30 watt modified bookshelf speaker attached to a ball-in-socket joint.

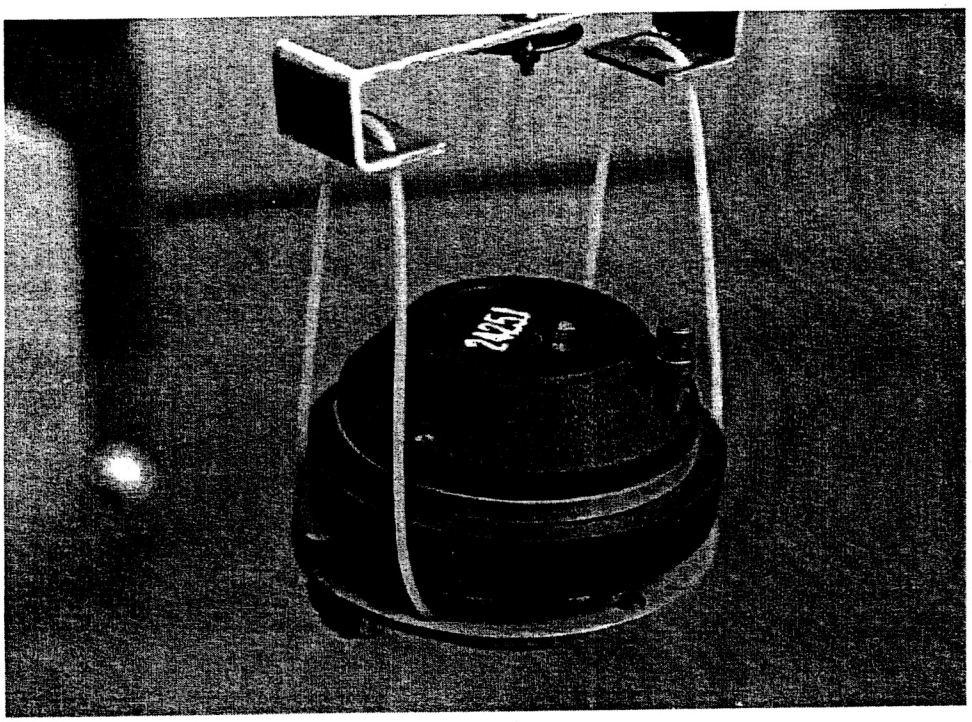

Figure 3-4.3 A JBL 50 watt driver

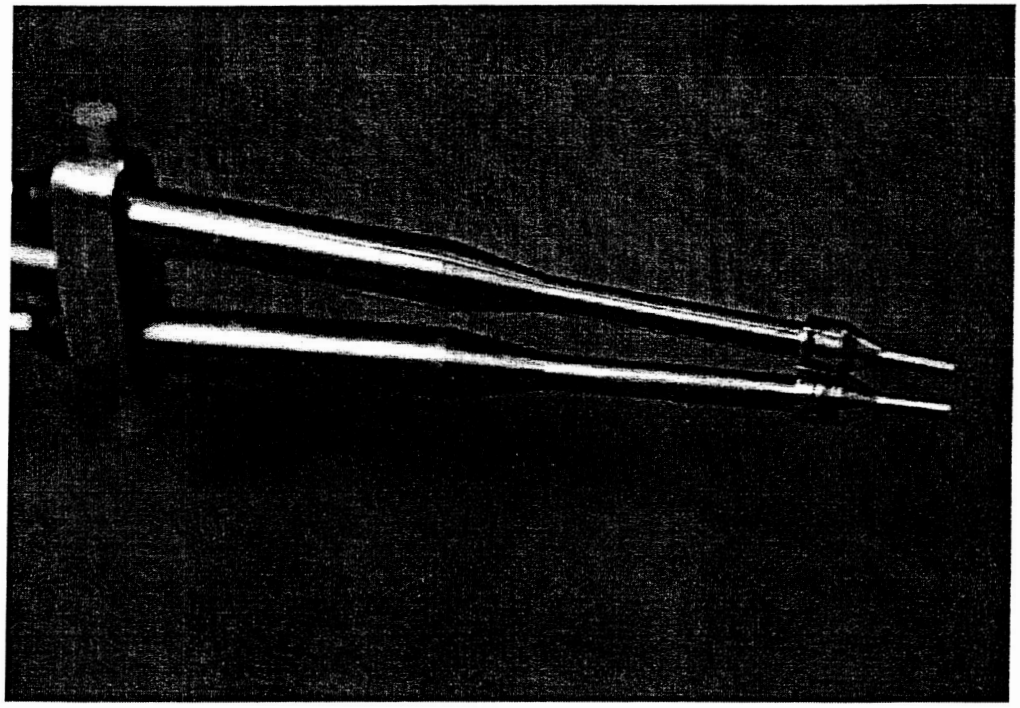

Figure 3-4.4 Microphone probes fitted over one-quarter inch microphones

3.5 Experimental Investigation

In this section, measurements made in an impedance tube at lower frequencies (< 5 kHz) are compared with measurements made in the free field. Also discussed is the effect of the sample size and the directivity of the source on the measurements. Lastly, a measurement of the impedance of a treatment panel is made in the 0-25 kHz range.

3.5.1 Transfer function measurements

The experimental setup for free field measurements is shown in Figure 3-5.1. The sound waves emitted by the sound source reflect from the sample and generate a standing wave pattern. The microphones M_1 and M_2 are placed above the sample and measure the sound signals at two different locations in the standing wave. The transfer function is the ratio of the Fourier transforms of the signals measured at M_2 over M_1. The signals measured contain the magnitude as well as the phase of the sound wave. Thus, if P_2 and P_1 are the Fourier transform of the acoustic pressures at the microphone locations M_2 and M_1 respectively, the transfer function is given by

$$H_{12} = \frac{P_2}{P_1}$$

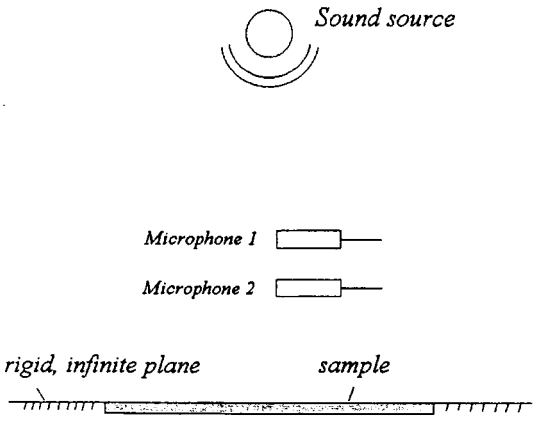

Figure 3-5.1 Experimental setup for free field measurement of impedance

The transfer function H_{12} contains the characteristics of the sample which reflects the sound waves and establishes a standing wave. As shown in Sections 3.5.1(a) and 3.5.1(b), H_{12} is a key parameter in determining the sample impedance by the free field method.

3.5.2 Calibration microphone function

Two microphones exposed to the same sound signal will yield different measurements owing to the fact that they have different sensitivity; the sensitivities of two microphones vary

in magnitude as well as phase. While making transfer function measurements, it is necessary to know the sensitivity of the two microphones to determine a true transfer function measurement. The microphone calibration function is defined as a complex quantity that is the ratio of the microphones' magnitude sensitivities and the difference in phase measured by the two microphones. The calibration function, when multiplied by any other transfer function measurement made by the same pair of microphones gives the true transfer function for that experiment.

The microphone calibration function may be determined by measuring the transfer function H_{12} for an absorbing sample by placing the microphones in an impedance tube excited by random noise as shown in Figure 3-5.2. Then, the positions of the two microphones are exchanged such that M_2 takes the position of M_1 and vice-versa, and a similar transfer function measurement is made for the same absorbing sample without disturbing the other system parameters (ASTM, 1990). Because all the other system parameters are retained and the same sample is used for this second measurement, the new transfer function H_{21} is the reciprocal of H_{12} and the microphone calibration function K is given by,

$$K = \sqrt{H_{12}H_{21}}$$

It is important to note that the calibration function K is independent of the sample used for making the transfer function measurements H_{12} and H_{21}. Moreover, the microphone calibration function is frequency dependent. Transfer function measurements H_{12} and H_{21} are shown in Figure 3-5.3(a) and 3-5.3(b), respectively.

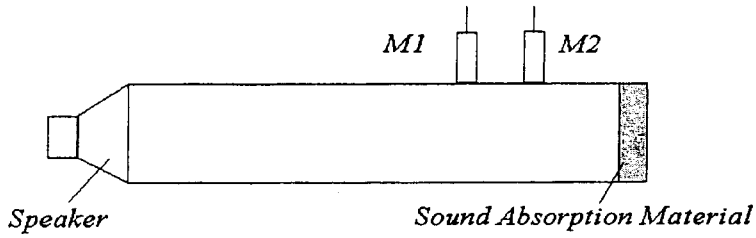

Figure 3-5.2 Measuring the microphone calibration function in an impedance (plane-wave) tube

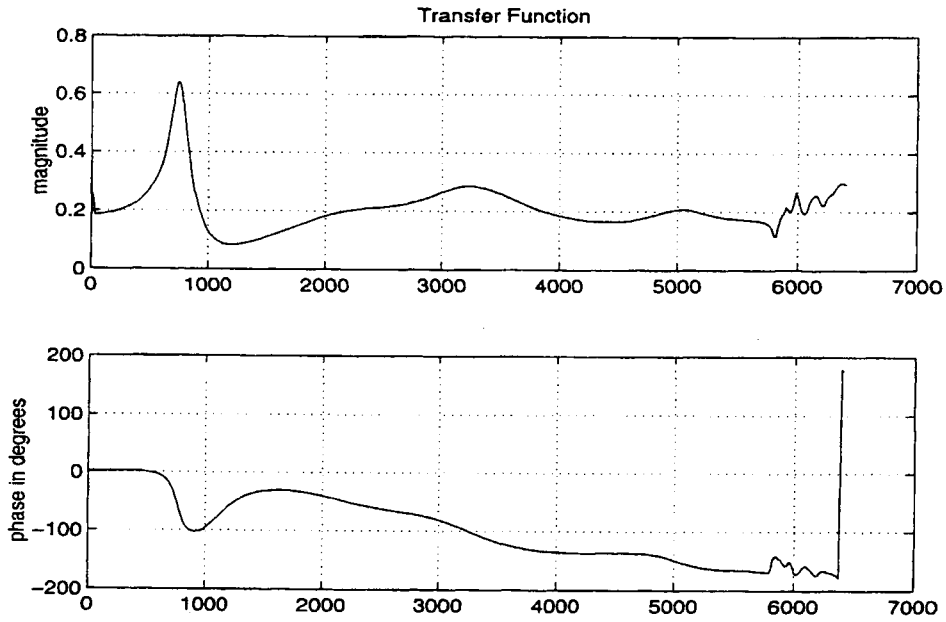

Figure 3-5.3(a) **Transfer function measurement for a foam sample**

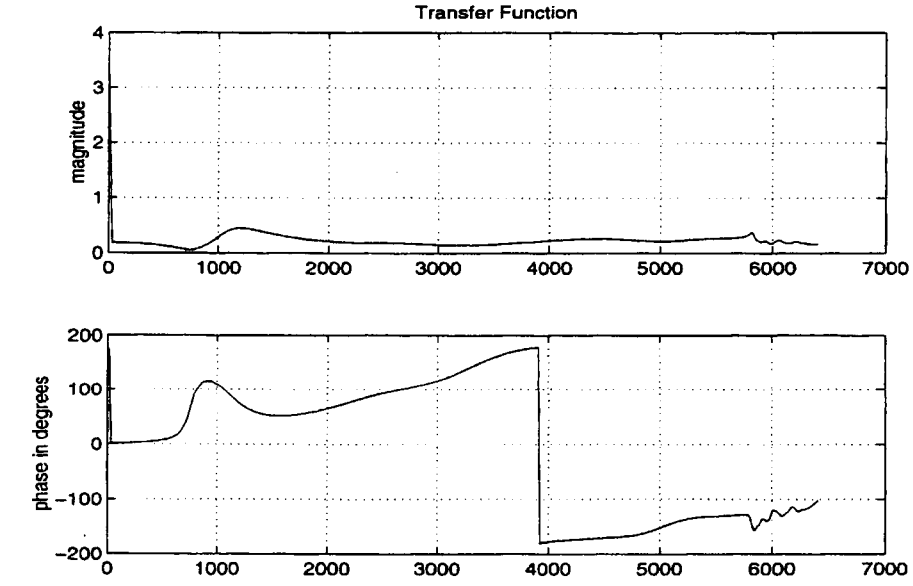

Figure 3-5.3(b) **Transfer function measurement after switching the microphone position**

The microphone calibration function K obtained from the transfer function measurements shown in Figure 3-5.2 is shown in Figure 3-5.3(c).

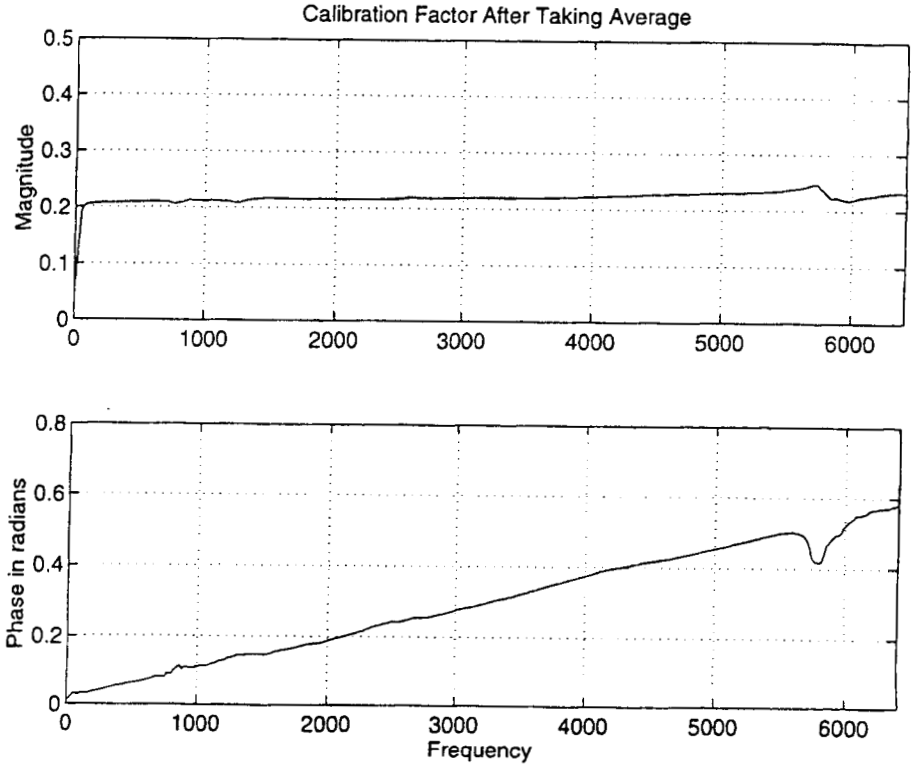

Figure 3-5.3 (c) Microphone calibration function (impedance tube) expressed in terms of magnitude and phase

As mentioned above, this calibration can be used to correct the transfer function measurement made for any material sample for the same frequencies of analysis using the same microphone pair; if h is the transfer function measurement made for some material sample, the true transfer function can be written as

$$H = Kh$$

where H is the true transfer function of the material sample.

The calibration function shown in Figure 3-5.3 was evaluated by making measurements in an impedance tube. At frequencies above the tube cut-off, the calibration cannot be determined from the measurements in an impedance tube. So, the feasibility of measuring the microphone calibration function at high frequencies in the free field is an important consideration. Figure 3-5.4 shows the microphone calibration function evaluated by making the transfer function measurements H_{12} and H_{21} in a free field, as shown in Figure 3-5.1

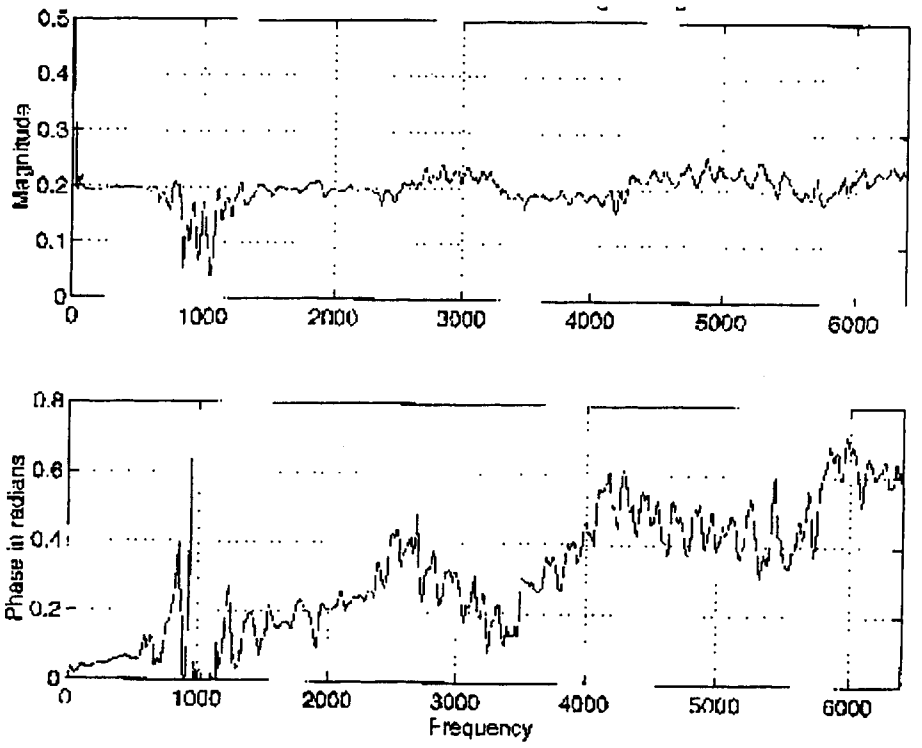

Figure 3-5.4 Microphone calibration function evaluation from the free field data for a non-anechoic environment

The comparison between the results shown in Figures 3-5.3 and 3-5.4 shows that the microphone calibration function measured from the impedance tube and the free field data are in general agreement with each other, but the microphone calibration function from the impedance tube is much smoother than the one obtained in the free field. The lack of smoothness in Figure 3-5.4 is due to the lower coherence of free field measurements.

3.5.3 The effect of sample size

A glass wool sample was used to perform the experiments to determine the effect of sample size on measured impedance. Glass wool material is cheaply available to cut into the pieces of different sizes, as required; it is also easy to find the true absorption characteristics using the ASTM E-1050 procedure at lower frequencies (ASTM, 1990). Glass wool material, 0.6 inches thick, was cut into two pieces, 4 X 4 ft^2 and 2 X 2 ft^2. The experiments were carried out in a hemi-anechoic chamber with a loudspeaker sound source placed 1 m away from the glass wool sample, and two 1/4" microphones were used to pick up the sound signals. The microphone calibration function was determined in the 0-12 kHz frequency range using the free field method as explained in the previous section. The distances of the microphones were accurately measured using slip gauges and the absorption coefficient was calculated using Eq. 3-2.3.

The impedance and absorption coefficient are shown in Figures 3-5.5(a) and 3-5.5(b), respectively. It can be concluded that a sample size of 2 X 2 ft^2 is sufficiently large for measurements up to 12 kHz. The microphone spacing for these experiments was 1 inch which

is approximately one-half wavelength at 6.75 kHz, thereby making the impedance indeterminate at 6.75 kHz (see Eq. 2.4).

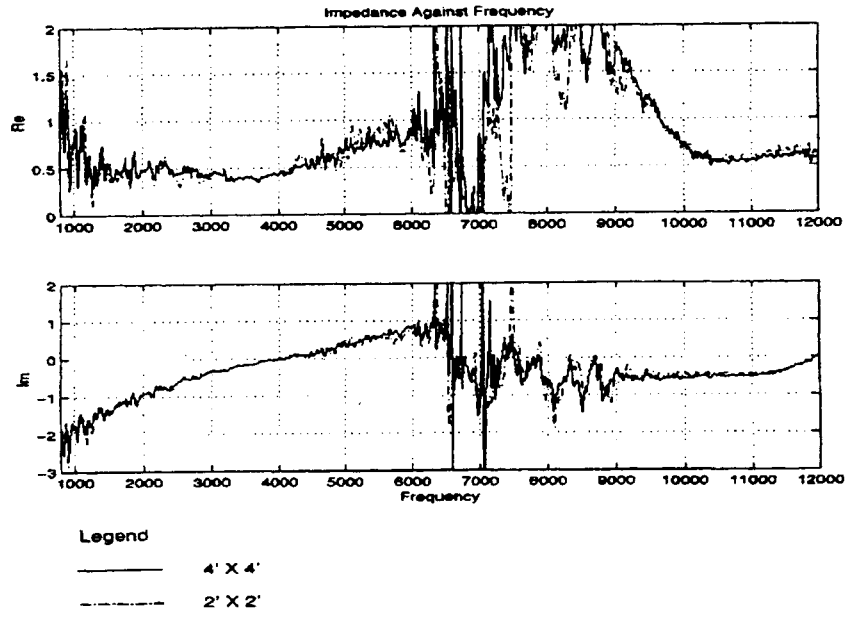

Figure 3-5.5(a) **Comparison of the impedance for two sample sizes**

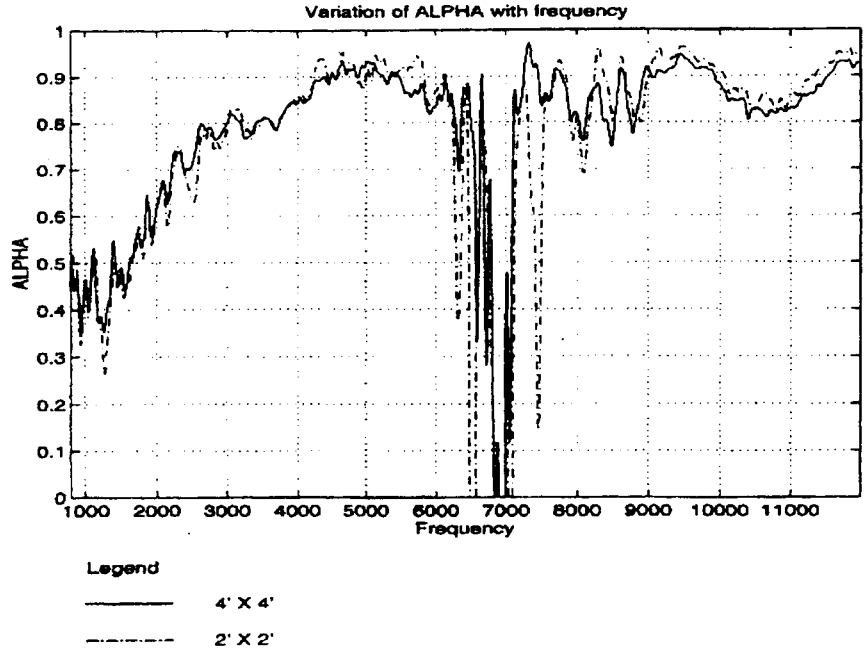

Figure 3-5.5(b) **Comparison of the absorption coefficients for two sample sizes**

3.5.4 Directivity of the source

The absorption coefficient determined from Eq. 3-2.3 is based on the assumption that the sound waves emitted by the source are spherical. Usually sound wave propagation in the direction of the oscillation of the diaphragm is more prominent than any other direction, and the sound field will be uniform within a certain angle of the source. If the sound source is tilted, such that the direction of the oscillation of the diaphragm is at an angle with the normal to the sample, the spherical wave assumption may be violated.

To determine the effect of source directivity, measurements were made with the sound source tilted at two different inclinations, 0 and 10 degrees. A glass wool sample, 4 X 4 ft^2 was used as the sample. The absorption coefficient obtained for the two inclinations is shown in Figure 3-5.6(a) and 3-5.6(b). The data in Figure 3-5.6 has been smoothed to make interpretation possible. The inclination of the speaker within 10 degrees did not seem to affect the results.

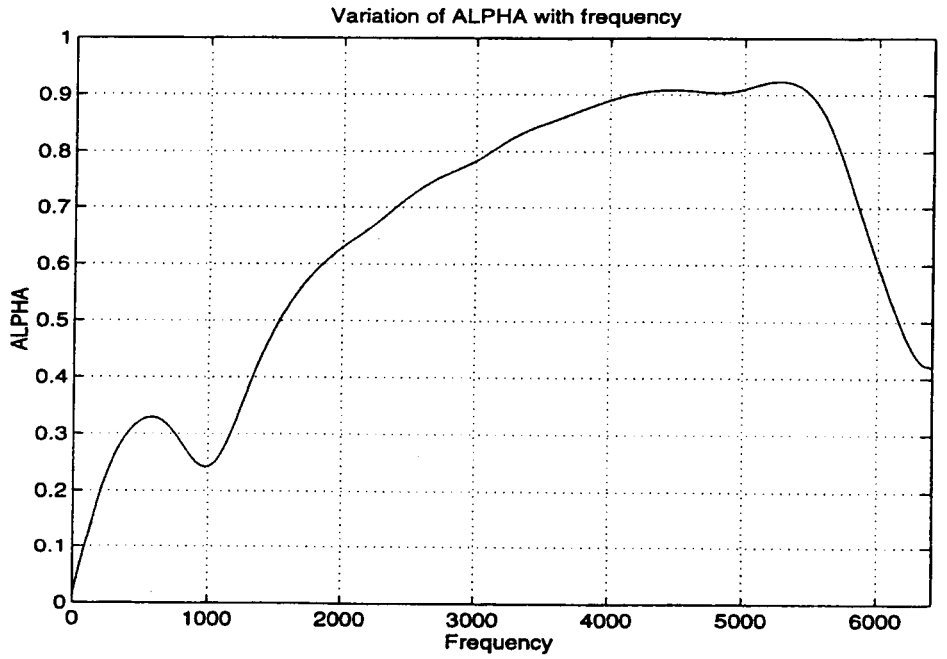

Figure 3-5.6(a) **Absorption coefficient with the source inclined at 0 degrees for glass wool sample**

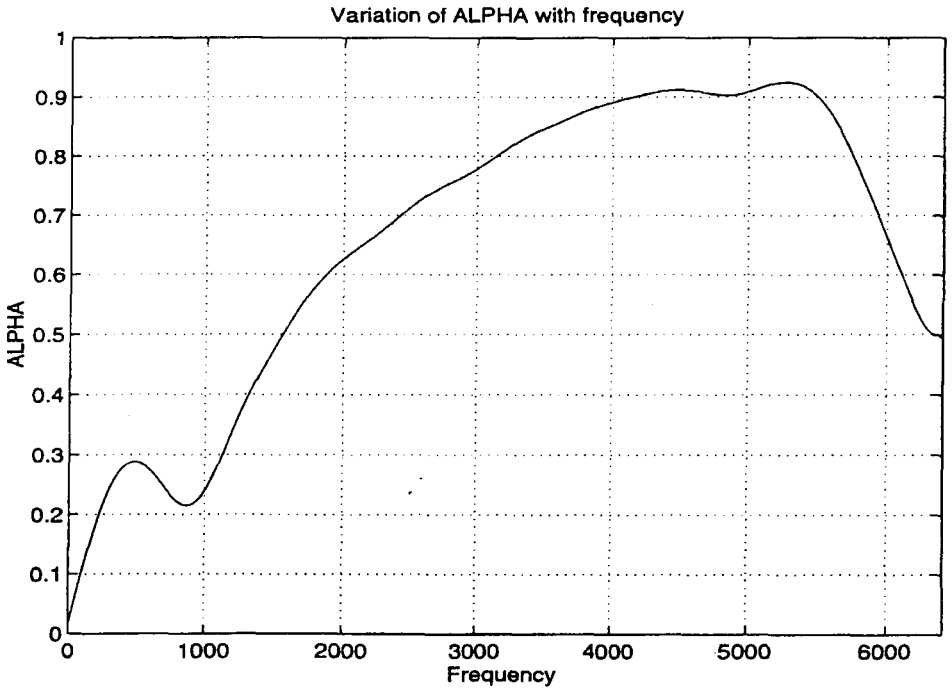

Figure 3-5.6(b) **Absorption coefficient with the source inclined at 10 degrees for glass wool sample**

3.5.5 Non-anechoic environments

For practical purposes, it is important to determine the viability of conducting free field impedance measurements in non-anechoic environments. An experiment was conducted to determine the absorption coefficient of a glass wool sample in a frequency range of 0-12 kHz in a hemi-anechoic chamber and in a laboratory room. The laboratory room had a area of 180 ft^2 and constructed of a concrete floor and concrete block walls. The results are shown in Figure 3-5.7. The results show that measurements made in non-anechoic environments give encouraging results.

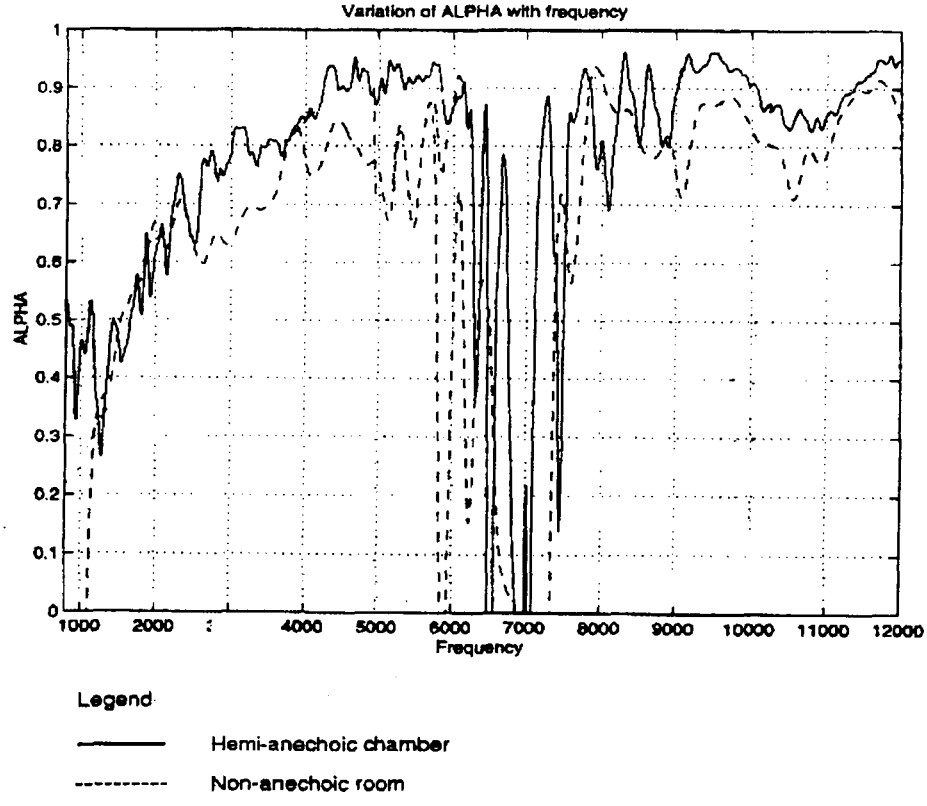

Figure 3-5.7 Comparison of the absorption coefficient for a hemi-anechoic chamber and a laboratory environment

3.5.6 Impedance of full-scale acoustic liners

Measurements were made on two samples of full-scale acoustic liners supplied by Rohr, Inc. One liner was a sample of DynaRohr with approximate dimensions of 16 in × 16 in. The other liner was a single degree of freedom liner with a hole size of 0.0365 inches, a hole spacing of 0.1095 inches and air-element depth of 0.727 inches. The second liner had dimensions of 24 in × 24 in.

Both samples were tested in a hemi-anechoic chamber using random noise in the 0-6400 Hz frequency range. A loudspeaker was used as a sound source, placed at a distance of 1m from the sample. The microphone calibration function was determined in a free field hemi-anechoic environment. One-quarter inch microphones were used to make the measurements. The results of the DynaRohr sample are shown in Figures 3-5.8 and 3-5.9 along with comparison data obtained from a 3.0 cm impedance tube test conducted by Rohr. The results for the single degree of freedom liner are shown in Figures 3-5.10 and 3-5.11. SPL levels given are overall levels at the surface of the liner.

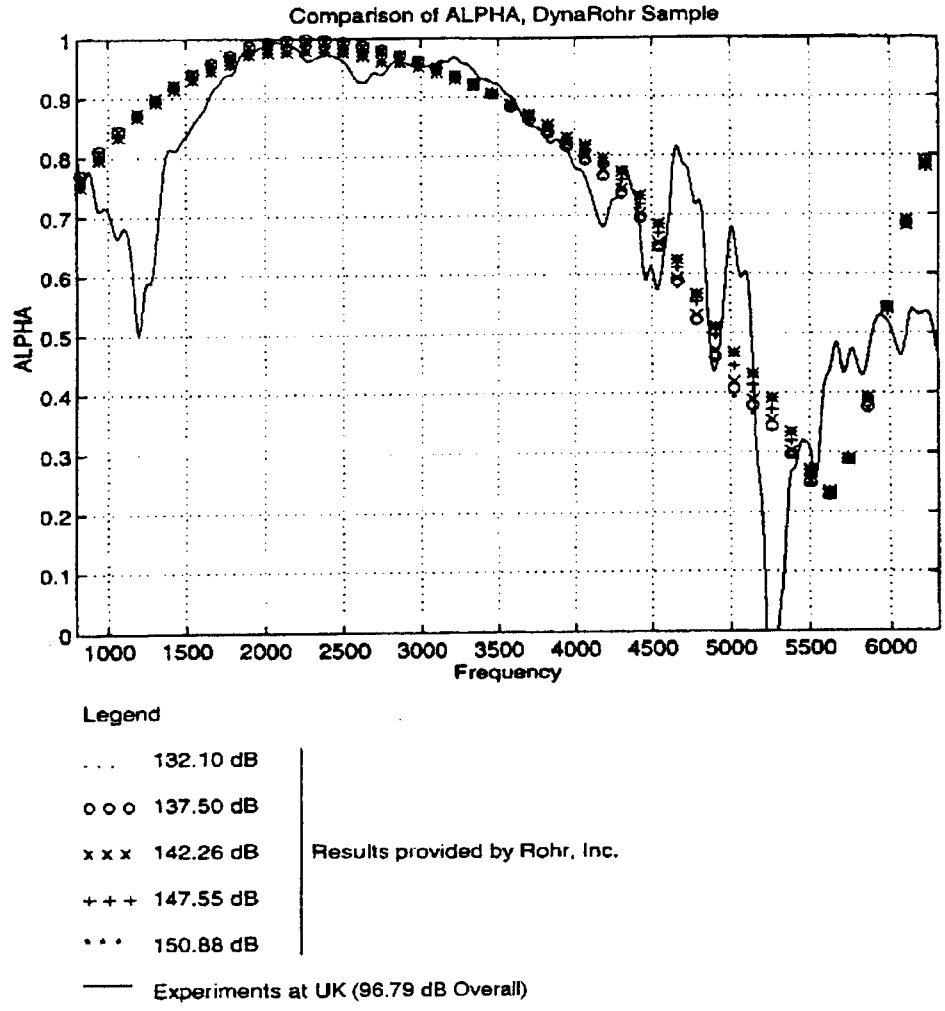

Figure 3-5.8 Comparison of the absorption coefficient from free field measurement with the Rohr data from the 3 cm impedance tube, SDOF DynaRohr sample.

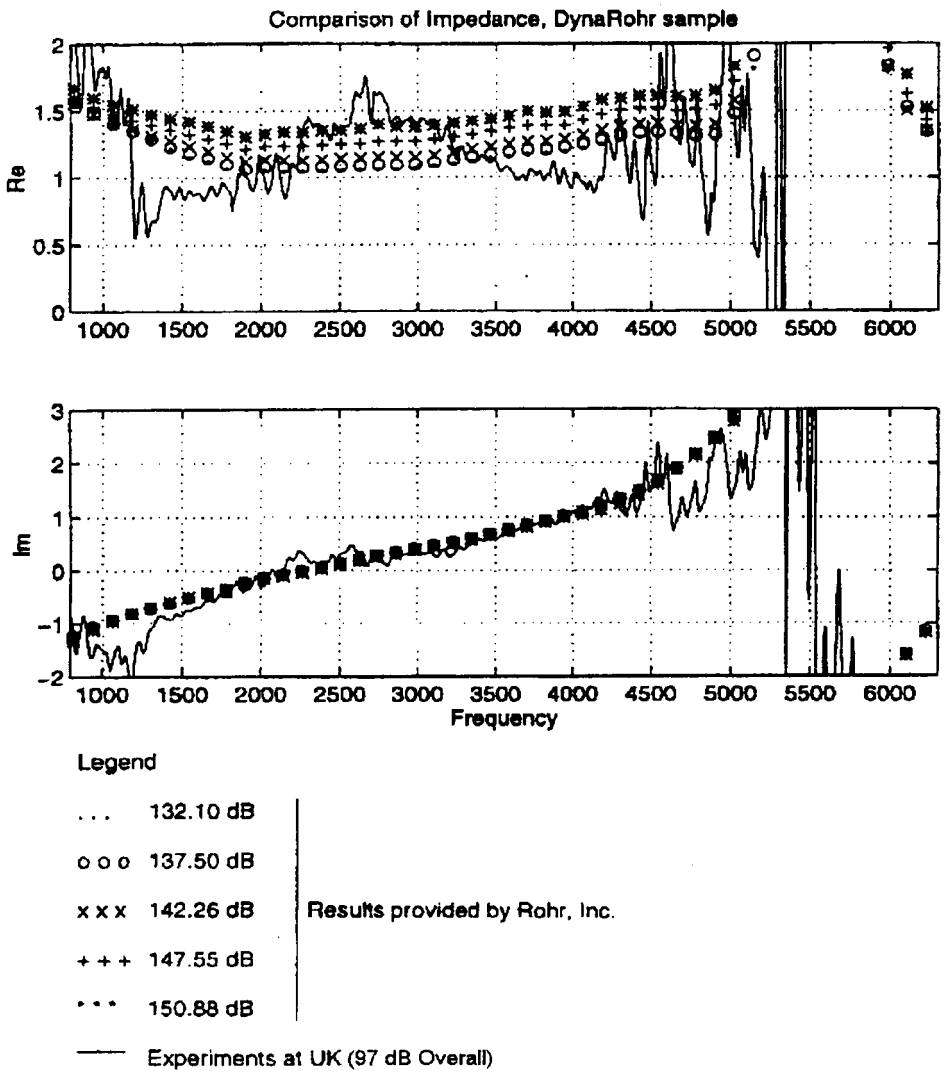

Figure 3-5.9 Comparison of the impedance from free field measurement with the Rohr data, SDOF DynaRohr sample.

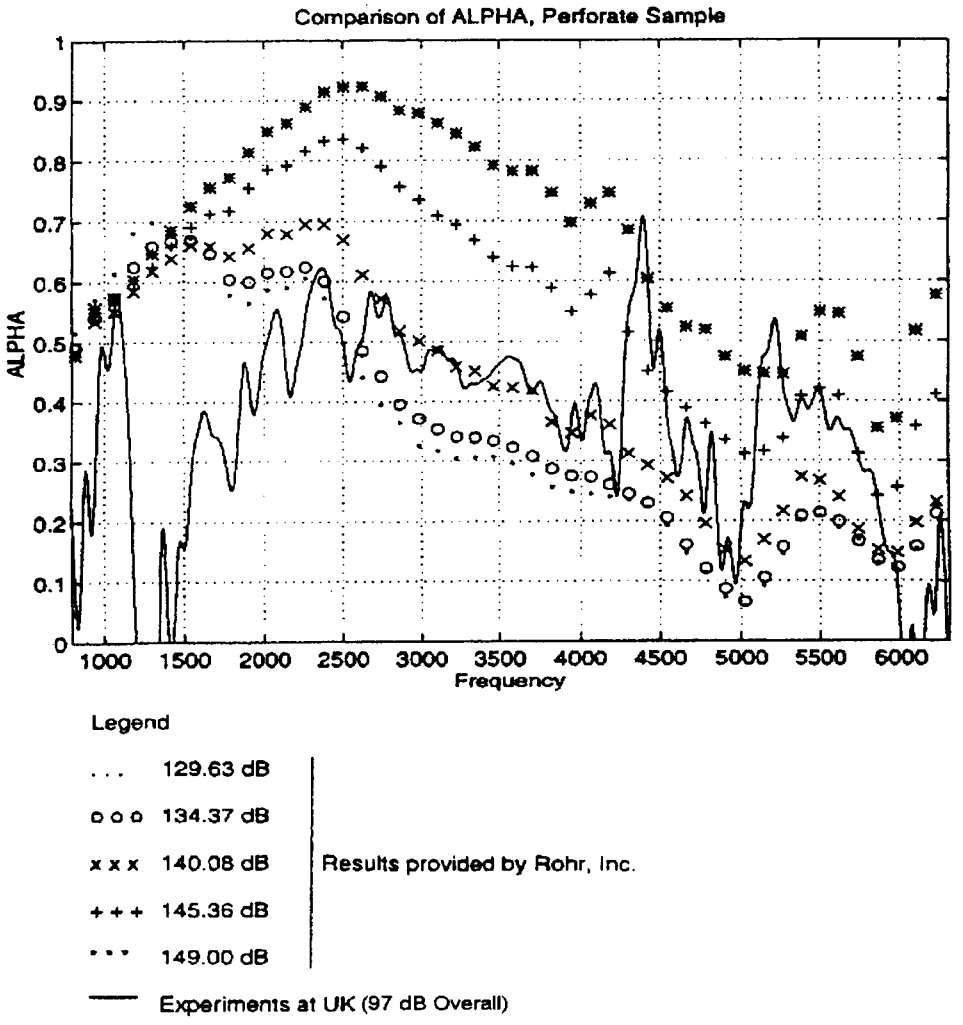

Figure 3-5.10 Comparison of the absorption coefficient from free field measurement with the Rohr data, from 3 cm impedance tube, SDOF perforate sample.

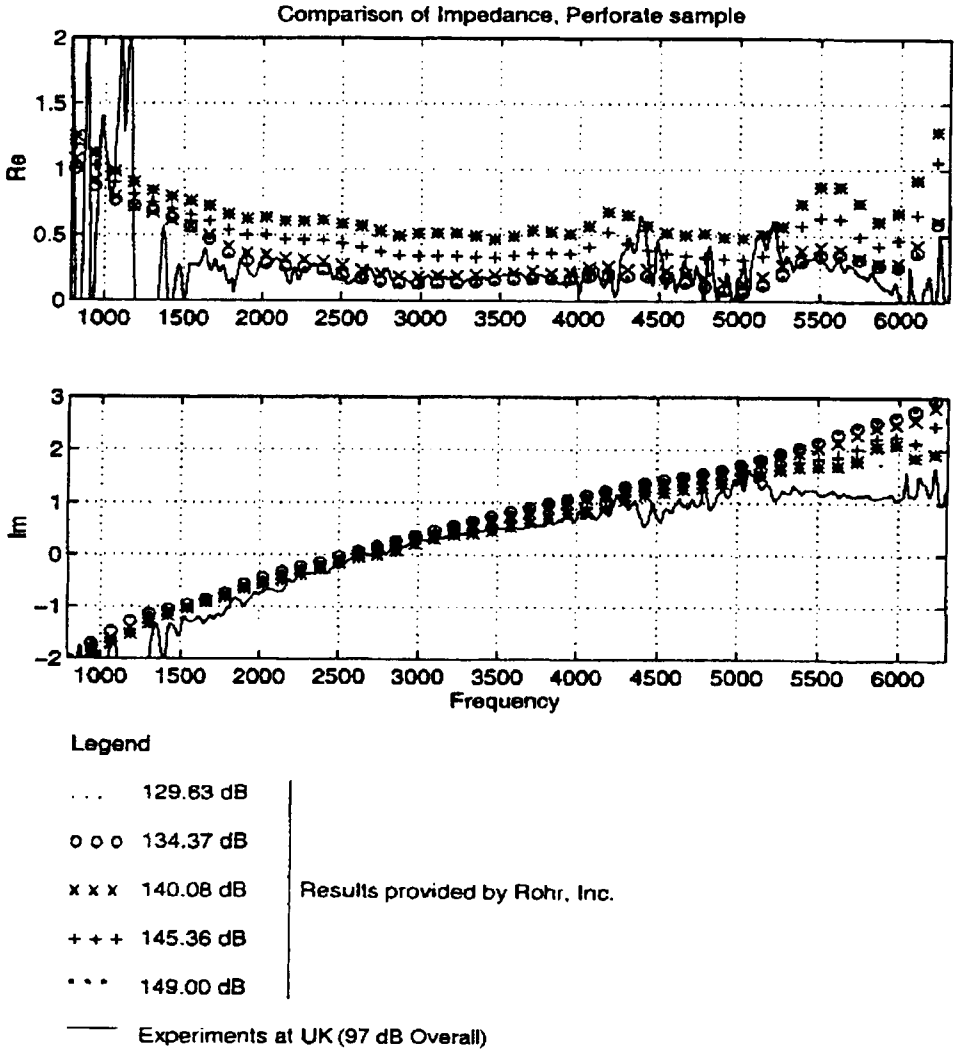

Figure 3-5.11 Comparison for the impedance from the free field measurement with the Rohr data for 3 cm impedance tube, SDOF perforate sample.

3.5.7 Extension to 25 kHz

Measurements of impedance using the free field method at 25 kHz were problematic without a high-intensity broadband source. However, a JBL 100 watt driver which had a measurable output at 25 kHz at 1 m was used for a preliminary test. The probe tips shown in Figure 3.4-4 were used with one-quarter inch microphones. Figure 3-5.12 shows the microphone calibration function for the one-quarter inch microphones fitted with the probe tips. The discontinuities in the microphone calibration function near 12 kHz is likely due to a resonance in the probe tip canal.

The absorption coefficient and impedance for the DynaRohr sample are shown in Figures 3-5.13 and 3-5.14, respectively. No data were available for comparison above 6500 Hz.

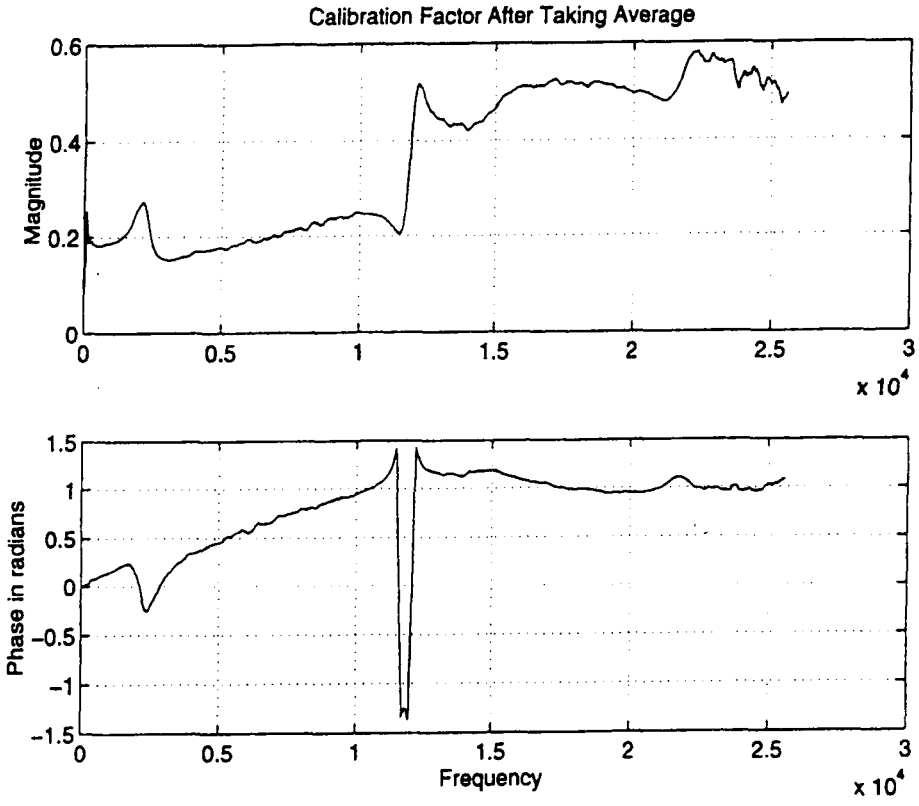

Figure 3-5.12 Microphone calibration function for full bandwidth (0-25 kHz)

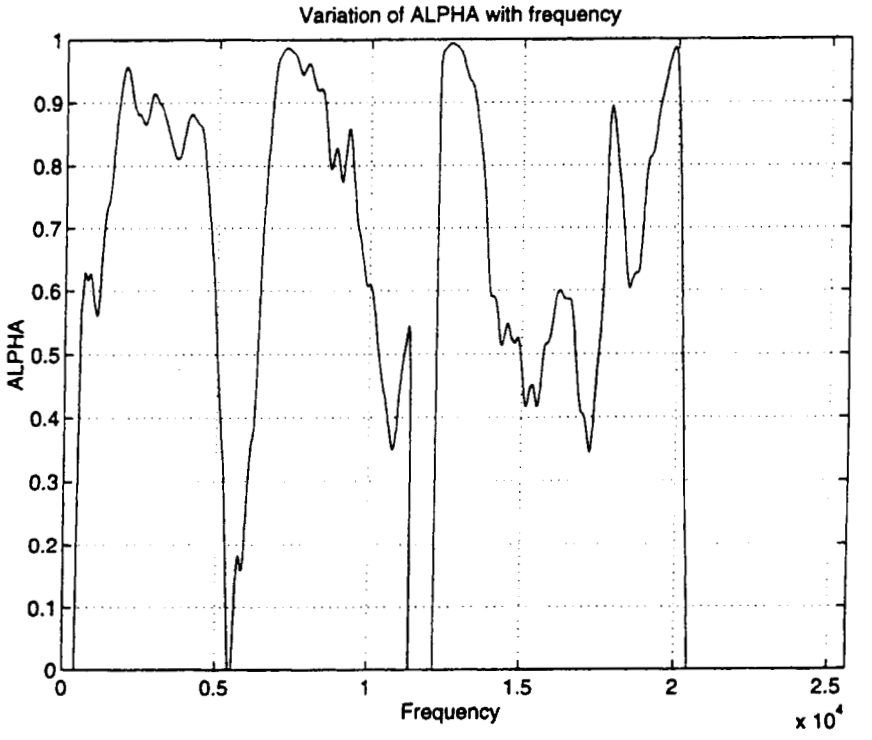

Figure 3-5.13 Absorption coefficient for DynaRohr for full bandwidth (0-25 kHz)

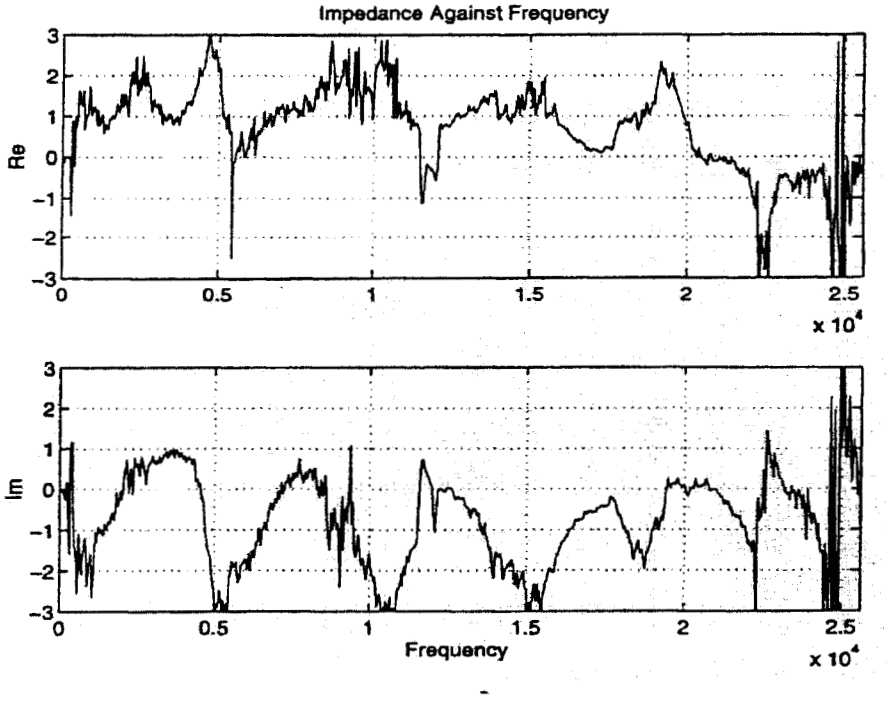

Figure 3-5.14 Acoustic impedance for DynaRohr for full bandwidth (0-25 kHz)

3.6 Summary and Conclusions

In this project the free field method has been evaluated for measuring the acoustical impedance of scale-model aircraft engine liner treatments at high frequencies. Such treatments are used in the Ultra-High-Bypass Ratio Propulsion Simulator (UPS) where the frequencies may extend to 25 kHz. A literature search revealed that none of the existing methods for the measurement of impedance, including the free field method, has been used above approximately 8 kHz. The literature search also revealed that the choice of basic experimental parameters of the free field method, such as sample size, source and microphone placement, and source directivity has not been investigated even at low frequency.

In an effort to understand certain experimental parameters, a simulation of the free field method using the boundary element method was conducted. The simulation showed that at 25 kHz the sample size should be approximately 12 inches square or larger in order to establish a uniform sound field in the vicinity of the microphones. The simulation further showed that the microphones should be no larger than approximately 1/16 inches in diameter to avoid distortion of the sound field due to diffraction at 25 kHz. Finally, the simulation showed that the microphones should be placed within a few centimeters of the sample and that the source should be at least one-half meter from the sample in order to determine accurately the impedance.

An experimental test apparatus (ETA) was constructed based on the results of the simulation and on findings from the literature search. The ETA consisted of a frame to support the source and a fixture to hold a pair of one-quarter inch diameter microphones over the center of the sample placed on the floor of a hemi-anechoic chamber. The ETA was evaluated by measuring the impedance and absorption coefficient of samples of glass wool in the 0-5 kHz frequency range and comparing the results with those obtained using the ASTM E-1050 "two-microphone impedance tube" method. Measurements of impedance were made in both a hemi-anechoic chamber and in a typical laboratory room. The impedance and absorption coefficient of a single degree of freedom liner and of a "linear" impedance liner (DynaRohr) supplied by Rohr were also measured in the 0-7 kHz range. Impedance data obtained by Rohr for both liners in an impedance tube were used for comparison.

The current project was able to shed some light on the feasibility of extending the free field method to frequencies of 25 kHz. In particular, a number of issues were addressed for the first time and additional issues have been defined for future study. These items are discussed below.

1. **The free field method**. While there are several variants of the free field method, all use a pair of closely-spaced microphones; however, an interesting departure from this is the cepstral method that uses a single microphone (Bolton, 1984). For the current project, the two microphone configuration was selected as it is the easiest to implement and because it is the free field analog of the well-established ASTM E-1050 method (ASTM, 1990). It is recommended that the two-microphone configuration be used for subsequent tests of the free field method.

2. **Source selection and location**. The free-field method places rather severe constraints on the source of sound as compared to the ASTM E-1050 method. This is because (1) the source

must have a frequency response up to 25 kHz, (2) the source must be able to produce a sound pressure level of at least 130 dB in a free field in order to measure the impedance of most non-linear liner treatments, and (3) the source must be reasonably small so that the spherical-wave assumption upon which the free field method is based is fulfilled. A source meeting these requirements was not available for the project and, indeed, may not exist. Instead, the impedance results in the current project were obtained using commercially available sources. It is recommend, therefore, that an effort be made to identify or develop a source meeting the requirements for the free field method.

3. **Minimum sample size**. Both the simulation and the experimental results showed that the sample size of approximately 12 x 12 inches square was adequate for measurements up to approximately 7 kHz. At higher frequencies it may be possible to reduce the sample size, but this cannot be confirmed without a source as described above. It is recommended that additional tests be conducted to determine the minimum sample size required at 25 kHz.

4. **Microphones**. Due to their low-sensitivity and the unavailability of a high-output source, 1/16 inch diameter microphones could not be used. Instead, the current project used one-quarter inch diameter microphones. Thus, measurements had to be confined to the 0-12 kHz frequency range. Probe tips that reduced the effective diameter of the microphones to 1/8 inch diameter were used with the one-quarter inch microphones in order to make measurements up to 25 kHz. However, these results were inconclusive as no comparison data were available. It is recommended that future measurements using the free field method be conducted with 1/16 inch diameter microphones and with a high-output source, as described above.

5. **Measurement environment**. Impedance tests were conducted in both a hemi-anechoic and a "typical" laboratory environment in the 0-12 kHz range at relatively low sound levels (approximately 100 dB). The results showed that it may possible to use the free field method in a non-hemi-anechoic environment if the source level is high (e.g., approximately 130 dB). It may also be possible to construct a small (about 1 meter cube) hemi-anechoic chamber with a relatively high cutoff frequency (approximately 1 kHz) for conducting free field impedance measurements. A special test chamber would also keep the high sound levels used for the free field tests from interfering with nearby activities. It is recommended that some effort be devoted to the design and development of a special test chamber for free field impedance measurements.

3.7 References

1. Allard, J. F. and Sieben, B., Measurements of Acoustic Impedacnce in a Free Field with Two microphones and a Spectrum Analyzer, *Journal of the Acoustical Society of America*, 77(4), 1617-1618, April, 1985.
2. Allard, J. F. and Champoux, Y., In Situ Two-Microphone Technique for the Measurement of the Acoustic Surface Impedance of Materials, *Noise Control Engineering Journal*, 32(1), 15-23, Jan-Feb, 1989.
3. Allard, J. F. and Lafarge, D., Free Field Measurement at High Frequencies of the Impedance of Porous Layer, *Second Int Congress on Recent Development In Air- and Structure-Borne Sound and Vibration*, Auburn University, 759-762, March 4-6, 1992.
4. ASTM, Standard Test for Impedance and Absorption of a Acoustical Materials Using a Tube, Two microphones, and a Digital Frequency Analysis system, *ASTM E1050-90*, 1-6, 1990.
5. Balan, C. and Hoff, G., Propulsion Simulator for High Bypass Turbofan Performance Evaluation, *SAE Aerospace Atlantic Conference & Exposition*, Dayton, Ohio, 1-10, April 20-23, 1993.
6. Balan, C. and Hoff, G.E., *Aerospace Engineering*, Turbofan Propulsion Simulator, 11-16, August, 1993.
7. Balan, C., Design Considerations of a Versatile Simulator for High Bypass Turbofans, Proceedings, *International Gas Turbine and Aeroengine Congress and Exposition*, Cincinnati, Ohio, May 24-27, 1993.
8. Bolton, J. S., Cepstral techniques in the measurement of acoustic reflection coefficient, with applications to the determination of acoustic properties of elastic porous materials, *Thesis submitted for the degree of Doctor of Philosophy*, University of Southampton, United Kingdom, July 1984.
9. Brouard, B., Lafarge, D., Allard, J. F. and Tamura, M., Measurement and Prediction of the Reflection Coefficient of Porous Layers at Oblique Incidence and for Inhomogeneous Waves, *Journal of the Acoustical Society of America*, 99(1), 100-107, January, 1996.
10. Brouard B., Allard, J. F., Lauriks, W. and Verhaegen, C., Acoustical Impedance and Absorption Coefficients of Porous Layers Covered by a Facing Perforated by Parallel Slits, *Noise Control Engineering Journal*, 41(1), 289-297, Jul-Aug, 1993.
11. Champoux, Y. and Esperance, L., Numerical Evaluation of Errors Associated with the Measurement of Acoustic Impedance in a Free Field Using Two Microphones and a Spectrum Analyzer, *Journal of the Acoustical Society of America*, 84(1), 30-38, July 1998.
12. Cramond, A. J. and Don, C. G., Reflection of Impulses as a Method of Determining Acoustic Impedance, *Journal of the Acoustical Society of America*, 75(2), 383-389, February, 1984.

13. Dahl, M. D. and Woodward, R. P., Comparison Between Design and Installed Acoustic Characteristics of NASA Lewis 9- by 15-Foot Low-Speed Wind Tunnel Acoustic Treatment, *NASA Technical Paper 2996*, April, 1990.

14. Dickinson, P. J. and Doak, P. E., Measurements of the Normal Acoustic Impedance of Ground Surfaces, *Journal of Sound and Vibration.*, 13(3), 309-322, 1970.

15. Fuller, C. R., Free-Field Correction Factor for Spherical Acoustic Waves Impinging on Cylinders, *AIAA Journal*, 27(12), 1722-1726, December, 1989.

16. Hartwig, T. J. and Bolton, J. S., Two-Microphone Measurements of the Acoustical Properties of SAE and ISO Pass by Surfaces in the Presence of Wind and Temperature Gradients, *SAE Transactions*, Travers City Michigan, 931-945, May, 1997.

17. Hodges, R. M., Gerhold, C., Balster, D. and Thomos R., Acoustic Testing of Very High Bypass Ratio Turbofans Using Turbine Powered Scale Models, *18th AIAA Aerospace Ground Testing Conference*, Colorado Springs, AIAA94-2552, June 20-23, 1994.

18. Ingard, U. and Bolt, R. H., A Free Field Method of Measuring the Absorption coefficient of Acoustic Materials, *Journal of the Acoustical Society of America*, 23(5), 509-516, September, 1951.

19. Ingard, U. and Bolt, R. H., Absorption Characteristics of Acoustic Material with Perforated Facings, *Journal of the Acoustical Society of America*, 23(5), 533-540, September, 1951.

20. Ingard, U., Perforated Facing and Sound Absorption, *Journal of the Acoustical Society of America*, 26(2), 151-154, March, 1954.

21. Jacobsen, F., Cutanda, V. and Juhl, P. M., A numerical and Experimental Investigation of the Performance of Sound Intensity Probes at High Frequencies, 25p, *Journal of the Acoustical Society of America*, February 21, 1997.

22. Jarvis, D. R. and Barham, R. G., Free-Field Sensitivity Calibration of Laboratory Standard Microphones by the Reciprocity Technique: *Measurements for the 1991 EEC Intercomparison*, 1-24, National Physical Laboratory, May 1993.

23. Jones, M. G. and Parrott, T. L., Evaluation of a Multi-point Method for Determining Acoustic Impedance, *Mechanical Systems and Signal Processing*, 3(1), 15-35, 1989.

24. Jones, M. G. and Stiede, P. E., Comparison of Methods for Determining Specific Acoustic Impedance, *Journal of the Acoustical Society of America*, 101(5), 2694-2704, May, 1997.

25. Kinsler, L. E., Frey, A. R., Coopens, A. B. and Senders, J. V., *Fundamentals of Acoustics*, John Wiley & Sons, New York.

26. Klein, C. and Cops, A., Angle of Dependence of the Impedance of a Porous Layer, *Acustica*, 44, 258-264, 1980.

27. Li, J. F., Hodgson, M. and Pascal, J. C., Errors Caused by the Finite-Difference Approximation in the Estimation of the Surface Impedances of Materials, Proceedings, *Noise-Con 96*, Seattle, Washington, 723-728, September 29-October 2, 1996.

28. Musafir, R. E., Slama, J. G. and Zinkdeluk, M., Use of Acoustic Intensity Measurements In the Characterization of Jet Noise Sources, *2nd International Congress on Acoustic Intensity*, CETIM, Sinlis, France, 407-412, September 23-26, 1985.

29. Nobile, M. A., Measurement of the Spherical Wave Absorption Coefficient at Oblique Incidence Using the Two-Microphone Transfer Function Method, *Inter-noise*, December 4-6, 1989.

30. Nobile, M. A. and Hayek, S. I., Acoustic Propagation over an Impedance Plane, *Journal of the Acoustical Society of America*, 78(4), 1325-1335, October, 1985.

31. Parrott, T. L. and Jones, M. G., Parallel-element Liner Impedance for Improved Absorption of Broadband Sound in Ducts, *Noise Control Engineering Journal*, 43(6), 183-195, Nov-Dec, 1995.

32. Rogers, C. L. and Watson, R. B., Determination of Sound Absorption Coefficients Using a Pulse Technique, *Journal of the Acoustical Society of America*, 32(12), 1555-1557, Dec, 1960.

33. Salikuddin, M. and Ahuja, K. K., A Device To Generate high Frequency Noise From Commercially Available Low Frequency Acoustic Drivers, *Journal of Sound and Vibration*, 123(2), 261-280, 1988.

34. Seybert, A. F. and Ross, D. F., Experimental Determination of Acoustic Properties Using a Two-Microphone Random Excitation Technique, *Journal of the Acoustical Society of America*, 61(5), 1362-1370, May 1977.

35. Tizianel, J., Allard, J. F., Lauriks, W. and Kelders, L., Experimental Localization of a Pole of Reflection Coefficient of a Porous Layer, *Journal of Sound and Vibration*, 202(4), 600-606, 1997.

36. The Measurement of Acoustic Impedance at Oblique Incidence with Two-Microphones, *Journal of Sound and Vibration*, 101(1), 130-132, 1985.

37. Watson, W. R. and Jones, M. G., Validation of a Numerical Method for Extracting Linear Impedance, *AIAA Journal*, 34(3), 548-554, March, 1996.

38. Wu, M. Q., Micro-perforated Panels for Duct Silencing, *Noise Control Engineering Journal*, 45(2), 69-77, Mar-Apr, 1997.

39. Wuzhou, Y. and Zuomin, W., Three-point Method for Measurement In an Impedance Tube Using Pseudorandom Signal Excitation, *Acta Acustica*, 21(4), 352-361, July, 1996.

4. Evaluation of In-Situ Methods for Measurement of Acoustic Impedance

4.1 The "In-Situ" Method For The Measurement Of Acoustic Impedance

The "In-Situ" technique is designed to measure the acoustic impedance of locally reacting, single-degree-of-freedom (SDOF), resonator type, acoustic liners. This technique has been used, with some success, to measure the effects of grazing flow on the acoustic impedance of SDOF liners with perforated face sheets [1, 2]. The work presented in this report was undertaken to evaluate the feasibility of this method for measuring acoustic impedance of scaled acoustic treatment at high frequencies.

The sketch in Figure 4-1 below shows a single cavity of a locally reacting, single layer (SDOF), acoustic liner of the type used in the inlet and exhaust ducts of an aircraft engine. It consists of a porous face sheet bonded to a cavity. The cavity is normally constructed from a thin walled honeycomb bonded to an acoustically hard back wall. The width (or diameter) of the cavity cross section is considered to be small compared to the acoustic wave length over the frequency range of interest. Moreover, the walls of the cavity are assumed to be acoustically hard so that there is no acoustic transmission between adjacent cavities.

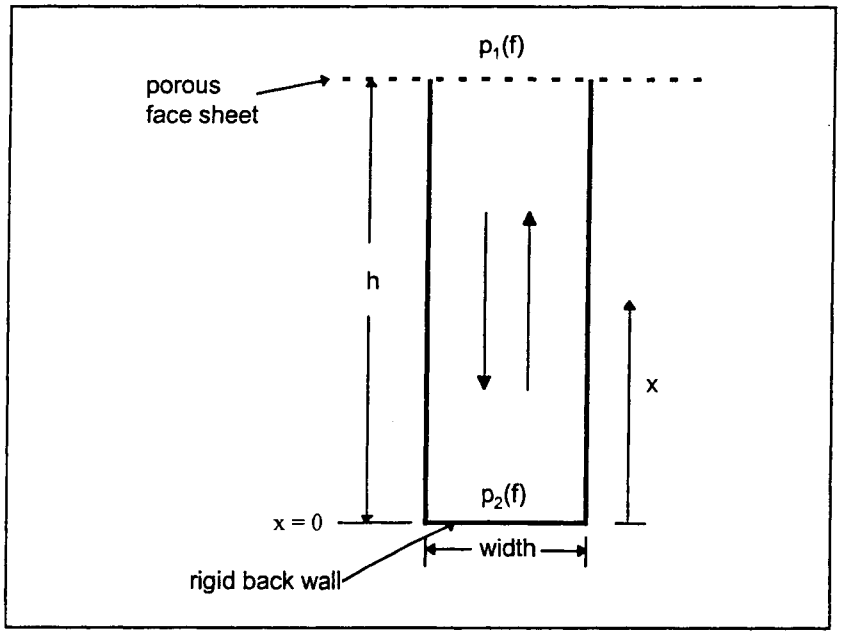

Figure 4-1. Isolated, locally-reacting SDOF resonator cavity.

We define

$p_1(f)$ - acoustic pressure at the surface of the liner face sheet – assumed constant over the area of the cavity.

$p_2(f)$ - acoustic pressure at the bottom or back wall of cavity (x=0) -- assumed constant over the area of the cavity.

f - acoustic frequency

h - depth of the cavity

c - speed of sound in the air contained in the cavity

k - acoustic wave number; $k = 2\pi f/c$

The complex ratio of the acoustic pressures measured at the face sheet and at the back wall respectively. is

$$H(f)e^{i\phi(f)} = \frac{p_1(f)}{p_2(f)} \tag{4-1}$$

If the walls of the cavity are rigid, then sound can enter and leave the cavity through the face sheet only. If the width of the cavity is such that over the frequency range of interest, only plane wave mode can propagate inside it, then the single-degree-of-freedom (SDOF) liner can be modeled by one-dimensional wave propagation theory. It can be shown that the acoustic impedance, Z(f), at the surface of the face sheet is given by

$$Z(f) = R(f) + iX(f) = -iH(f)\frac{e^{i\phi(f)}}{\sin(kh)} = H(f)\left\{\frac{\sin[\phi(f)]}{\sin(kh)} - i\frac{\cos[\phi(f)]}{\sin(kh)}\right\} \tag{4-2}$$

Thus, in terms of the specific acoustic resistance, R(f), and reactance, X(f), we can write

$$R(f) = H(f)\frac{\sin[\phi(f)]}{\sin(kh)} \tag{4-3}$$

$$X(f) = -H(f)\frac{\cos[\phi(f)]}{\sin(kh)} \tag{4-4}$$

Thus, to measure the acoustic impedance by the "In-Situ" method, we need to measure, simultaneously, the acoustic pressure fluctuations at the face sheet and at the back wall. The acoustic transducers have to be sufficiently small that they do not affect the measured acoustic signals. The Transducers must be calibrated for their relative amplitude and phase response characteristics to ensure accurate measurements of the acoustic impedance data.

4.2 Analysis of Possible Errors in the In-Situ Impedance Measurement Technique.

Notice that there are three principal quantities that can affect the accuracy of the measured resistance, R(f), and reactance, X(f). These are H(f) , ϕ(f) and (kh). An error in any one of these quantities can produce an error in the measured values of the acoustic resistance and reactance. The effects of errors in these principal quantities are discussed below.

4.2.1 Errors in "kh"

It can be shown that

$$\frac{\delta R(f)}{R(f)} = \frac{\delta X(f)}{X(f)} = -\cot(kh)\cdot\delta(kh) \tag{4-5}$$

There are two possible sources of error in the quantity kh.

- An error in the cavity depth, h, can be due to an uncertainty in the measurement of h.
- An error in the speed of sound, c, can cause an error in the value of k.

Now

$$\delta(kh) = kh\left(\frac{\delta h}{h} - \frac{\delta c}{c}\right) \tag{4-6}$$

$$\frac{\delta c}{c} = \frac{0.5}{\sqrt{\frac{\delta T}{T}}} \tag{4-7}$$

therefore

$$\delta(kh) = kh\left(\frac{\delta h}{h} - \frac{0.5}{\sqrt{\frac{\delta T}{T}}}\right) \tag{4-8}$$

With thermocouples, temperature can be measured with an accuracy of ±2°R. Based on this, $\delta c/c \approx \pm 0.0019$, which represents less than 0.2% change in the speed of sound. The estimated "percent error" in measured impedance due to a ±2°R error in the measured temperature is illustrated in Figure 4-2. Note that the error in the measured resistance and reactance is magnified near the anti-resonance frequencies (multiples of half wave length, $\lambda/2$). Since the reactance of typical liners has a large magnitude at anti-resonance frequencies, this measurement error is insignificant. On the other hand, this error represents a significant deviation for the resistance.

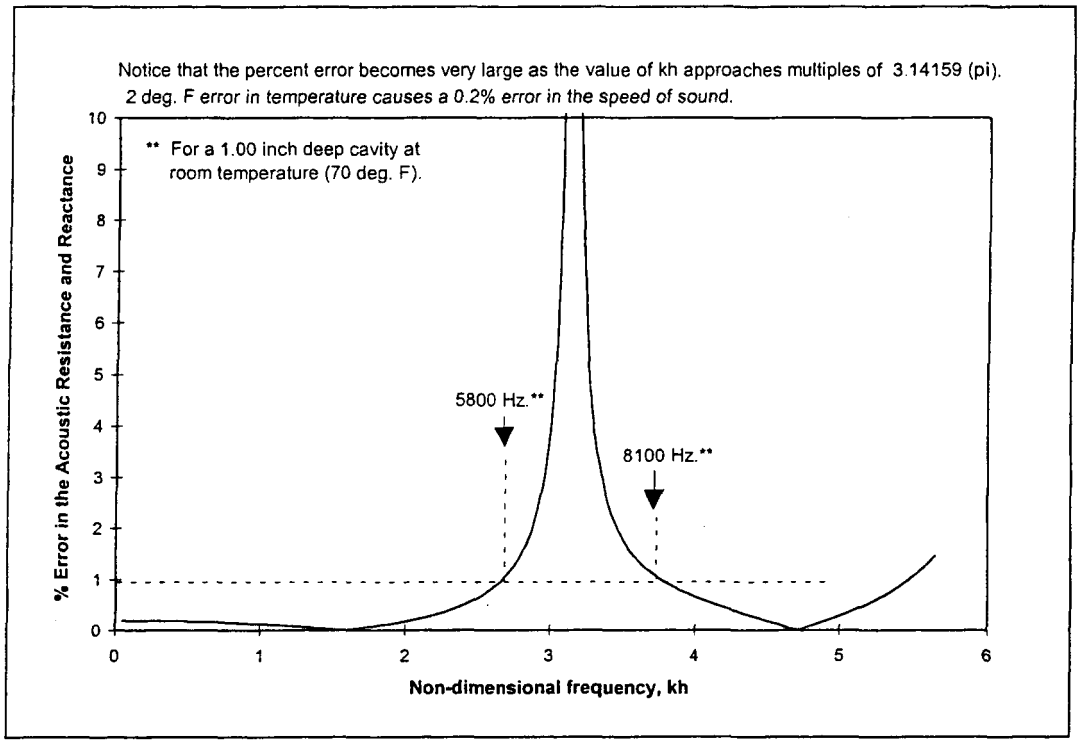

Figure 4-2. Percent error in the acoustic impedance of a liner due to an error in the measured temperature of 2 degrees R.

4.2.2 An error δH(f) in the magnitude, H(f) .

It can be shown that the errors δR(f) and δX(f), due to an error δH(f) in H(f), are given by

$$\delta R(f) = \frac{\sin[\phi(f)]}{\sin(kh)}\delta H(f) \tag{4-9}$$

and

$$\delta X(f) = -\frac{\cos[\phi(f)]}{\sin(kh)}\delta H(f) \tag{4-10}$$

Therefore

$$\frac{\delta R(f)}{R(f)} = \frac{\delta X(f)}{X(f)} = \frac{\delta H(f)}{H(f)} \tag{4-11}$$

Thus, a ±1% error in the measured value of H(f) will result in ±1% error in the corresponding values of R(f) and X(f) at all frequencies.

4.2.3 An error $\delta\phi(f)$ in the phase, $\phi(f)$

The error in resistance caused by an error in the phase is

$$\delta R(f) = \frac{\cos[\phi(f)]}{\sin(kh)} H(f)\delta\phi(f) \tag{4-12}$$

The relative error in resistance is then

$$\frac{\delta R(f)}{R(f)} = \frac{\cos[\phi(f)]}{\sin[\phi(f)]}\delta\phi(f) = \cot[\phi(f)]\delta\phi(f) \tag{4-13}$$

The error in reactance caused by an error in phase is

$$\delta X(f) = \frac{\sin[\phi(f)]}{\sin(kh)} H(f)\delta\phi(f) \tag{4-14}$$

giving a relative phase error

$$\frac{\delta X(f)}{X(f)} = -\frac{\sin[\phi(f)]}{\cos[\phi(f)]}\delta\phi(f) = -\tan[\phi(f)]\delta\phi(f) \tag{4-15}$$

Notice that the percent errors in the values of resistance and reactance are functions of frequency.

4.2.4 Some Error Computations for the In-Situ Impedance Measurement Method.

To illustrate the magnitude of measurement errors, the impedance of a typical SDOF liner with a linear face sheet is assumed to be given by

Resistance: $R(f) = 1.0$

Reactance: $X(f) = 0.4 - \cot(kh)$

Using Equation (4-2), we can compute the magnitude H(f) and phase $\phi(f)$ of the complex ratio (Transfer Function) of the acoustic pressures $p_1(f)$ and $p_2(f)$, at the face sheet and the back wall respectively. Thus, in terms of R(f) and X(f) , the transfer function magnitude and phase is given by

$$H(f) = \sin(kh)\sqrt{R(f)^2 + X(f)^2} \tag{4-16}$$

$$\phi(f) = \tan^{-1}\left(-\frac{R(f)}{X(f)}\right) \tag{4-17}$$

An example of the spectrum of such a transfer function, for a 1.27 cm.(0.5 inch) deep SDOF liner is shown in Figures 4-3 and 4-4. These data represent what would be measured, without any errors, under ideal conditions. Similar data can be obtained for any other cavity depth value. Note that a $\pm 1°$ in phase can not be detected on the plot of Figure 4-4. Figure 4-5 shows the effect of an error of $\pm 1°$ (± 0.0174 radians) in the phase data of Figure 4-4 on the acoustic resistance values that would be computed. Figures 4-6 and 4-7 show similar results for

2.54 cm. (1.0 inch) and 3.81 cm. (1.5 inch) deep SDOF liners. The effect of an error in the phase, $\phi(f)$, on the acoustic reactance is found to be much less in magnitude. This is illustrated in Figure 4-8. These results show clearly that the acoustic resistance values of a SDOF liner, measured by the in-situ method, will have bigger measurement uncertainties than the corresponding acoustic reactance values.

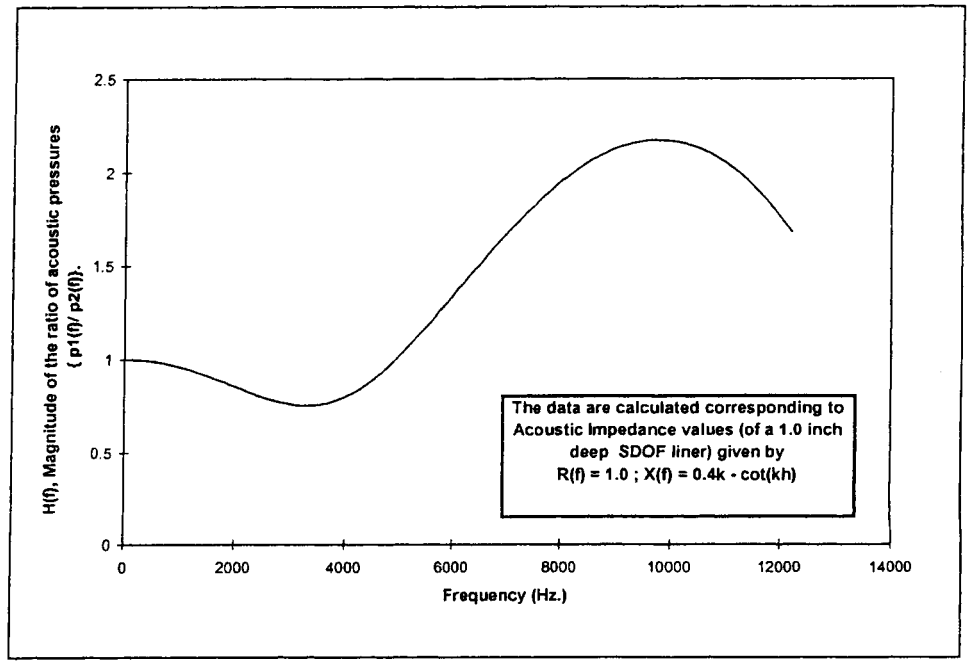

Figure 4-3 Transfer function H(f), magnitude of the ratio of acoustic pressure oscillations at the face sheet and back wall for a 0.5 in. deep SDOF liner.

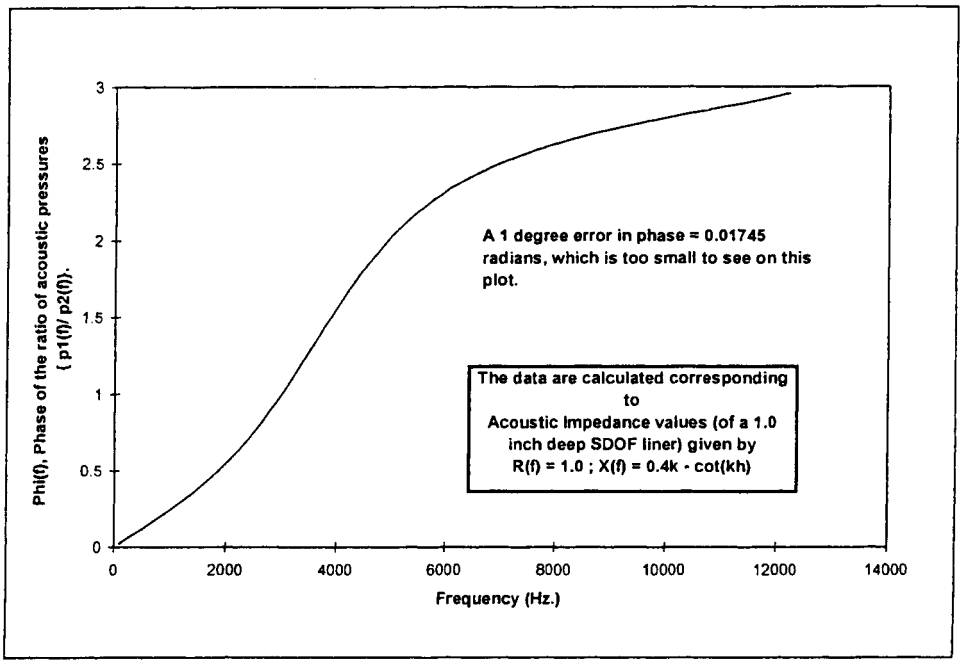

Figure 4-4. Transfer function phase, φ (f), phase of the ratio of acoustic pressure oscillations at the face sheet and the back wall for a 1.27 cm (0.5 in.) deep SDOF liner.

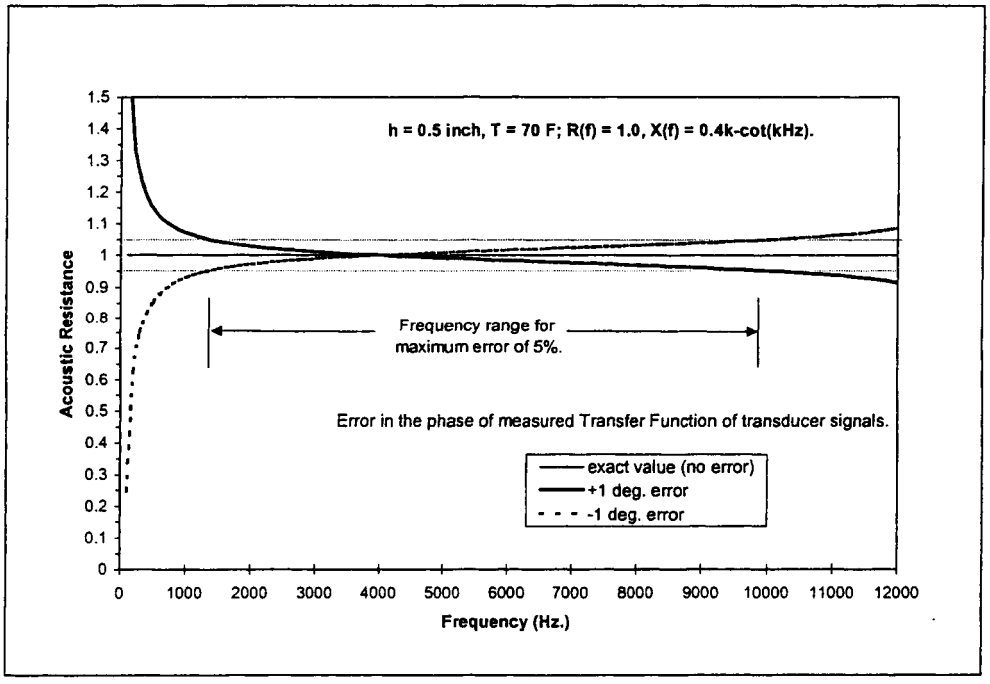

Figure 4-5. The effect on resistance of 1 degree error in the measured phase of the transfer function for 1.27 cm. (0.5 in.) deep liner.

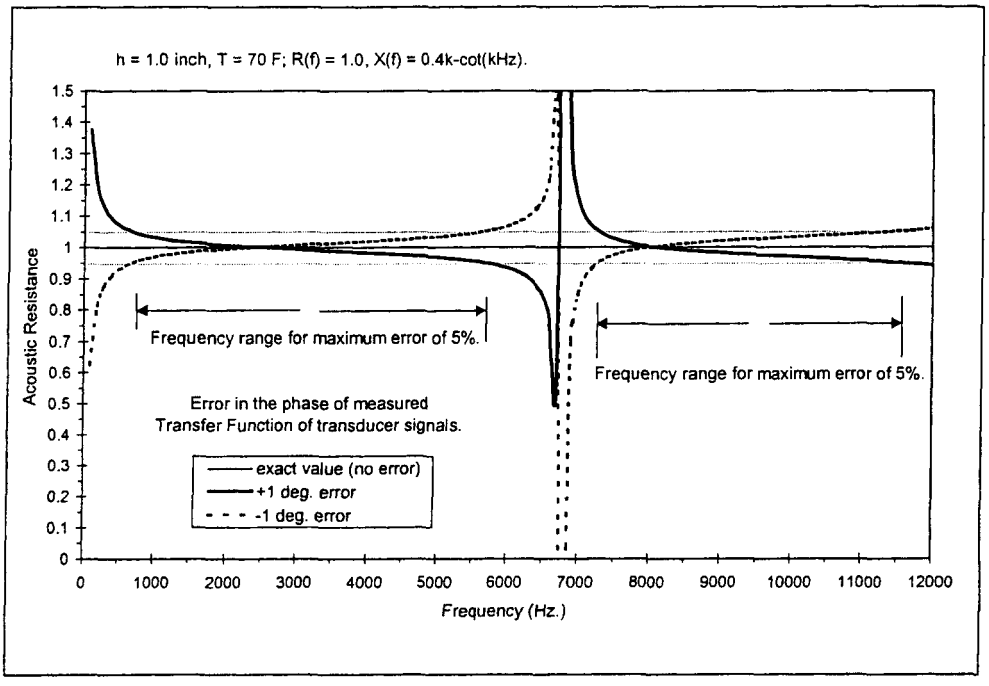

Figure 4-6. The effect on resistance of 1 degree error in the measured phase of the transfer function for 2.54 cm. (1.0 in.) deep liner.

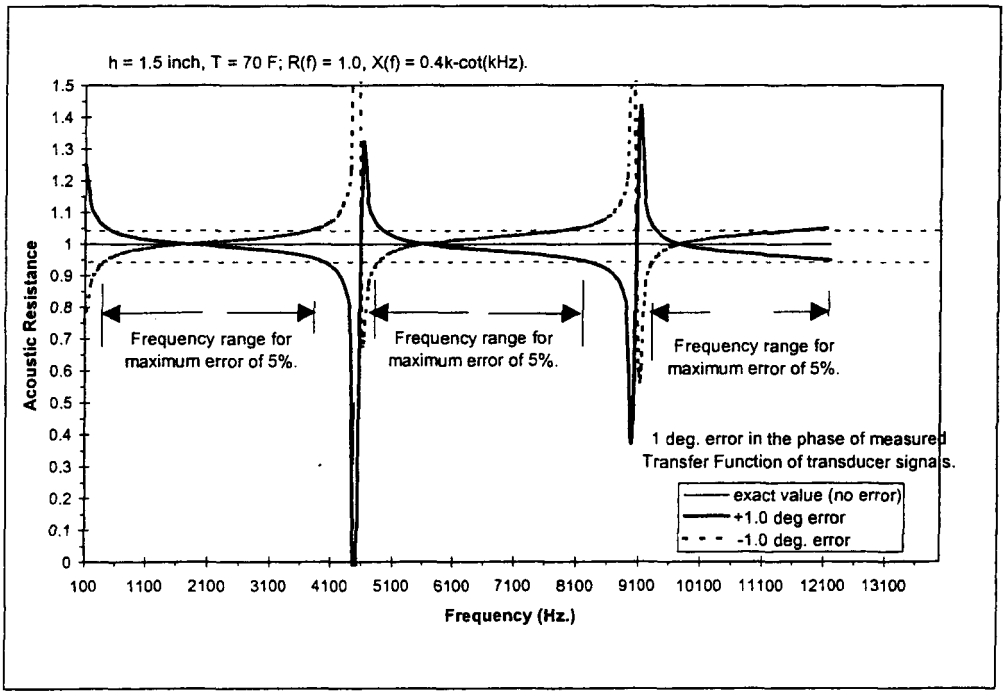

Figure 4-7. The effect on resistance of 1 degree error in the measured phase of the transfer function, 3.81 cm. (1.5 in.) deep liner.

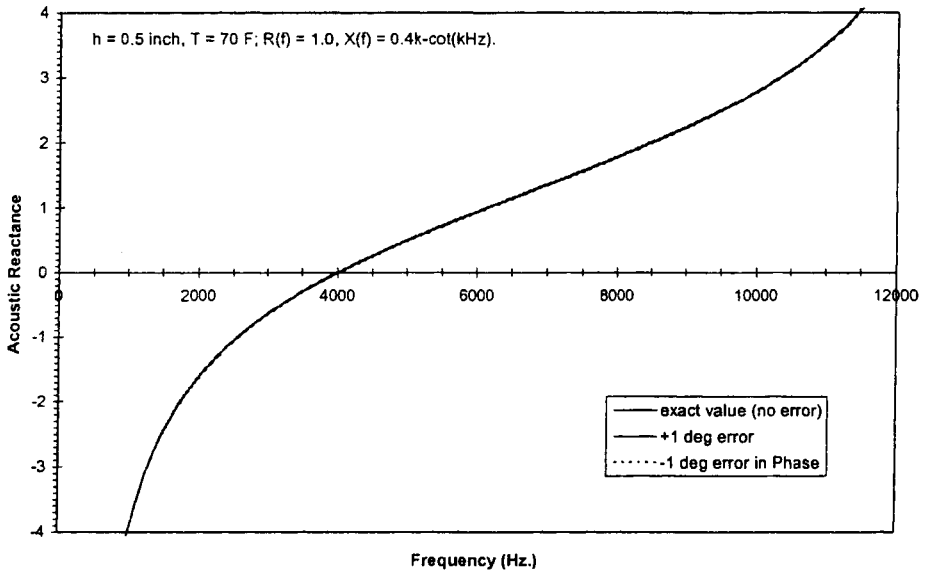

Figure 4-8. The effect on reactance of 1 degree error in the measured phase of the transfer function for 1.27 cm. (0.5 in.) deep liner.

4.2.5 Possible Causes Of Measurement Errors

Some possible causes of measurement errors that have been identified are:

1. Test set-up may not satisfy assumptions of rigid cavity walls and one-dimensional (plane wave) acoustic propagation in the cavity. The acoustic pressure, $p_1(f)$, measured at a fixed location on the face sheet, may not be representative of the value averaged over the face sheet area.
2. In an in-situ impedance measurement test, the depth of the cavity, h, is measured. Consequently there can be some error in the value of h. Current estimate of error in the measured value of h is ±0.0254 cm. (±0.010 inch).
3. The speed of sound is computed from a measured value of the temperature, which can be measured within an accuracy of ± 2°F.
4. The magnitude, H(f), and phase, $\phi(f)$, are obtained from the analysis of signals from the acoustic pressure transducers installed at the face sheet surface and at the back wall. The errors in these measured data can be due to the following:
    - distortion of signals by the signal conditioning electronics due to incorrect gain settings
    - lack of accurate calibration of transducer systems
        - poor stability of electronics used in data acquisition and analysis (transducers, signal conditioning amplifiers, A-to-D converter in the signal analyzer, etc.)

- installation effects (transducer response may be sensitive to any bending stress caused by insertion in a tube).
- effects of flow conditions (Steady ΔP may affect the response characteristics of the transducers. If so, then the calibrations will not be applicable.)

4.3 Preliminary Experiments

The experiments were carried out in two phases. In the first phase, tests were designed to measure the impedance of a cavity only (no face sheet). In the second phase, limited tests were done with porous face sheets. All experiments were conducted without any grazing flow.

4.3.1 Impedance Measurements in Cavities of Rectangular Cross Section.

The apparatus used in these experiments is schematically illustrated in Figure 4-9 below. It consists of rectangular tubes, made of brass, that are bonded together to form a rectangular cell core structure. The outside dimensions of the brass tube are 1.041 cm x 0.787 cm. (0.410 in. x 0.310 in.). The tubes have 0.028 cm. (0.011 in.) thick walls. Thus the thickness of the wall between adjacent cavities is 0.056 cm. (0.022 in.). In this sketch, these tubes are mounted on a suitably machined metal block.

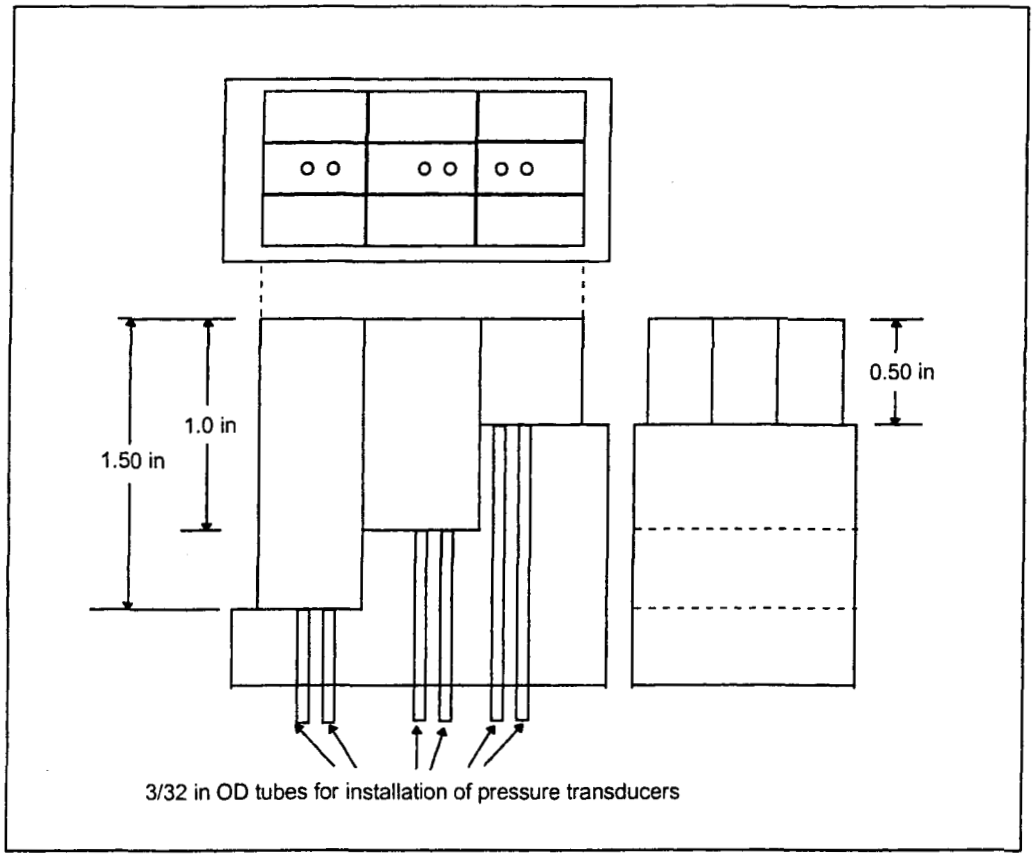

Figure 4-9. Impedance sample holder for two-microphone in-situ impedance measurement.

Note that each of the three central cells has a pair of tubes for acoustic transducers. One of the tubes in a pair must be located at the center of the cell.

The above rectangular cavity core apparatus was flush mounted in a flat Plexiglas plate and instrumented to measure the impedance of the three cavities, one after the other. This set up is illustrated in Figure 4-10.

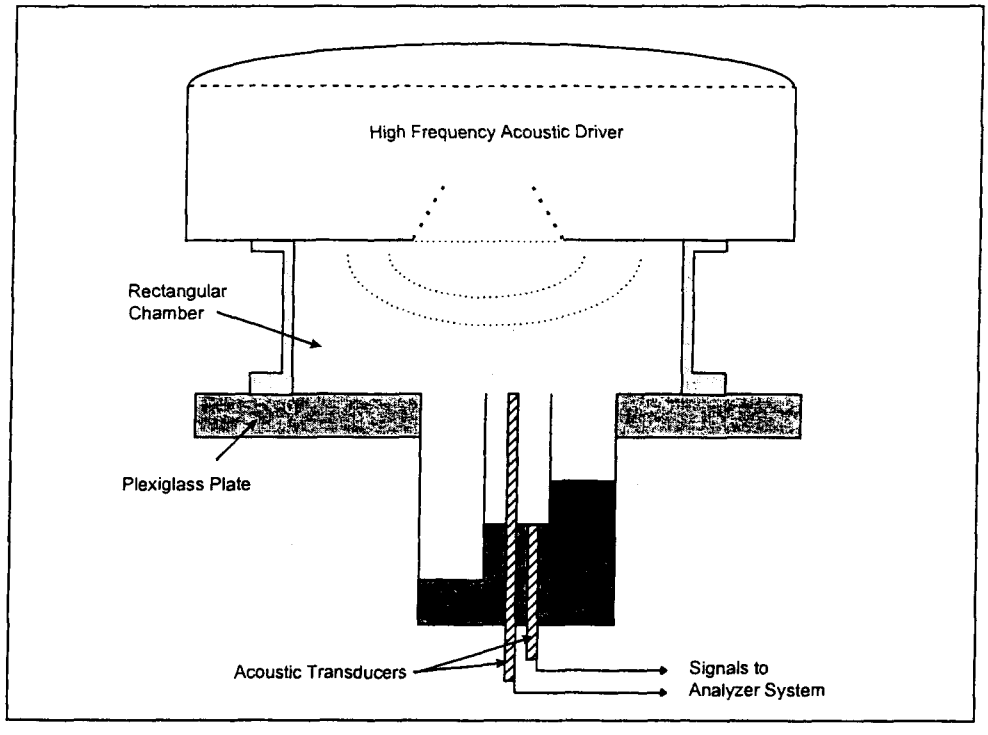

Figure 4-10. Test apparatus used for two-microphone in-situ impedance measurement

Note that the acoustic field in the rectangular chamber consists of many modes. Therefore, the acoustic field over the Plexiglas plate surface may vary, particularly at the higher frequencies. This means that there is the possibility of acoustic transmission across the cavity wall, if the walls are not sufficiently stiff. Such transmission is not permitted in the in-situ method for impedance measurement.

Figures 4-11, 4-12, and 4-13 compare the acoustic impedance data, measured in rectangular cavities, with predicted data. With the 1.27 cm. (0.5 inch) deep cavity, measurements above 8 kHz., show significant measurement uncertainty. Results from the 2.54 cm. (1.0 inch) deep cavity (Figure 4-12), show significant measurement errors between 5kHz., and 7kHz., but improved accuracy between 7 kHz and 10 kHz. Data obtained with the 3.81 cm. (1.5 inch) deep cavity (Figure 4-13), does not show any significant improvement at the high frequencies (10 to 12 kHz.).

Generally good correlation between theory and experiment confirms that cavity walls are sufficiently rigid and the acoustic field inside the cavities can be modeled by one-dimensional wave propagation theory.

The deterioration in the measurement accuracy above 8 kHz may be due, in part, to poor signal to noise ratio. This conclusion may be drawn from the spectral data in Figure 4-14.

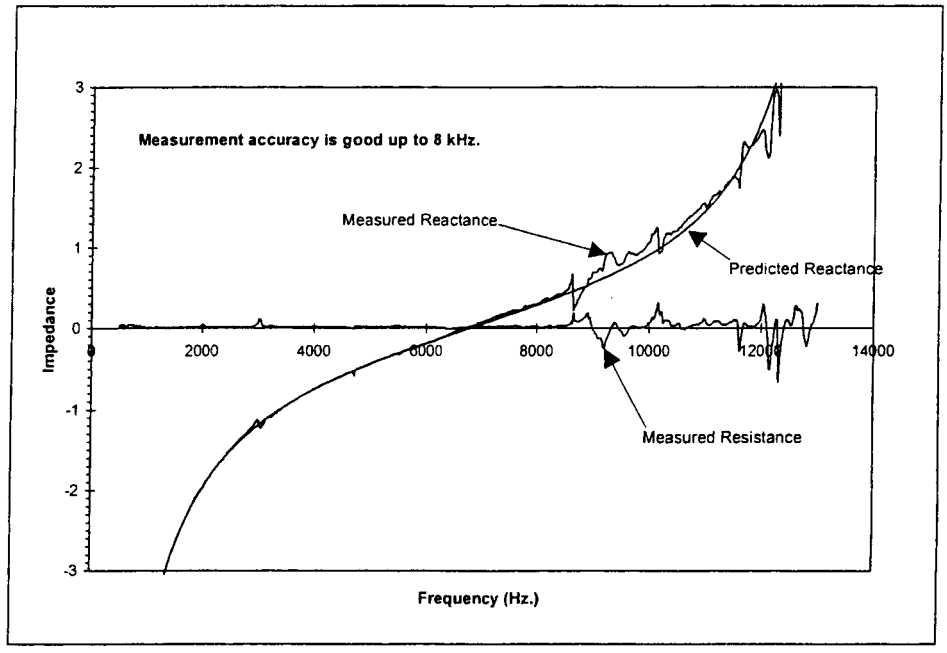

Figure 4-11. Comparison of in-situ measured impedance with predicted values for 1.27 cm. (0.5 inch) deep cavity with no faceplate.

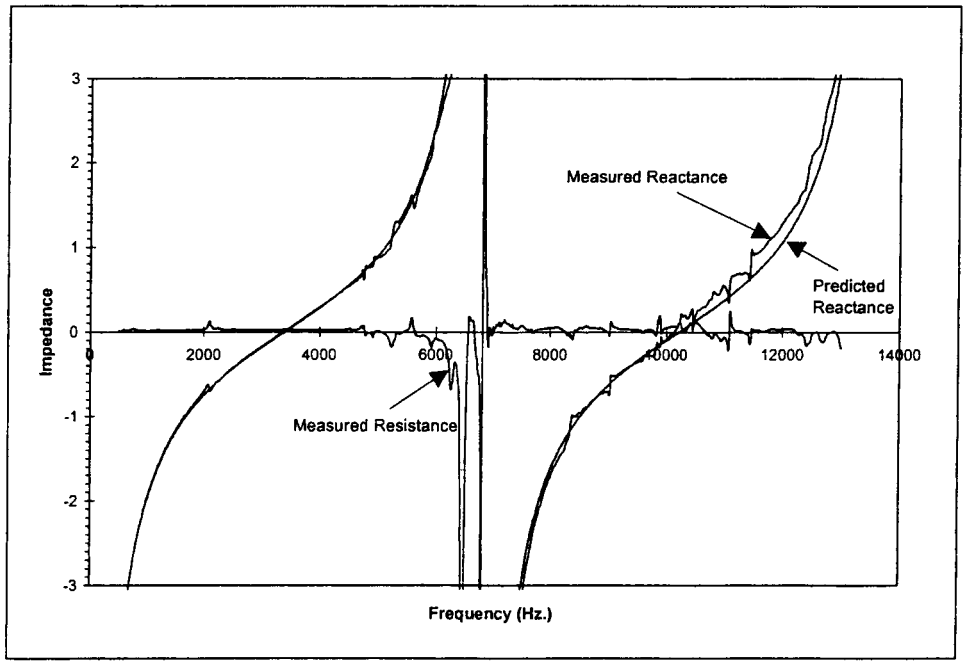

Figure 4-12. Comparison of in-situ measured impedance with predicted values for 2.535 cm. (0.998 in.) deep cavity with no faceplate.

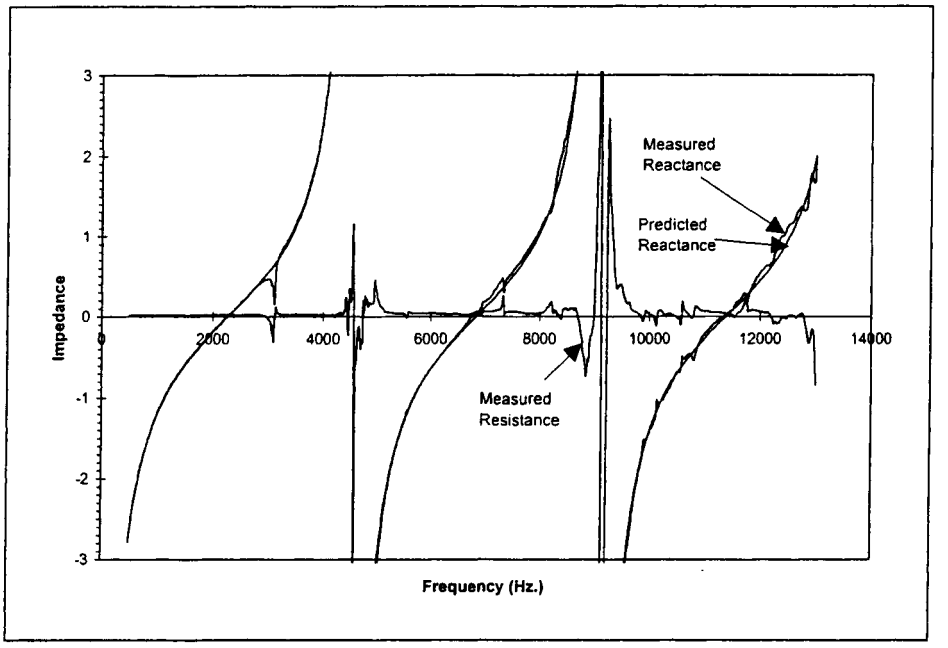

Figure 4-13. Comparison of in-situ measured impedance with predicted values for 3.792 cm. (1.493 in.) deep cavity with no faceplate.

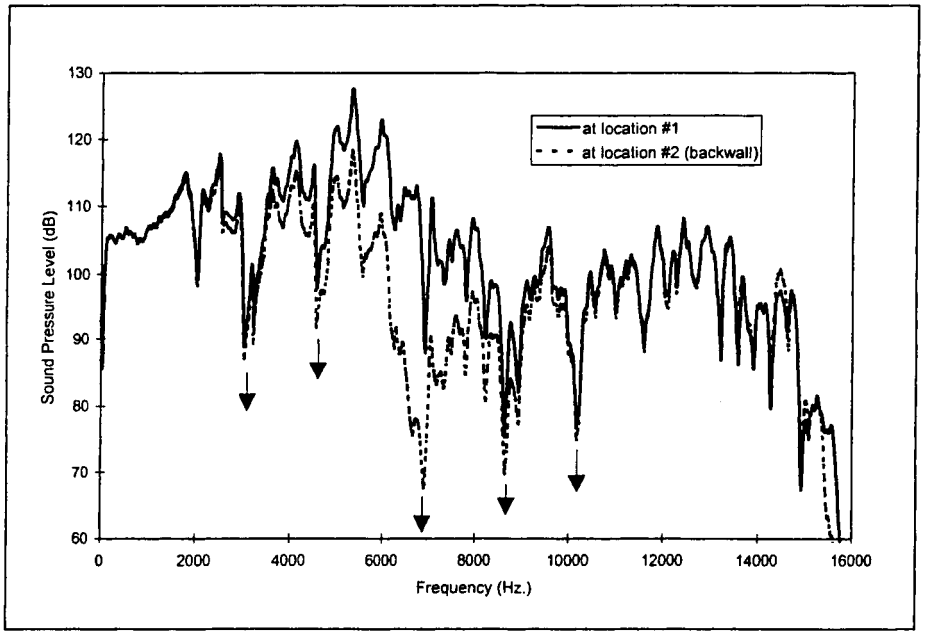

Figure 4-14. Auto-spectrum of the face sheet acoustic pressure.

4.3.2 Impedance Measurements in a Cavity of Circular Cross Section.

In these measurements the cavity was created in a brass tube of thick walls, as shown in Figure 4-15. The back wall transducer was flush-mounted in a piston, which was moved up or down the brass tube to set the cavity depth to any desired value.

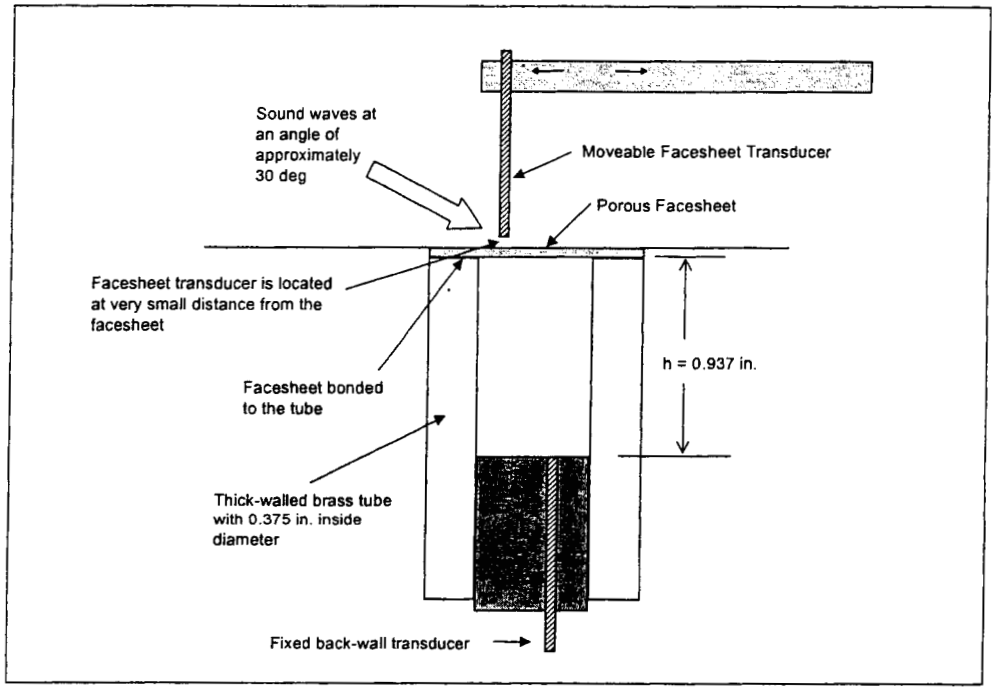

Figure 4-15. Schematic diagram of the setup for in-situ impedance experiments designed to study the effects of changing the location of the facesheet transducer.

First measurements were done, without a face sheet, for different values of the cavity depth. An example of such a measurement is illustrated in Figure 4-16. The correlation between measured and predicted data was found to be as good as for the rectangular cavities. After these measurements, tests were conducted with porous face sheets, as described below.

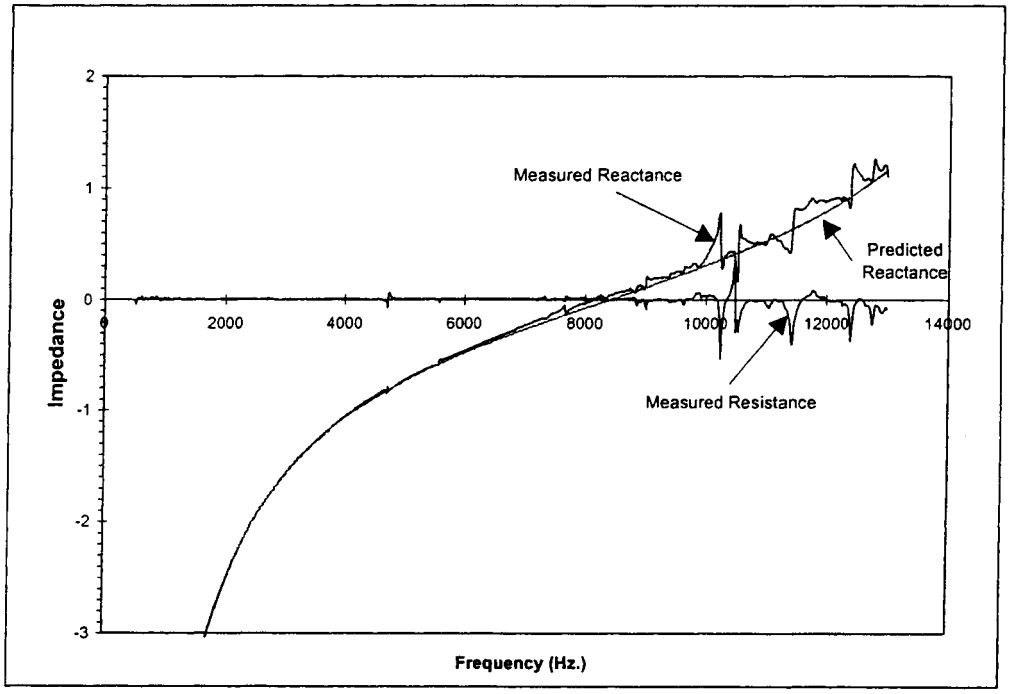

Figure 4-16. Comparison of impedance measurements and predictions for a 0.4 in. deep thick-walled cavity of circular cross-section.

A perforated sheet of 4.8% nominal porosity was bonded on the cavity to create a single-degree-of-freedom liner sample. The hole pattern of the perforated sheet relative to the cavity wall is shown in Figure 4-17. Note that the center hole in the pattern was drilled to accommodate the flush mounted face sheet transducer, as shown in Figure 4-15. The measured Impedance data are presented in Figure 4-18. Note that above 8kHz., the quality and accuracy of the measured impedance data become unsatisfactory.

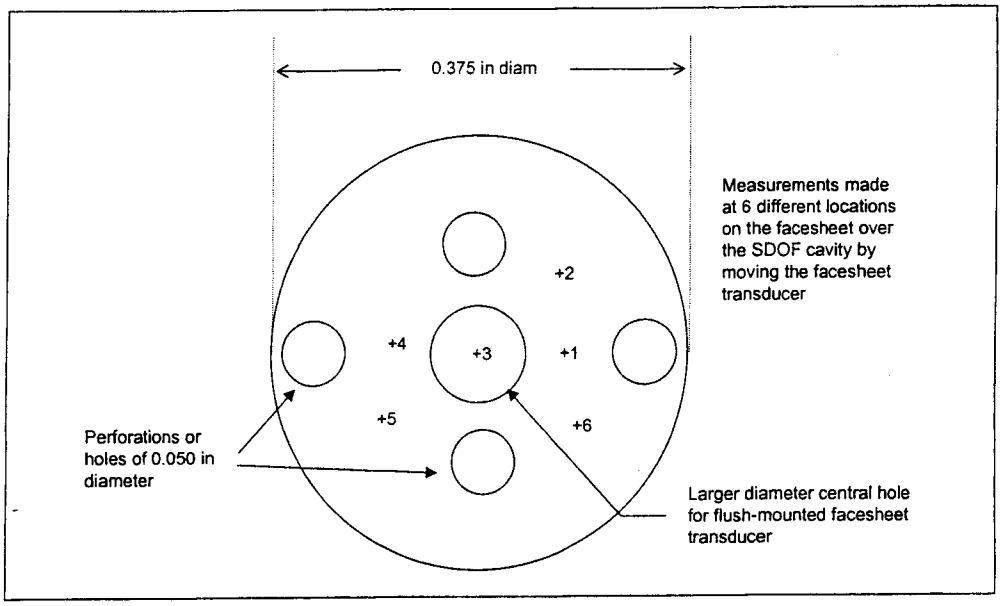

Figure 4-17. Diagram showing location of the facesheet transducer relative to the hole pattern of the facesheet for moving facesheet transducer measurement.

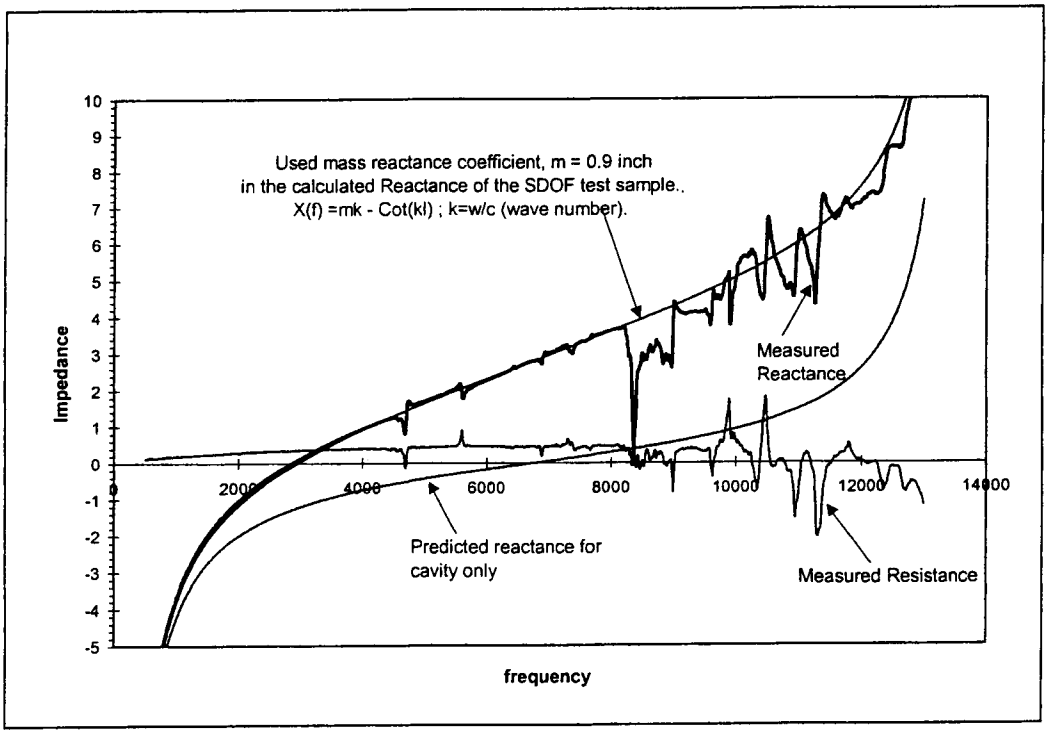

Figure 4-18. In-situ impedance measurement from a SDOF test sample with 1.27 cm. (0.5 in.) deep circular cavity with 4.8% porosity perforated facesheet.

Next, the sensitivity of the in-situ measurement to location of the face sheet transducer was investigated. The location of the face sheet transducer was controlled as shown in Figure 4-15. First impedance data were measured at locations shown in Figure 4-17. These data are plotted in Figures 4-19 and 4-20. The resistance data (Figure 4-19) show considerable data scatter with increasing frequency. However, the averaged values, based on the 6 locations, look reasonable. There is much less scatter in the Reactance data (Figure 4-20).

This suggests that at higher frequencies, there is some variation of the acoustic pressure over the face sheet. Therefore, a single location measurement of the acoustic pressure at the face sheet is not accurate enough. For accurate measurement of acoustic impedance, an estimate of the acoustic pressure, averaged over the face sheet area, is required.

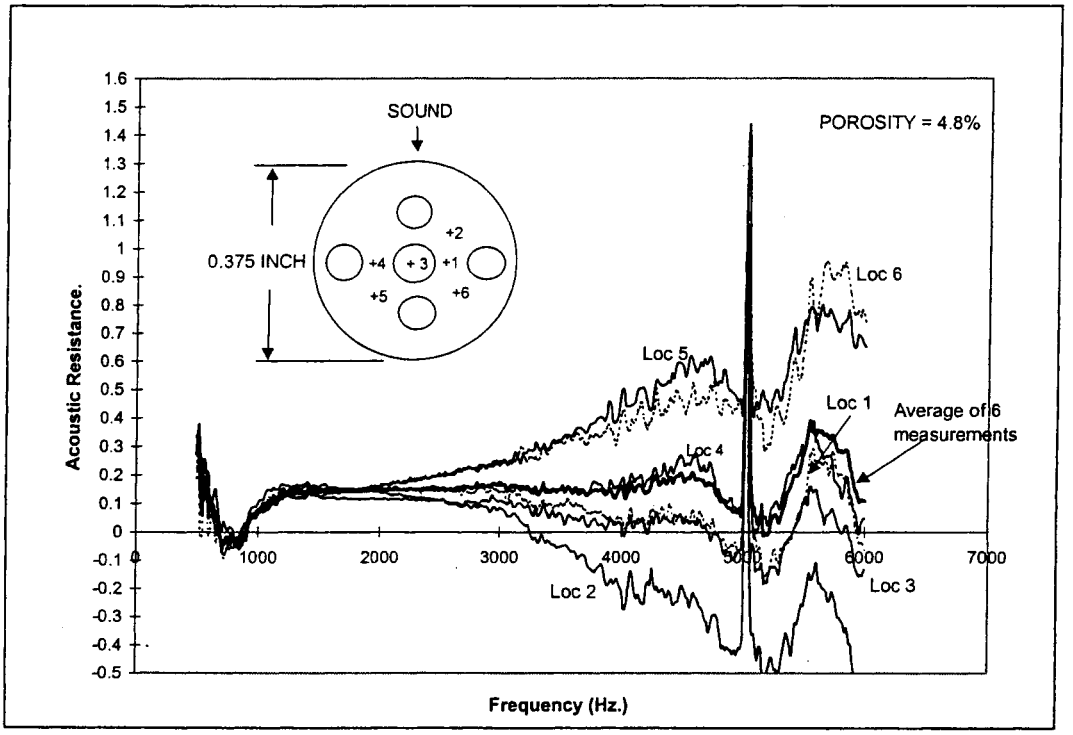

Figure 4-19. In-situ resistance measurement showing effects of changing the location of the face sheet transducer.

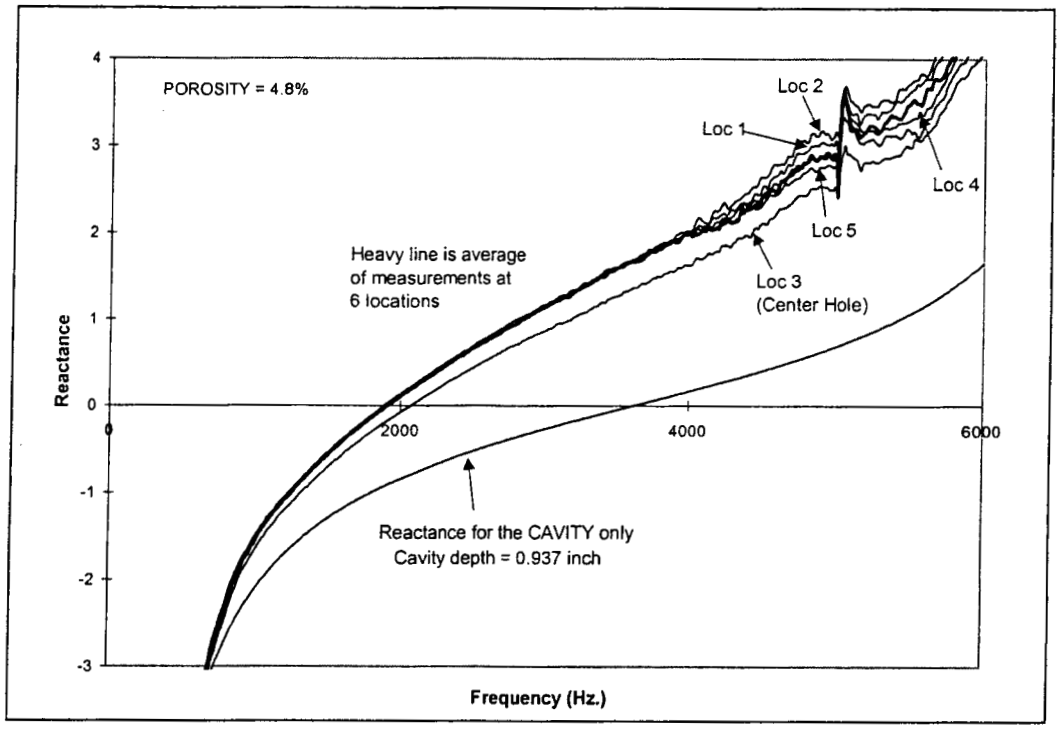

Figure 4-20. In-situ reactance measurement showing effects of changing the location of the facesheet transducer (see Figure 4-17 for transducer locations).

In the experiment discussed in the above paragraph, it was realized that acoustic pressure variation along the direction of sound propagation might be larger than along a diametral line at right angles to it. The data plotted in Figures 4-21 and 4-22 were measured along such a diametral line. As expected, these plots show much less scatter than those of Figures 4-19 and 4-20. From these observations, it would appear that the best location for face sheet acoustic pressure is at the center of the cavity.

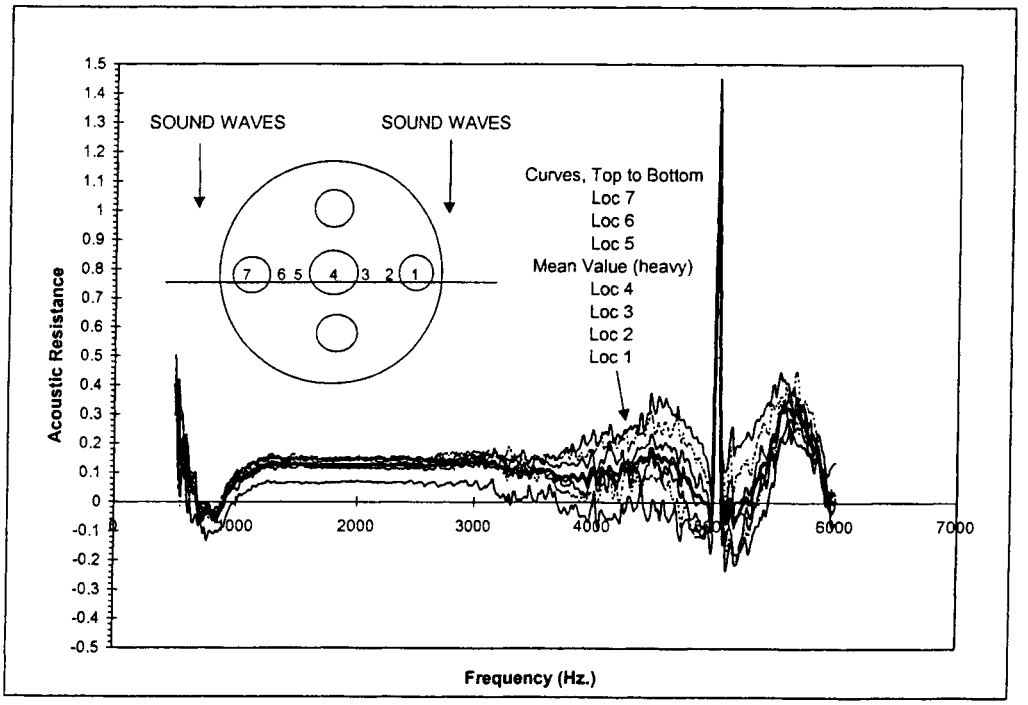

Figure 4-21. In-situ resistance measurement showing effects of changing location of the facesheet transducer.

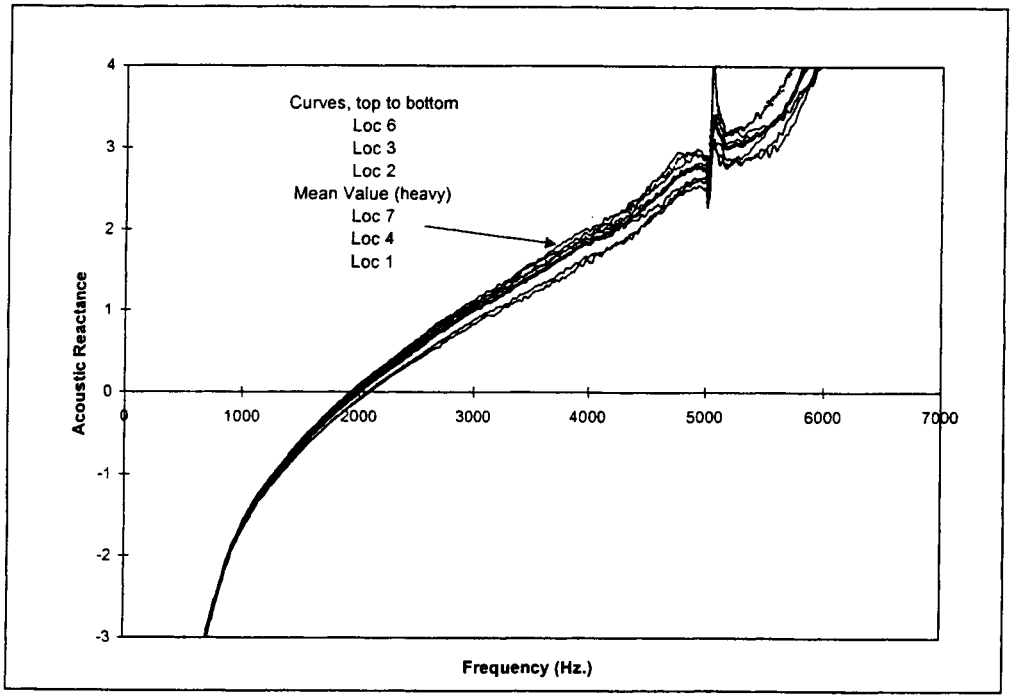

Figure 4-22. In-situ reactance measurement showing effects of changing the location of the facesheet transducer (see Figure 4-21 for transducer locations).

The next series of experiments were designed to study the effect of changing the location of the back wall transducer. For these, the face sheet transducer was installed in the center, as shown in Figure 4-23, while the location of the back wall transducer was varied. During these experiments, the orientation of the face sheet hole pattern relative to the acoustic source was kept unchanged. The measured impedance data are plotted in Figure 4-24. These plots have very little data scatter due to changing the back wall transducer. This shows that the measurement is not sensitive to the location of the back wall transducer. This is because only plane waves reach the back wall. Higher order modes are heavily damped due to the cut-off phenomenon.

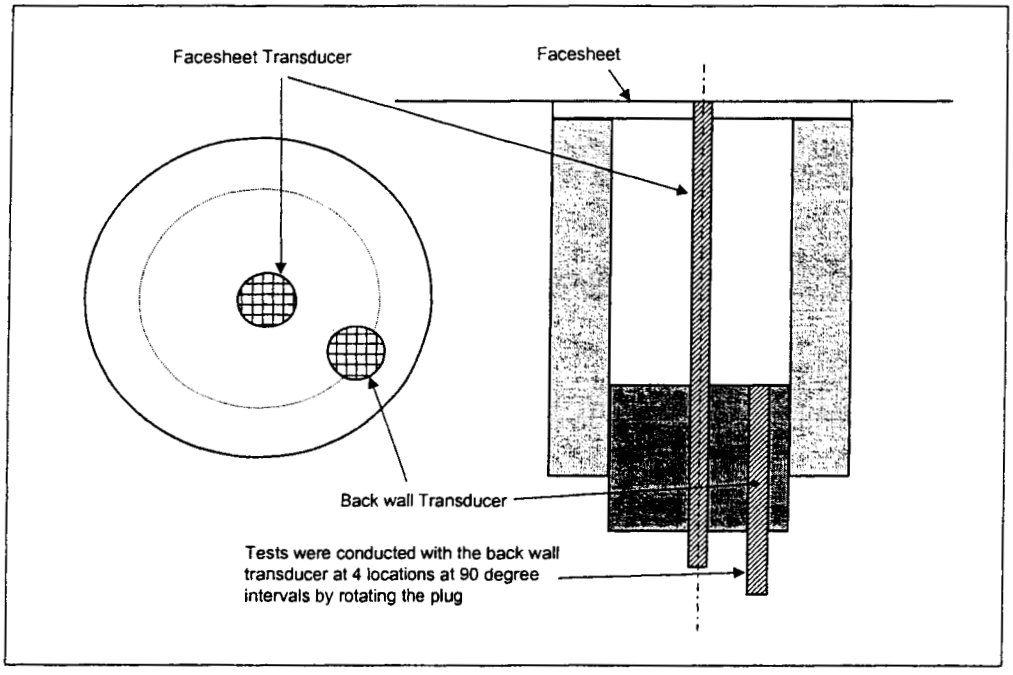

Figure 4-23. Schematic diagram of the setup for in-situ impedance measurements designed to study the effects of changing the location of the back wall transducer.

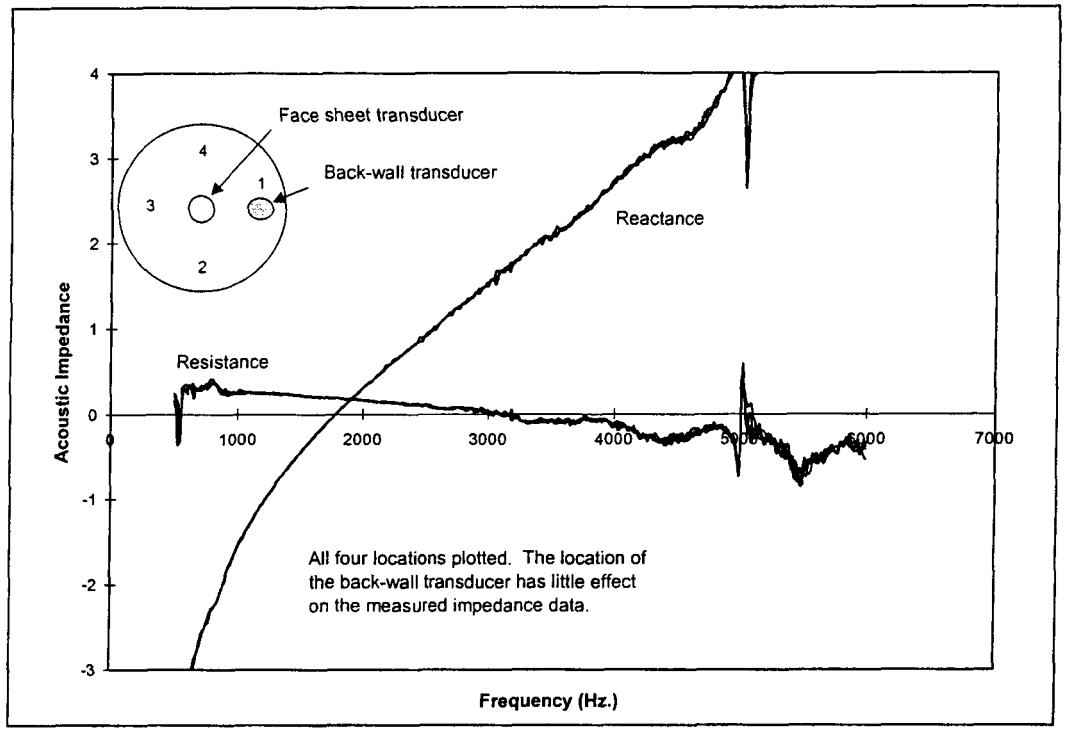

Figure 4-24. In-situ impedance measurement showing effects of changing the angular location of the back wall transducer.

Finally, in-situ impedance data were measured with a wiremesh-on-perforate face sheet. These measurements are presented in Figures 4-25 and 4-26. The acoustic resistance of approximately 1.5 ρc is in good agreement with the zero intercept of the measured steady (DC) flow resistance for the wiremesh face sheet (65 cgs Rayls). Note that the impedance data measured with discrete excitation is in good agreement with the data measured with broad band excitation. This is because of the "linear" character of the wiremesh material. Moreover, note that the reactance of the cavity plus face sheet is almost the same as the reactance of the cavity alone. This indicates that the mass reactance of the face sheet is governed by the thickness of the wiremesh alone. Compare this to the mass reactance for a perforated face sheet, as shown in Figure 4-18.

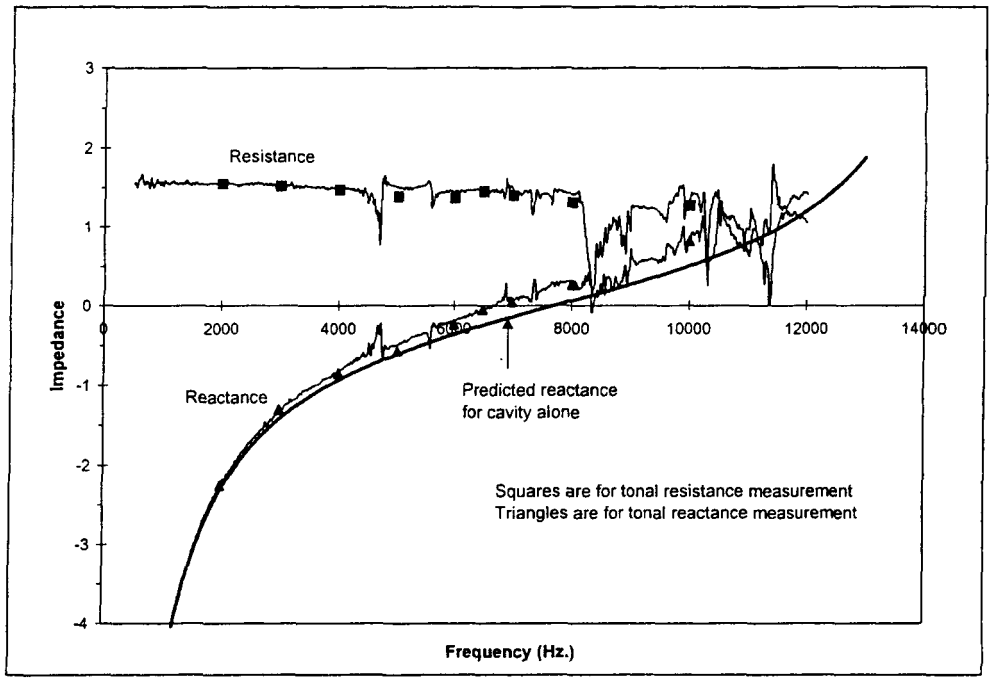

Figure 4-25. In-situ impedance measurement for a linear SDOF sample with a 1.120 cm. (0.441 in.) deep cavity and a wiremesh-on-perforate facesheet.

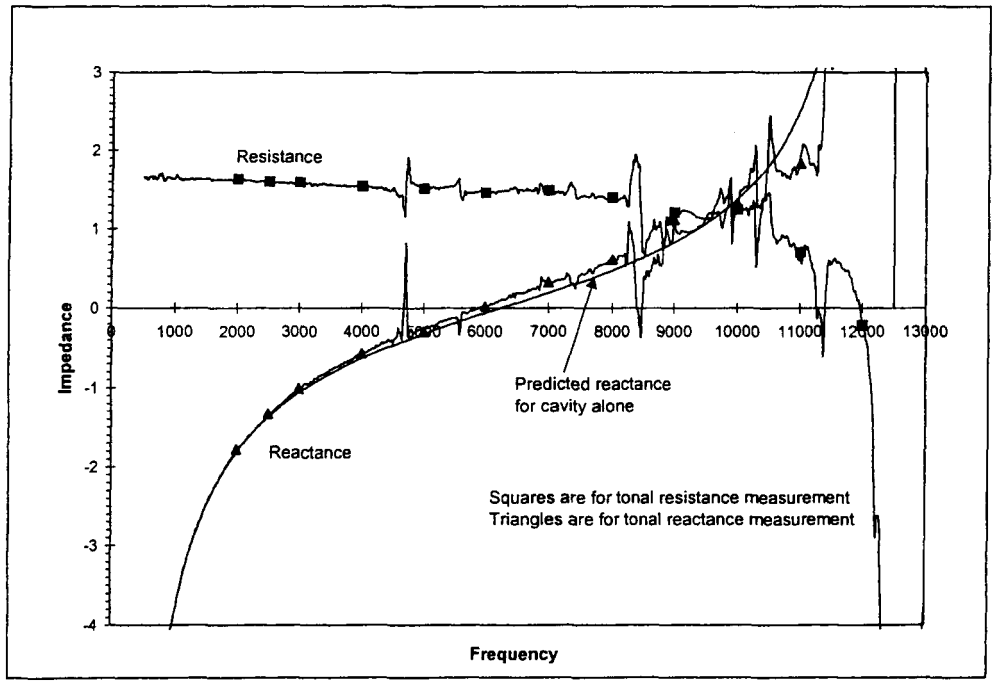

Figure 4-26. In-situ impedance measurement for a linear SDOF sample with a 1.379 cm. (0.543 in.) deep cavity and a wiremesh-on-perforate facesheet.

4.4 Conclusions and Recommendations

The preliminary tests were conducted to assess the feasibility of the in-situ method, for the measurement of the acoustic impedance of single-degree-of-freedom (SDOF) liner samples. Analysis of the measurement uncertainties was also carried out. From the results of this preliminary study, the following conclusions can be drawn.

- Measured acoustic resistance data are sensitive to small errors in the phase of the complex ratio of the acoustic pressures (referred to as the Transfer Function), measured at the face sheet and the back wall.
- In a typical grazing incidence sound field, the acoustic pressure over the surface of a SDOF liner sample, is not constant. The variation of the acoustic pressure is small (negligible) at low frequencies where the wave length is very large compared to the cavity dimensions. However at higher frequencies, this variation becomes significant and may give rise to unacceptable measurement uncertainty. For this reason, this technique is unlikely to be suitable for accurate measurements of acoustic impedance at high frequencies ($f > 6000$ Hz.).
- The measured transfer function is not affected by the angular or radial location of the back wall transducer.
- Further evaluation and development of the in-situ method is required before it can be reliably used to measure the acoustic impedance of SDOF liners in grazing flow conditions.

It is recommended that further experimental evaluation be carried out to develop and refine this measurement technique.

4.5 References

1. Dean P. D., "An In-Situ Method of Wall Acoustic Impedance Measurement in Flow Ducts," Journal of Sound and Vibration, Volume 34(1), pages 97 to 130, 1974.
2. Kooi J. W., and Sarin S. L., " An Experimental Study of the Impedance of Helmholtz Resonator Arrays Under a Turbulent Boundary Layer," AIAA-81-1998, October 1981.

5. Time-Domain Numerical Method to Predict Acoustic Impedance

5.1 Introduction

5.1.1 Basis and Advantages of the Time-Domain Model

5.1.1.1 Acoustic Model Geometry

The objective of this study was to develop a time-domain numerical model that represents a simple, isolated single-degree-of-freedom (SDOF) acoustic treatment hexcell cavity covered by a perforated faceplate. For the numerical calculation, the faceplate is modeled as a lumped mass inertia and resistance element with zero thickness. The lumped inertia and resistance models are obtained as time-domain representatives of the standard frequency-domain models for the DC flow resistance and mass reactance of a perforated plate.

The geometry of the cavity is shown in Figure 5-1. A known time-dependent acoustic pressure is applied to the outer surface of the faceplate. The applied pressure is defined in terms of its complex spectral components over a given range of frequencies. The cavity is modeled as a uniform acoustic medium, and the differential equations for the acoustic pressure and velocity are solved numerically in the space and time domains.

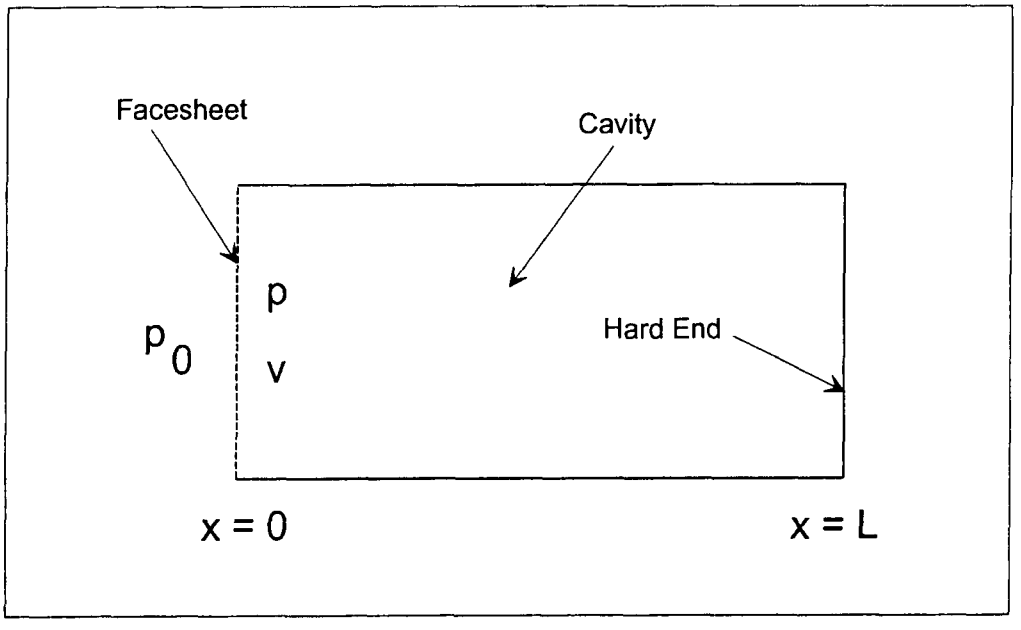

Figure 5-1. Geometry of SDOF resonator cavity.

5.1.1.2 The Acoustic Computation Numerical Method

The computation uses an advanced finite-difference numerical model to compute the acoustic propagation in the cavity. At the facesheet end of the cavity, pressure drop and continuity of acoustic velocity boundary conditions are enforced. At the hard end of the cavity, a hardwall, zero normal acoustic velocity boundary condition is enforced. The time history of the acoustic velocity at the plane of the faceplate is computed for an arbitrary, but known, broadband

acoustic pressure forcing function. The time histories of the excitation pressure and the acoustic velocity response at the faceplate are then Fourier transformed back to the frequency domain. The ratio of the pressure and velocity in each frequency band then gives the acoustic impedance spectrum.

5.1.1.3 Advantages of the Time-Domain Method

This may seem like unwarranted extra effort to result, essentially, in a frequency domain prediction of the impedance of a perforated plate resonator. The main advantage of the method over current frequency-domain acoustic impedance predictions is that it inherently incorporates the shape of the broadband pressure excitation spectrum into the computation. The frequency-domain acoustic impedance models lose this variable spectrum shape dependence by assuming that the acoustic resistance, for example, is a function of the overall rms acoustic velocity in the perforated plate orifice. The time-domain method is limited only by the assumptions made for the fluid mechanical models for the faceplate resistance and mass reactance.

Although current frequency-domain impedance prediction models appear to be adequate for predicting impedance of full-scale acoustic treatment panels up to about 10,000 Hz., it is hypothesized that there may be a spectral shape effect on acoustic treatment in the high frequency ranges of sub-scale treatment. The time-domain model was developed to determine whether or not the simpler frequency-domain models could be extended up to higher frequencies and to provide a tool for investigating excitation pressure spectral shape effects on impedance.

5.1.2 Results of Prior Study

5.1.2.1 Description of Numerical Model in Prior Study

This study is an extension of a prior effort which was reported upon completion of the first phase of the Contract[1]. Theoretical development of the method, much of which applies to the current effort, is presented in detail in Reference 1. The original finite-difference spatial scheme was a three-point central-difference formulation applied directly to the second order differential equation for acoustic pressure in one dimension. A two-step time increment scheme was applied to integrate in time from a set of quiescent initial conditions.

The nonlinearity in acoustic resistance of the faceplate had to be incorporated using an iterative technique incorporated into the numerical integration. This was probably the most suspect aspect of the entire original scheme.

The operation of the numerical analysis program simulates the physical process of measuring acoustic impedance. At time zero, the pressure source is turned on, and the system is integrated in time a sufficient number of steps for all transient effects to decay. Then a digital signal processing data acquisition phase is initiated and a discrete time history of the acoustic pressure and velocity is acquired for FFT analysis. An arbitrary number of frequency averages can be applied.

The pressure source is defined in terms of its complex pressure coefficient (or component) in each narrowband frequency bin. If the computation is aimed at comparison with measured data, the pressure source is usually given only in terms of the Sound Pressure Level (SPL) in each frequency bin, such that the relative phasing among frequency components is generally not known. A standard procedure is to assign a uniformly distributed random phase for

each pressure frequency component. Probably the most difficult part of setting up a computation case is the process of making sure the narrowband Fourier analysis parameters (sampling frequency, block size, etc.) are commensurate with the requirements of the numerical integration (grid size, time step, numerical stability criteria).

5.1.2.2 Key Results from Prior Study

The most significant issue for the previous study, from the numerical analysis viewpoint, was the large number of points per wavelength required to obtain convergence of the predicted acoustic impedance. At the time, this was attributed to the simplicity of the three point central finite-difference scheme. One of the conclusions of the prior study was that adopting one of the more advanced acoustic wave propagation computational aero-acoustics (CAA) schemes currently under development might improve the speed and accuracy of the computation.

A second result of the previous study was that there seemed to be a general tendency for the time-domain model to over-predict both the acoustic resistance and the acoustic mass reactance of the perforated plate liner, compared to both frequency-domain impedance prediction models and measured impedance data. This, again, was initially ascribed to inaccuracies in the numerical method, specifically the nonlinear resistance iteration scheme, and it was hoped a more advanced numerical model might improve the impedance prediction as well as the computational efficiency.

5.2 Tam Numerical Integration Scheme

5.2.1 Modifications for New Numerical Scheme

One of the foremost time-domain CAA schemes available today is the Tam dispersion-relation-preserving 7-point stencil finite difference time-domain scheme[2,3,4,5,6]. As detailed below, this scheme was adapted to the perforated plate model. Lumped impedance models for the faceplate were kept the same as the earlier computation, as were the source pressure model and the Fourier analysis method.

5.2.2 Differential equations

Rather than applying the finite difference scheme to the second order differential equation for the acoustic pressure (which was the approach for the previous study), Tam starts with the system of two first-order differential equations in acoustic pressure and velocity,

$$\frac{\partial p}{\partial \tau} + \rho_0 c \frac{\partial u}{\partial x} = 0 \tag{5-1}$$

and

$$\frac{\partial u}{\partial \tau} + \frac{1}{\rho_0 c} \frac{\partial p}{\partial x} = 0 \tag{5-2}$$

where p is the acoustic pressure, u is the acoustic velocity, c is the speed of sound, ρ_0 is the mean air density, and τ is the nondimensional time,

$$\tau = ct \tag{5-3}$$

The acoustic medium in the cavity is assumed to be uniform, and no mean flow is allowed. The acoustic propagation in the cavity is assumed to be one-dimensional, which assumes that the cavity cross-dimension is much smaller than the shortest wavelength in the problem.

5.2.3 Dispersion Relation Preserving 7-Point Stencil

Tam proposes solving these equations for the acoustic propagation using a 7-point finite difference stencil coupled with a four-level explicit time marching scheme. In order to damp the short waves that are contaminants of the computational acoustics, Tam adds artificial damping to the finite difference scheme.

The Tam 7-point centered finite difference stencils with damping for acoustic velocity and acoustic pressure are given by

$$u(\ell,5) = u(\ell,4) + \frac{\Delta\tau}{\Delta x}\sum_{n=0}^{3}\left\{b_n\left[-\sum_{j=-3}^{3}a_j p(\ell+j,4-n) - \frac{\Delta x}{R_a}\sum_{j=-3}^{3}d_j u(\ell+j,4-n) - \frac{\Delta x}{R_a}\right]\right\} \tag{5-4}$$

and

$$p(\ell,5) = p(\ell,4) + \frac{\Delta\tau}{\Delta x}\sum_{n=0}^{3}\left\{b_n\left[-\sum_{j=-3}^{3}a_j u(\ell+j,4-n) - \frac{\Delta x}{R_a}\sum_{j=-3}^{3}d_j p(\ell+j,4-n) - \frac{\Delta x}{R_a}\right]\right\} \tag{5-5}$$

respectively, where ℓ is the index for the center grid point in x, Δx is the grid spacing, and the time step goes from the current time (index = 4) to the next time (index = 5). The coefficients for the x-grid, a_j, the coefficients for the time marching, b_n, and the coefficients for the damping term, d_j, have been determined and provided by Tam and Dong in Reference 3 (p.10). The constant R_a is the damping coefficient, and can be thought of as an artificial Reynold's number.

A diagram of the 7-point centered stencil spatial discretization is shown in Figure 5-2. Tam also provides coefficients for shifted forward and backward finite difference stencils, which are required as the x-grid approaches the boundary conditions at either end of the tube.

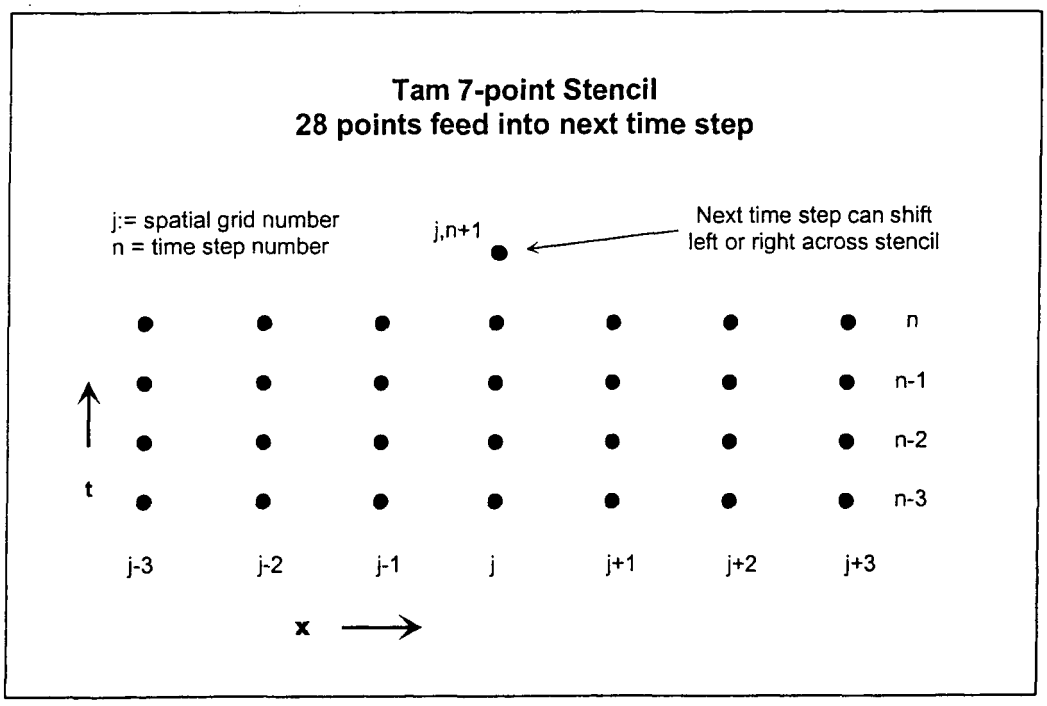

Figure 5-2. Diagram of Tam 7-point finite difference stencil.

5.2.4 Accuracy, Stability and Damping

Based on experience with the method, Tam and Auriault recommend at least 7 mesh points per wavelength (Reference 6, p. 4). This is appreciably less than the requirement for the previous 3-point finite difference scheme.

Numerical instabilities can arise in the finite difference/time marching scheme unless the time increment is chosen to be adequately small (Reference 2, pp. 268-270). The criterion for numerical stability is given in terms of the Courant number, defined as

$$C_n = \frac{\Delta\tau}{\Delta x} \tag{5-6}$$

For the current application, it can be shown that numerical stability is obtained (Reference 4, pp. 28-30) when the Courant number is less than 0.1086.

The rationale behind and derivation of the artificial selective damping coefficients is presented in Tam, Webb, and Dong, Reference 4, pp. 23-27. The damping coefficients are optimized to eliminate short wavelength parasitic waves while having minimal effect on the long acoustic waves.

5.2.5 Implementation of Boundary Conditions

The boundary condition for the acoustic velocity at the hardwall end of the tube, x = L, can be written simply as u = 0. At the faceplate end of the tube, the impedance boundary condition, in time-domain form, can be written as

$$p_0 - p = R_{LIN} u - R_{NL} u|u| - \frac{\rho_0 c t'}{\sigma C_D} \frac{\partial u}{\partial \tau} \tag{5-7}$$

where

p_0	=	time-dependent applied acoustic pressure
p	=	acoustic pressure on right side of faceplate, x = 0
R_{LIN}	=	linear part of acoustic impedance
R_{NL}	=	coefficient for nonlinear part of acoustic impedance
ρ_0	=	density of air
c	=	speed of sound
t'	=	effective thickness of orifice (faceplate thickness plus end correction)
σ	=	faceplate porosity
C_D	=	orifice discharge coefficient

This relation is derived in Reference 1.

The finite-difference discretization of the boundary condition equations is accomplished using shifted versions of Tam's 7-point stencils and a single ghost point just outside either end of the tube. One advantage of using the two first order differential equations as the basis for the model is that the nonlinear resistance boundary condition can be incorporated without requiring an iterative method to achieve convergence of the acoustic velocity at the faceplate.

5.3 Digital Signal Processing

5.3.1 Determination of Impedance in the Frequency Domain

The numerical integration in space and time gives the time history of the acoustic velocity at the faceplate. The applied acoustic pressure time history is obtained by summing the frequency components in a Fourier series. By taking FFT's of the pressure and velocity time histories, the acoustic pressure and velocity can be obtained in the frequency domain, exactly as they would be if measured by sensors transmitting signals to spectral analyzers.

The integration time step Δt will generally be much smaller than the digital signal processing time sampling interval of the time histories. It is necessary to determine how many time integration steps are required between each data element recorded for FFT processing. The intermediate values are not recorded.

Since the source is suddenly "switched on" at t = 0, an initial transient response can be expected in addition to the steady-state response. Several steps are taken to assure that all transient content has decayed before digital data acquisition commences:

1. The applied pressure signal is "ramped up" by multiplying by a linear function between zero and one over a time length equal to three of the longest periods (lowest frequency bin) in the pressure signal.

2. Following this, the integration runs for a settling time of at least three longest periods. The number of periods of settling time can be increased arbitrarily as part of the program input.

The damping of the signal is due to the resistance of the facesheet. The lower this resistance, the longer the transients should be in evidence.

DSP data for acoustic pressure and velocity is acquired at a given sampling rate, the number of samples acquired depending on the block size (which must be a power of 2). FFT's are applied to the pressure and velocity time histories, giving their spectral content. The spectral content of the pressure should reproduce the input pressure frequency coefficients, in both magnitude and phase, within the accuracy of the DSP process. The impedance at each frequency is obtained by dividing the complex pressure by the complex velocity.

5.3.2 Parameter Determination for the Signal Processing Parameters

The numerical integration procedure, the digital signal processing, and the measured data set (if comparing prediction and measurement) provide a multiple set of requirements and constraints that must be simultaneously accommodated before a computer run can be made. The measured impedance and SPL data, for instance, is usually in the form of a narrowband spectrum of given frequency resolution. The data will have a lowest and highest frequency of interest, which may not run from zero to the Nyquist frequency of the measurement FFT. If the frequency resolution is too narrow, giving too many values to be practical for the numerical model, it may be necessary to combine the data into wider resolution binwidths.

For the numerical processing, it is necessary to decide how many grid points to use for the shortest wavelength (highest frequency) of interest. Tam recommends a minimum of seven grid points per wavelength for the 7-point stencil model. For small resonator cavity depths, the seven point stencil requires at least 7 grid points (preferably at least 9) in the cavity. This may be more than needed to satisfy the points per wavelength requirement. Given a grid spacing, a numerical integration time step size must be chosen to satisfy the Courant number stability criterion.

This numerical integration time step, in turn, must be sized just right such that an integral number of time steps gives the proper data acquisition sampling interval to give a sampling rate, given the data acquisition block size, that gives a Nyquist frequency that is at least twice as high as the highest frequency in the applied pressure.

A MathCAD worksheet was prepared to determine the commensurate numerical integration and signal processing parameters for a given case. The input parameters are the frequency resolution bandwidth (the input pressure spectrum and the output impedance spectrum must have the same resolution bandwidth), the data acquisition block size, the Courant number, the number of grid points per highest wavelength, and the number of numerical time steps between data acquisition sampling points. This worksheet is shown in Figure 5-3.

Additional inputs related to the numerical integration and DSP are the numerical damping parameter, the number of extra cycles (longest periods) of transient settling time, the number of frequency averages, and the number of cases for which the input pressure phase is varied randomly. The last two options, related to averaging procedures, are discussed in the next section.

5.3.3 Averaging Processes

The source pressure coefficient input to the program allows a complex pressure coefficient to be input at each frequency. The applied faceplate pressure is then calculated at any instant of time from the Fourier expansion formula:

$$p_0(t) = \sum_{n=1}^{NFRQ} P_n e^{i\omega_n t} \tag{5-8}$$

where NFRQ is the number of pressure frequencies and ω_n is the n^{th} circular frequency. Usually, all that is available from an impedance measurement is the SPL spectrum of the applied pressure, which gives the magnitude of P_n, but the narrowband phase is not known. The program provides the capability of applying random phases to the P_n such that a phase angle uniformly distributed between 0 and 2π radians is applied without changing the amplitude.

Up to 32 frequency averages can be run for an individual set of P_n values. Frequency averaging is accomplished in the same manner as a spectral analyzer would, such that FFT bins are averaged over a sequence of acquired data blocks.

An additional capability of ensemble averaging over sets of randomly phased pressure coefficients is provided by the program. For each case, a new set of random phasings is applied to each pressure coefficient, holding the magnitude constant. Standard deviations of the resistance, reactance, rms pressure, and rms velocity can be obtained for a sufficient number of ensemble averages.

Frequency resolution for ZORF6

cgs system

Run prior to ZORF6 run to match given spectral frequencies
Use adjusted delta t stability coefficient as input to ZORF6

Cavity depth, cm $D := 1.27$ $D = 1.27$ Air temperature, degF $Tdf := 71.3$

Speed of sound, cm/sec $c := 2.54588\sqrt{Tdf + 460}$ $c = 34425.555$

Set Highest frequency in source $f_{mx} := 15360$ <-- This should be (block size) x Δf /4

Shortest wavelength, cm $\lambda := \frac{c}{f_{mx}}$ $\lambda = 2.241$ Nyquist frequency $f_c := 2 \cdot f_{mx}$ $f_c = 30720$

Block size $MB := 256$ Choose Number of grid points per wavelength $NPPL := 15$

Number of grid divisions in cavity $NDIV := floor\left(\frac{D \cdot NPPL \cdot f_{mx}}{c}\right) + 1$ $NDIV = 9$ MUST BE >= 7

Grid spacing, cm $\Delta x := \frac{D}{NDIV}$ $\Delta x = 0.14111$

Nominal stability coefficient $Ks := 0.1086$

Frequency resolution $df(NS, Ks) := \frac{1}{Ks} \cdot c \cdot \frac{NDIV}{MB \cdot D \cdot NS}$

Choose combination of NPPL and NS to get as close to DF as possible but staying below (use tables on next page to get NS), then adjust Ks by reducing slightly to match DF. Adjusted Ks = Kx found by root-search

Desired frequency binwidth $DF := 240$

Number of steps between data samples $NS := 37$

Approximate delta f

$df(NS, Ks) = 237.163704$

$F(x) := DF - df(NS, x)$ $x := Ks$ $Kx := root(F(x), x)$

Adjustment to Stability Coeff
Must end up less than 0.1086 $Kx = 0.107316576$ Revised delta freq $df(NS, Kx) = 240$

Numerical integration time step, sec $\Delta t := Kx \cdot \frac{D}{c \cdot NDIV}$ $\Delta t = 4.39893 \cdot 10^{-7}$ $\Delta\tau := c \cdot \Delta t$ $\Delta\tau = 0.015144$

Sampling time interval $dts := \frac{1}{MB \cdot df(NS, Kx)}$ $dts = 1.62760 \cdot 10^{-5}$ $NS \cdot \Delta t = 1.627 \cdot 10^{-5}$

Nyquist freq Sampling freq Max Pressure freq

$fnq := \frac{1}{2 \cdot dts}$ $fnq = 30720$ $fsmp := \frac{1}{dts}$ $fsmp = 61440$ $fmax := \frac{1}{4 \cdot dts}$ $fmax = 15360$

Record length,sec

$Tr := MB \cdot dts$

$Tr = 0.004167$

$\Delta f := \frac{1}{MB \cdot dts}$ $\Delta f = 240$ $\frac{1}{Tr} = 240$

Courant number

$Cn := \frac{c \cdot \Delta t}{\Delta x}$ $Cn = 0.107317$

Figure 5-3 MathCAD program for determining grid and DSP parameters for input to numerical integration program.

5.4 Computer Program ZORF7

The latest version of the computer program that performs the numerical integration in the time domain for the resonator model and then produces the resulting impedance spectrum is named ZORF7. It is written in Microsoft FORTRAN and runs on a PC in Windows 95. The length of the computer runs can vary from a few minutes to 10-12 hours, depending on the grid size, number of ensemble and frequency averages requested and the speed of the PC.

The computer program has been upgraded to full double precision, including both the numerical integration and the FFT data analysis. Version ZORF6, which performed the digital signal processing in single precision, was also used for some of the results presented here. It was found that the upgrade to double precision had little effect on the predicted impedance for most cases. The FORTRAN code should be portable with minimum modifications to compilers on other computer systems.

Output from the program is an ASCII data file reproducing the input data, giving the computed impedance and rms acoustic velocity at each frequency, and giving the standard deviations of the resistance, reactance, rms pressure, and rms velocity at each frequency when ensemble averaging is requested.

5.5 Comparison of Predicted and Measured Impedance

5.5.1 Comparison of Frequency-Domain and Time-Domain Predictions

The first test of the updated time-domain computation was to see whether it agreed with the frequency-domain prediction for a simple linear faceplate SDOF liner with constant SPL broadband excitation. Figure 5-4 shows the exact agreement between the two models for a 2.54 cm. deep liner with a 41.5 cgs Rayl linear faceplate. Mass reactance is based on an assumed perforated plate of 6% porosity and 0.2 cm effective orifice length.

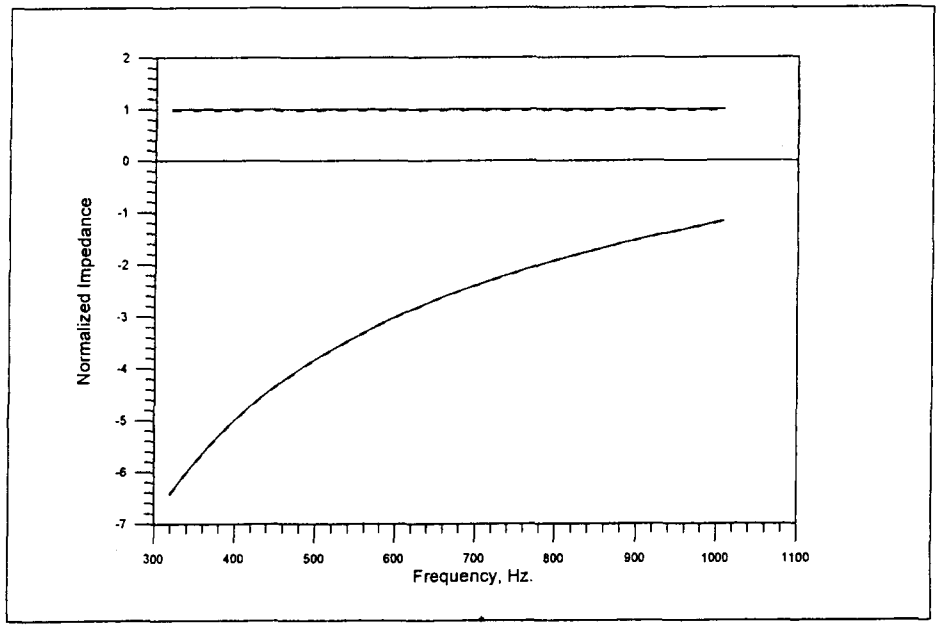

Figure 5-4 Comparison of impedance predicted by time-domain and frequency-domain models; solid line, time-domain; dashed line, frequency-domain.

For the nonlinear resistance faceplate case, the agreement between the models is not as good. Figure 5-5 shows the comparison for the same 6% porosity, 2.54 cm. deep liner with faceplate thickness of 0.0762 cm (0.03 in.) and hole diameter of 0.1321 cm. (0.052 in.). The excitation pressure is held constant at 150 dB for each 16 Hz. narrowband frequency bin between 320 Hz. and 1008 Hz, giving an OASPL of 166.4 dB. The DC flow resistance values used for this case (based on an analytical model) were R_{LIN} = 0.5555 cgs Rayls and R_{NL} = 0.2900 cgs Rayls per cm/sec.

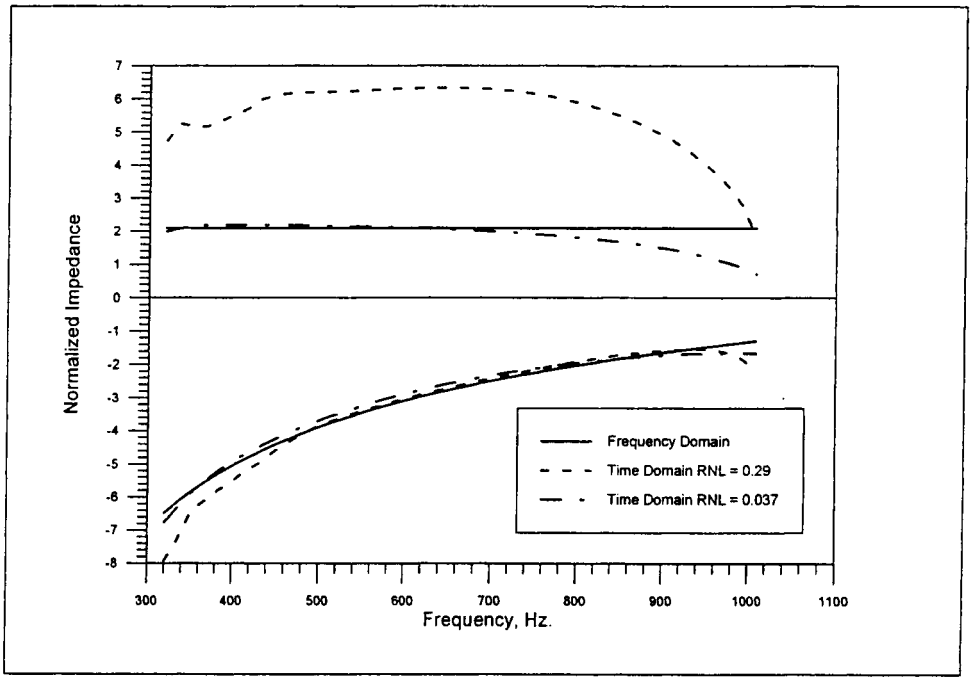

Figure 5-5 Comparison of impedance predicted by time-domain and frequency-domain models for a nonlinear resistance faceplate SDOF liner.

Note that the time-domain model overpredicts the resistance by an appreciable amount. If, however, the nonlinear resistance coefficient, R_{NL}, is reduced from 0.29 to 0.037 for the time-domain model, note that the agreement in both the resistance and reactance improves. This characteristic difference between the frequency-domain and time-domain model was at first thought to be a flaw in the time-domain computation. It will be argued below that what is necessary is a re-interpretation of the nonlinear resistance coefficient for application to the time-domain model.

5.5.2 Perforate SDOF with Single Frequency Excitation

A two-microphone in-situ impedance measurement was made in the GEAE duct for a 5.2% porosity SDOF perforated resonator of 1.27 cm (0.5 in.) depth. The resonator was excited by pure tone pressure signals for a range of frequencies and SPL's. The faceplate thickness for the resonator was 0.08128 cm (0.032 in.) and the hole diameter was 0.127 cm (0.050 in.). A comparison is made between the measured data for a 5000 Hz. pure tone excitation at 142.5 dB and the corresponding time-domain model prediction.

Rather than using measured DC flow resistance data to determine the linear and nonlinear resistance parameters for input to the time-domain program, the resistance parameters were extracted from the impedance measurement. Since the rms acoustic velocity at the faceplate is determined as part of the in-situ measurement, the measured resistance was plotted versus the rms acoustic velocity for measurements at a number of frequencies. Figure 5-6 shows the resulting linear curve fit to the resistance data, giving R_{LIN} = 15.397 cgs Rayls and R_{NL} = 0.13578 cgs Rayls per cm/sec.

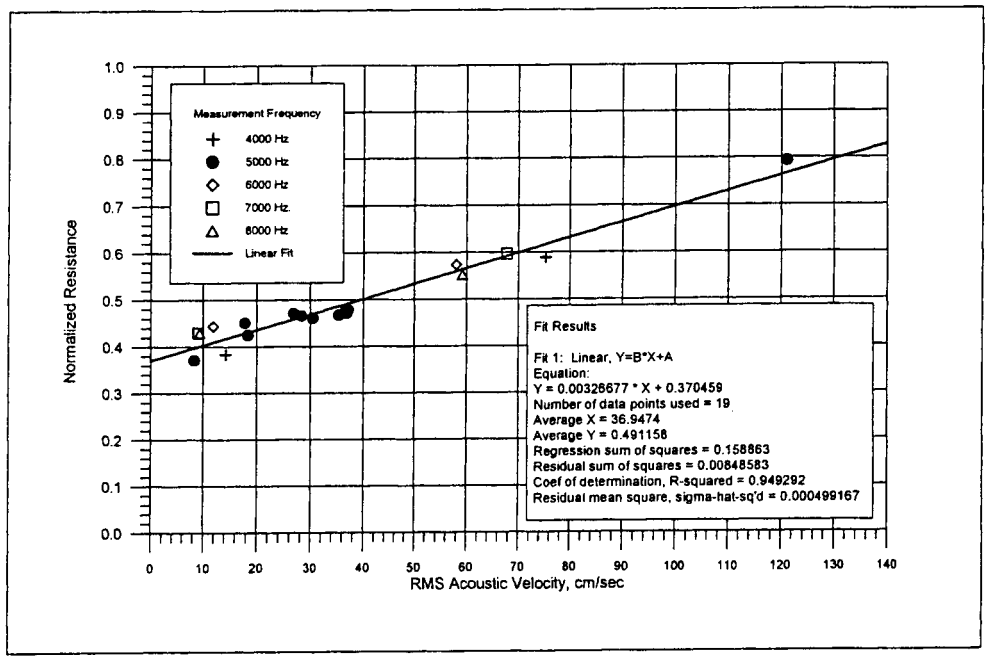

Figure 5-6 Linear fit to measured resistance for 5.2% porosity faceplate based on 2-microphone measurement at 5 pure tone frequencies, various SPL's.

Similarly, the mass reactance end correction coefficient, defined by ε in the frequency-domain formula for mass reactance,

$$\frac{X_m}{\rho c} = \frac{k(t+\varepsilon d)}{\sigma C_d} \tag{5-9}$$

was obtained as a function of rms acoustic velocity from the measured reactance data, by subtracting the cavity reactance, -cot(kL), from the measured reactance. This is shown in Figure 5-7, where a correlation due to R. Motsinger[7] is also plotted, for comparison. The measured results indicate that the end correction is not a strong function of rms acoustic velocity over the range considered, so that ε is taken to be constant at its average value of 0.298 for the prediction.

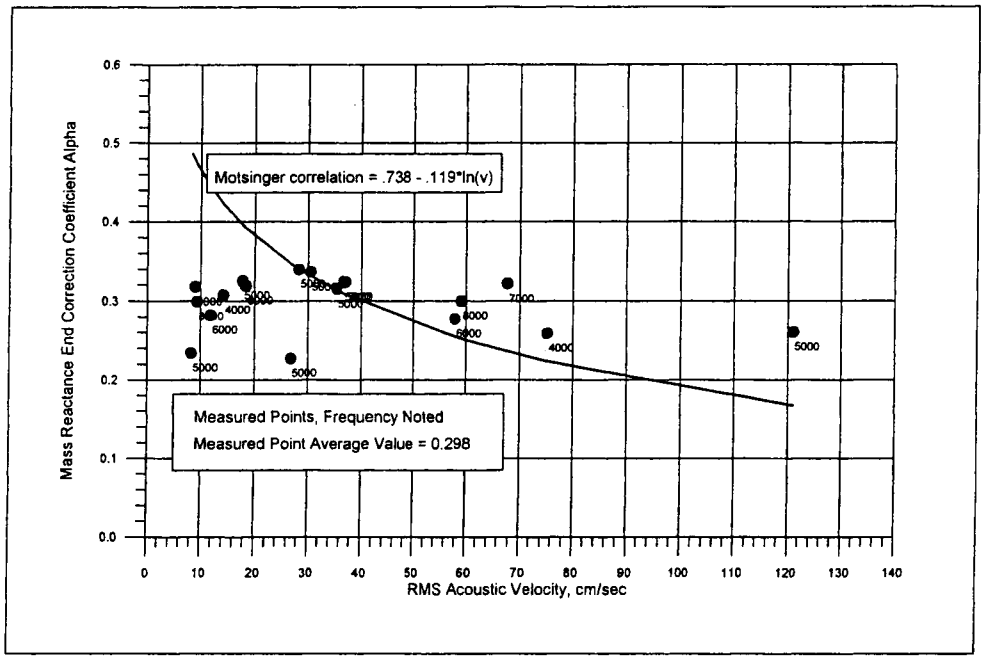

Figure 5-7. Mass reactance end correction coefficient extracted from measured reactance for 5.2% perforated facesheet, based on 2-microphone measurement at 5 pure tone frequencies and various SPL's.

Using the linear and nonlinear resistance and the mass reactance end effect coefficient derived from the measured data in the ZORF7 program, for a pure tone at 5000 Hz. with an SPL of 142.5 dB, the predicted impedances shown in Table 5-1 are obtained.

Table 5-1 Predicted and Measured Impedances for Perforated Plate SDOF Resonator for 5000 Hz. Pure Tone at 142.5 dB SPL.

Method	C_d	Resistance	Reactance	U_{rms}
Measured		0.478	1.707	36.7
Predicted Frequency-domain	0.76	0.459	2.309	27.3
Predicted Frequency-domain	1.0	0.492	1.650	37.3
Predicted Time-domain	0.76	0.475	2.311	27.2
Predicted Time-domain	1.0	0.516	1.651	37.1
Predicted Time-domain	0.974	0.512	1.706	36.0

Different assumptions were made regarding the orifice discharge coefficient, C_D, for the prediction. Note that the conventional choice of $C_D = 0.76$ for the frequency-domain model tends to give an over-prediction of mass reactance. Increasing C_D to 1.0 brings the reactance closer to

the measured value, and the resistance goes from just below the measurement to just above. The same behavior with respect to C_D occurs for the time-domain model, which gives results very similar to the frequency-domain model. Arbitrarily adjusting the discharge coefficient to a value of 0.974 for the time-domain model brings the reactance very close to the measured value, although the resistance is still slightly high.

Through hindsight, both the frequency-domain and the time-domain models could be made to match the measured value by appropriate adjustment of the orifice discharge coefficient and the nonlinear resistance coefficient. This is not a useful procedure unless one has a rationale for making these adjustments, for they are likely to be different for each liner configuration.

5.5.3 Full Scale 4.43% Perforate SDOF with Broadband Excitation

The first broadband excitation comparison is for a full-scale perforated plate resonator with the following design parameters:

Porosity = 4.43%

Cavity depth = 1.905 cm. (0.75 in.)

Faceplate thickness = 0.0787 cm (0.031 in.)

Hole diameter = 0.1151 cm (0.0453 in.)

Figure 5-8 shows the results of a DC flow resistance measurement, which was used to determine the linear and nonlinear resistance coefficients. The mass reactance is obtained from the analytical model. Figure 5-9 shows the SPL spectrum for the liner excitation, which has an overall SPL of 149 dB. The original measured data was converted from 8 Hz. narrowband frequency resolution to 192 Hz. bandwidths.

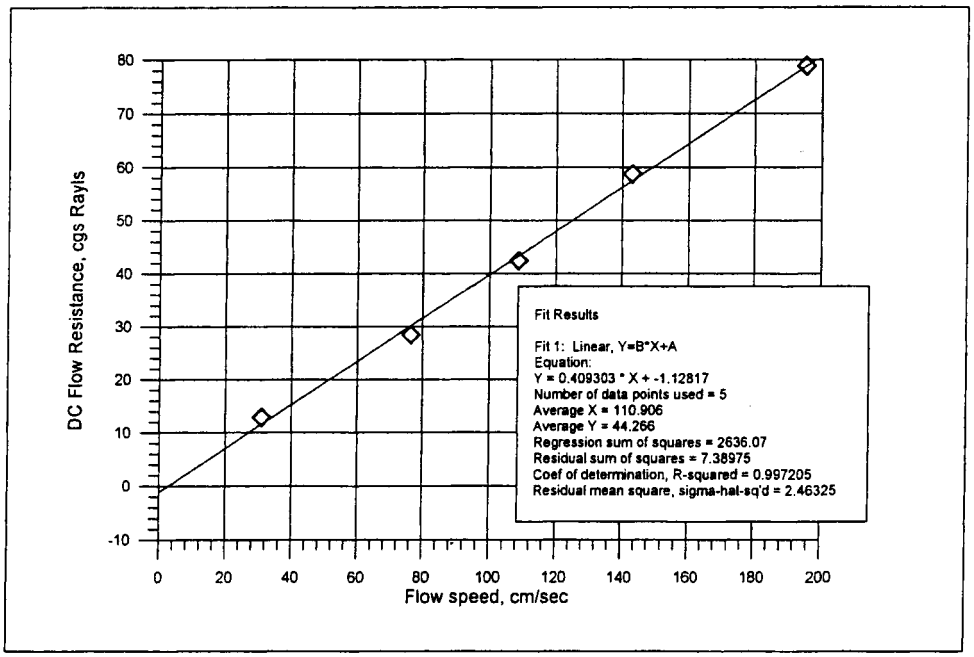

Figure 5-8. DC flow resistance measurement and linear curve fit for 4.43% porosity perforated sheet.

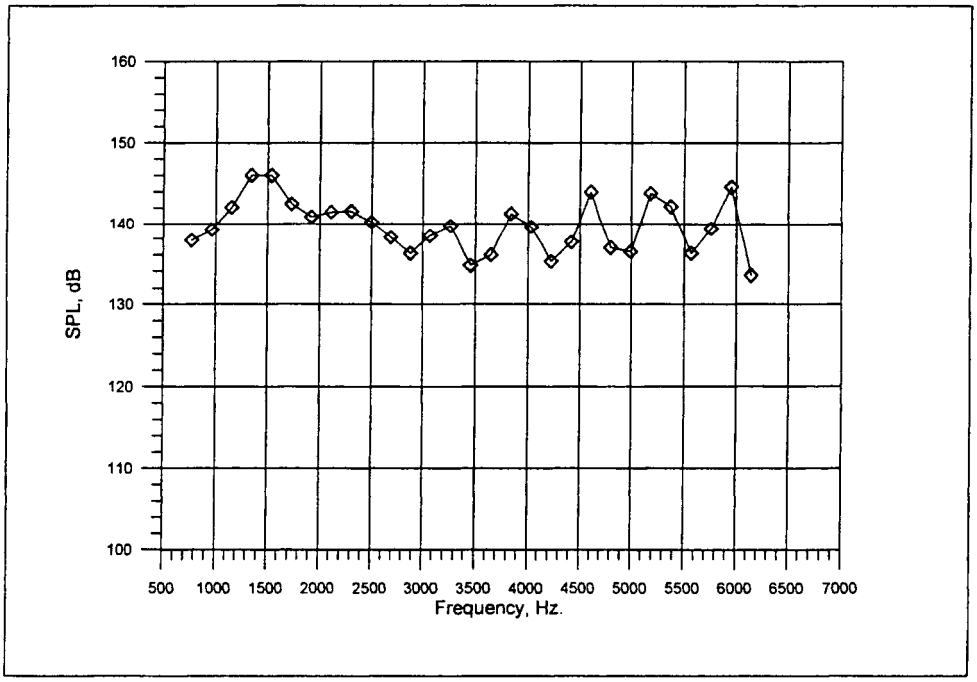

Figure 5-9 Excitation pressure SPL, dB, for 4.43% perforated plate resonator.

For this case, the first prediction made of the impedance using the time-domain model was done making no adjustments to the resistance and mass reactance models. The measured DC flow resistance coefficients were used for the resistance, and the full mass reactance model was used for the mass reactance, assuming an orifice discharge coefficient of 0.76. The results are shown in Figure 5-10. While the resistance is fairly close, there is a large over-prediction of the mass reactance by the time-domain model.

In an attempt to see how close the time-domain model could come to the measured impedance given the freedom to adjust the nonlinear resistance coefficient and the mass reactance (using an arbitrary mass reactance multiplication factor), these two parameters were iterated to minimize the difference (averaged over frequency) between the predicted and measured resistance and the measured and predicted reactance.

The results of this iteration are shown in Figure 5-11. The nonlinear resistance coefficient, R_{NL} was reduced by a factor of 0.8026, and the mass reactance was multiplied by a factor of 0.42. Also shown in the figure is the frequency-domain impedance prediction, which was also adjusted for a better fit by reducing the end correction factor from the conventional 0.85 to 0.36. With adjustments, both predictions show excellent agreement with measurement with the exception of the highest frequency points, for which the measurements are suspect.

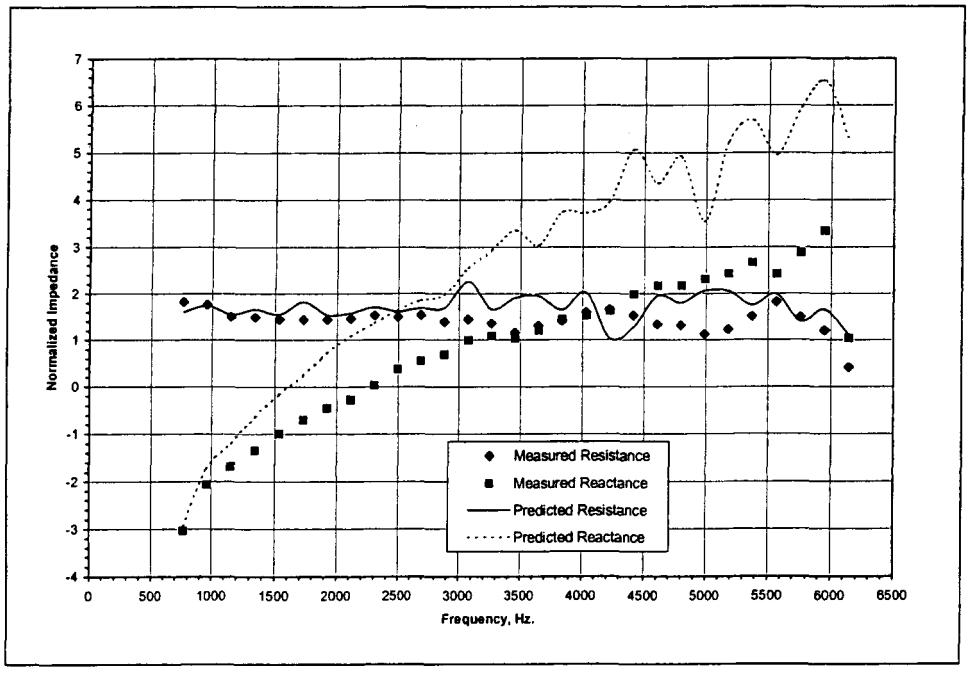

Figure 5-10. Comparison of predicted and measured impedance for 4.43% porosity resonator using nominal (unadjusted) models for resistance and mass reactance

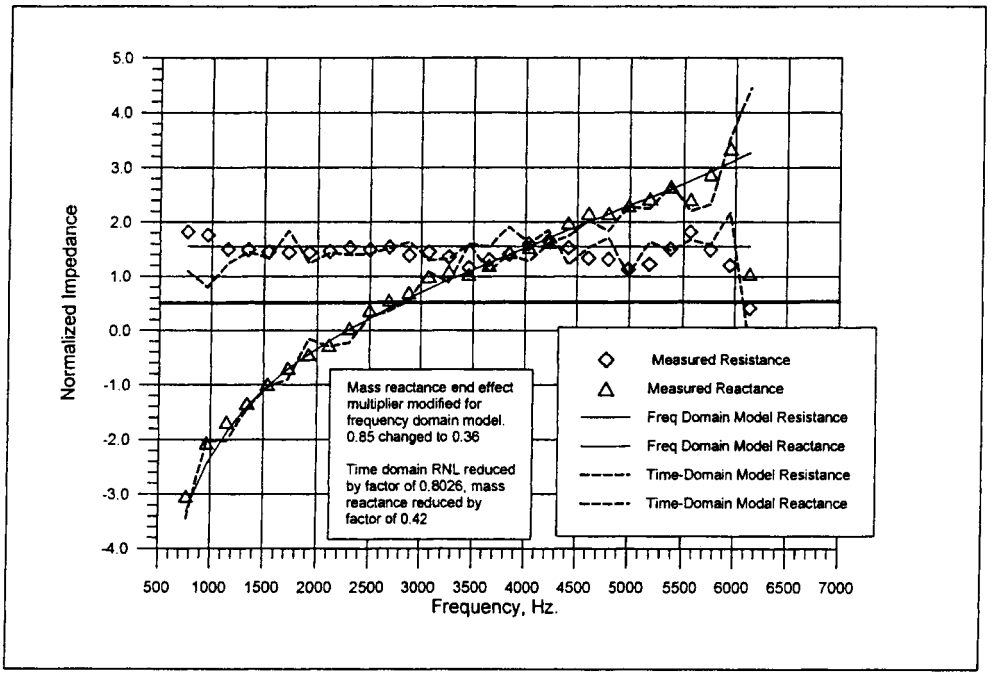

Figure 5-11. Comparison of predicted and measured impedance for time-domain and frequency-domain models for 4.43% porosity resonator.

5.5.4 One-Half Scale 8.0% Perforate SDOF with Broadband Excitation

A second perforated plate SDOF resonator with a higher porosity and a lower scale factor was chosen to examine the comparison of predicted and measured impedance for the time-domain model when extended to higher frequencies. In this case, the resonator parameters are:

Porosity = 8.0%

Cavity depth = 1.27 cm (0.5 in.)

Facesheet thickness = 0.035 cm (0.012 in.)

Hole diameter = 0.0508 cm. (0.02 in.)

The frequency range considered is 2640 Hz. to 13440 Hz. in 240 Hz frequency resolution bandwidths. The overall SPL is 130 dB (a spectral plot is shown below). The resistance parameters are obtained from DC flow resistance measurements, and are

R_{LIN} = 0.8999 cgs Rayls

R_{NL} = 0.14076 cgs Rayls/(cm/sec)

First, consider the nominal prediction of impedance using the time-domain method. This is compared with the measured data and the frequency-domain prediction in Figure 5-12. Note the reasonably good agreement even without adjustments for frequencies up to about 10,000 Hz. Above 10,000 Hz., both the prediction and the measurement begin to show strong variations with frequency. Note that the frequency-domain prediction shows no strong variations in the high

frequency range. For the time-domain prediction, 20 ensemble averages and 3 frequency averages were used.

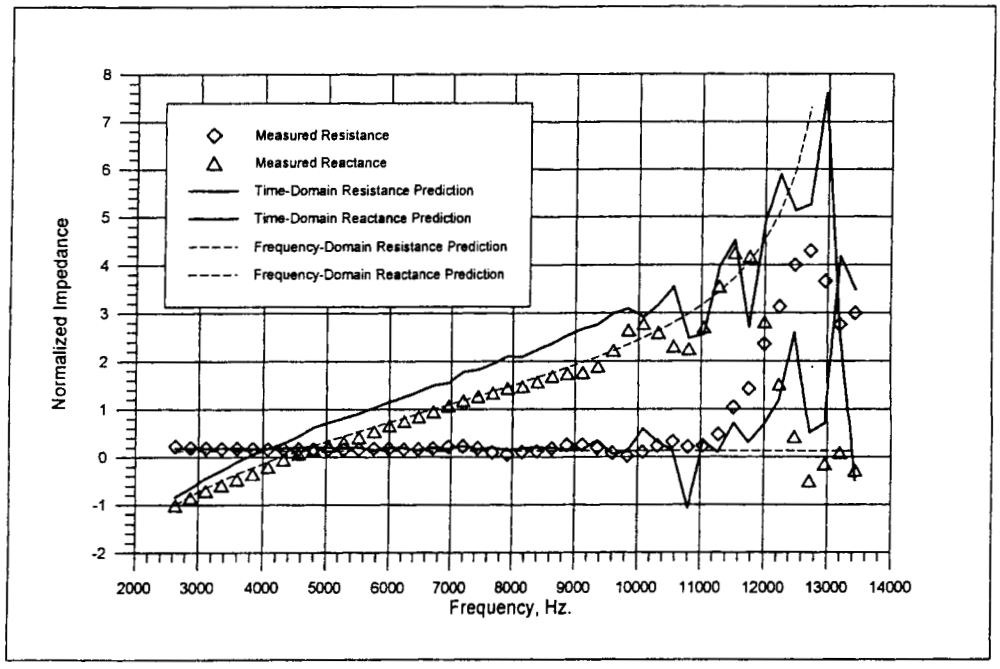

Figure 5-12. Comparison of measured and predicted impedance for 8% porosity, 1.27 cm deep resonator, nominal (unadjusted) case. 20 ensemble averages, 3 frequency averages.

The strong variations in the measured data would generally have been ascribed to problems with the measurement apparatus, and this may well be the case. The question arises, are the variations in the time-domain model due to numerical instabilities, or is there some sensitivity in the determination of impedance at high frequencies to which both the time-domain method and the measurement are subject?

Before examining this high frequency behavior, Figure 5-13 shows a plot of predicted versus measured impedance for an adjusted time-domain model, in which the nonlinear resistance coefficient has been reduced by a factor of 0.9 and the mass reactance has been reduced by a factor of 0.63, greatly improving the agreement between predicted and measured. The frequency-domain model was not adjusted. For this case, 10 frequency averages and 60 ensemble averages were used for the time-domain prediction.

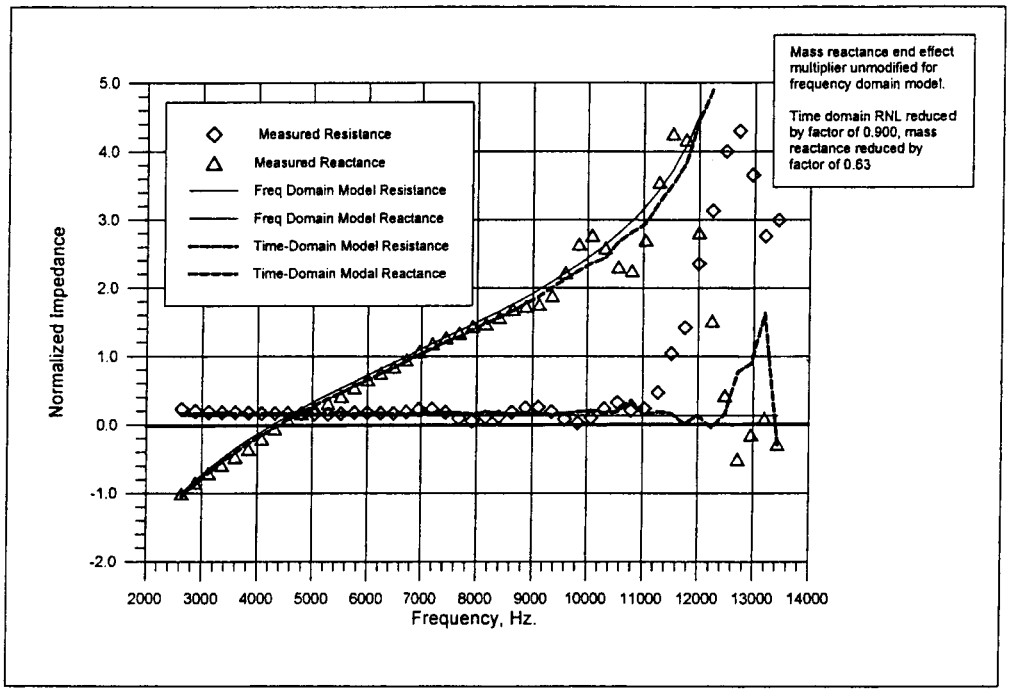

Figure 5-13. Comparison of predicted and measured impedance for 8.0% facesheet resonator for adjusted time-domain case, using 60 ensemble averages and 10 frequency averages.

The nominal case time-domain calculation was run with three frequency averages and 20 ensemble averages (i.e., cases where a new set of random phases was assigned to the input pressure coefficients). A definite smoothing can be observed at high frequencies for the case with 60 ensemble averages and 10 frequency averages compared to the first case. One question is: What is the effect of the number of averages on the standard deviation of the predicted resistance and reactance at each frequency for very large numbers of ensemble and frequency averages? An abbreviated statistical study was conducted to examine the effects of varying random seed and increasing the number of frequency and ensemble averages.

Consider first the resistance. Figure 5-14 shows a plot of the resistance predicted by the time-domain model with calculated standard deviations at each frequency plotted as error bars. For this case 60 ensemble averages, 10 frequency averages, and a random seed of 5069 were used. Note the rapid increase in standard deviation above 10,000 Hz.

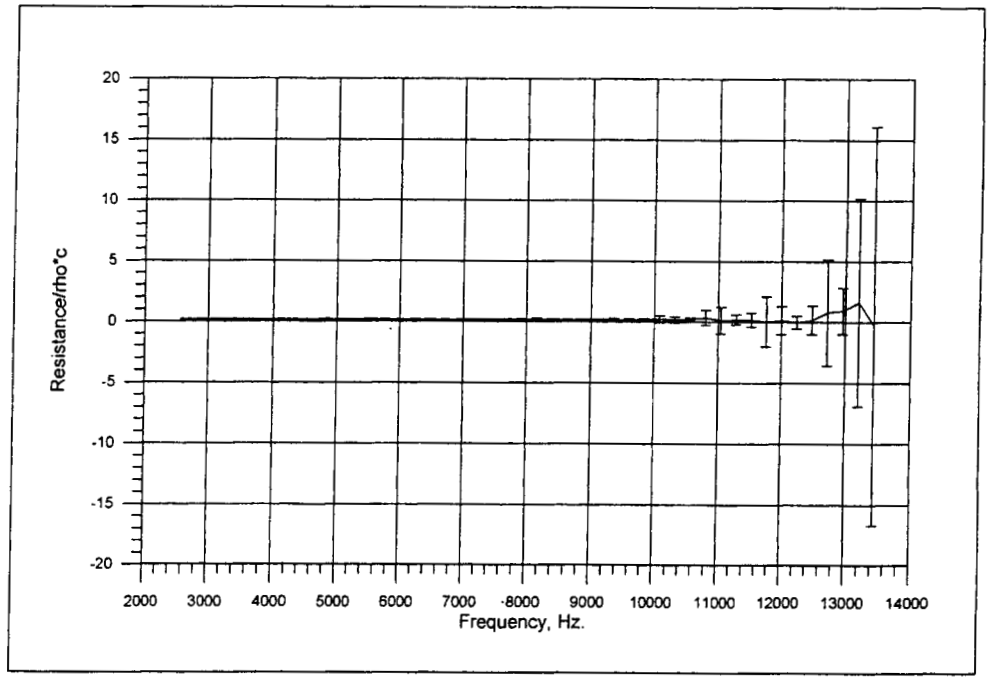

Figure 5-14. Resistance predicted by time-domain model showing standard deviation. 60 ensemble averages, 10 frequency averages, random seed = 5069.

Figure 5-15 compares the resistance standard deviation as a function of frequency for cases where the ensemble averages were held constant at 60, and the seed was held constant at 5069, but the number of frequency averages was set at 3 and at 10. Note a slight decrease in the magnitude of the standard deviation for all but the last two frequencies. This indicates that the deviations may be decreasing with increasing statistical averaging. Little difference in the behavior of the standard deviation is found when only the random seed is changed.

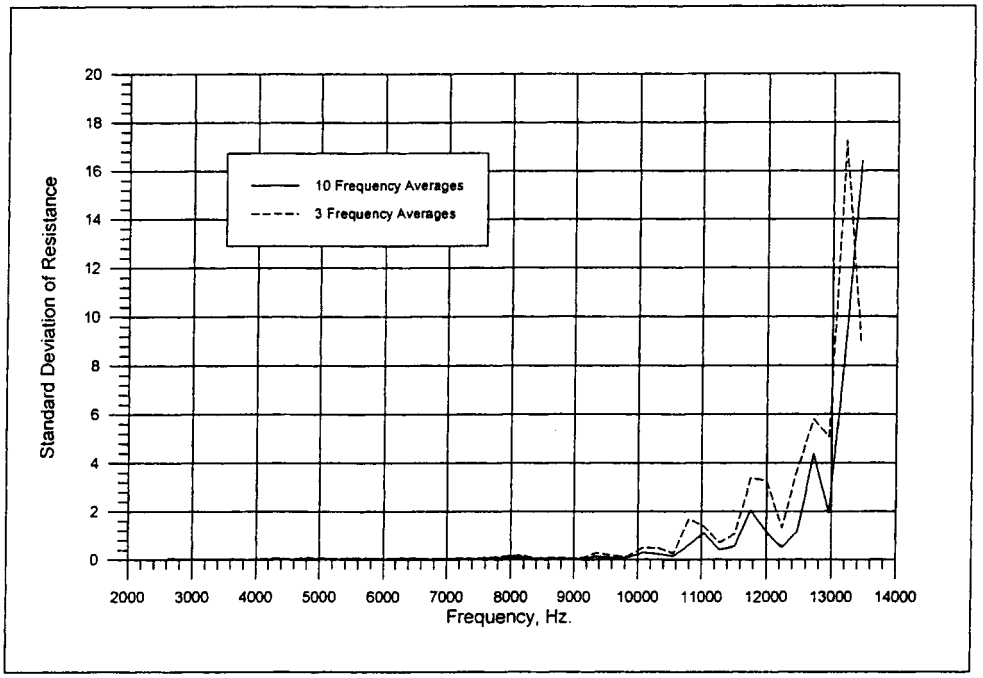

Figure 5-15. Comparison of resistance standard deviations when number of frequency averages is increased from 3 to 10, using 60 ensemble averages and for the random seed = 5069.

Figures 5-16 and 5-17 show corresponding charts for the reactance and reactance standard deviation. Again, 60 ensemble averages, 10 frequency averages, and a random seed of 5069 were used for the reactance chart, and the reactance standard deviation chart compares 3 frequency averages and 10 frequency averages. As in the case of the resistance, increasing the number of frequency averages from 3 to 10 did have a noticeable effect on decreasing the magnitude of the reactance standard deviations at high frequencies, except at the highest frequency.

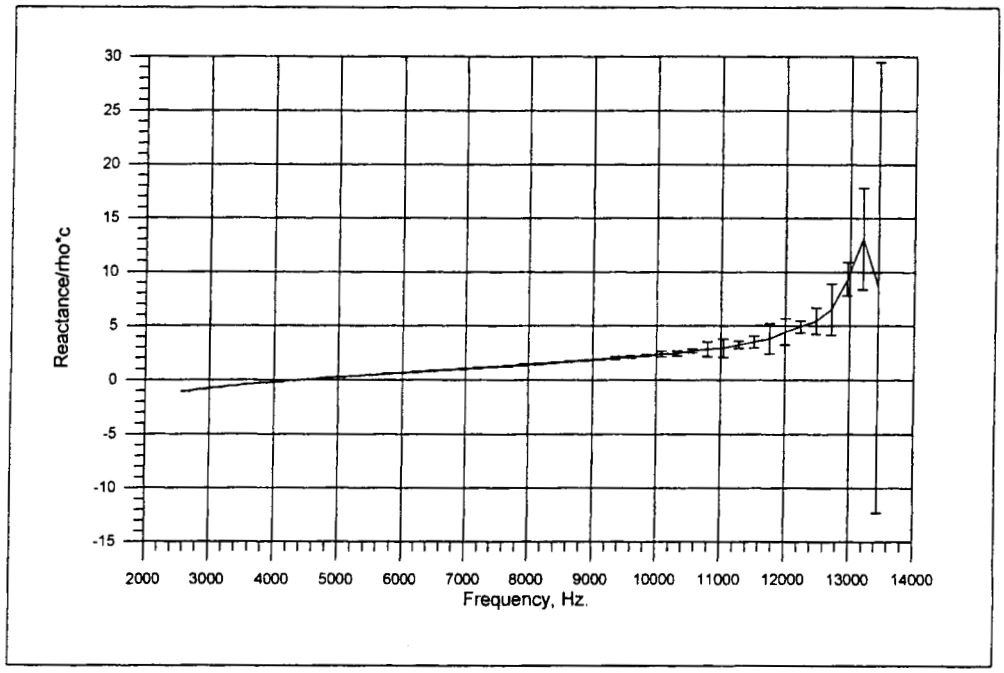

Figure 5-16. Reactance predicted by time-domain model showing standard deviation. 60 ensemble averages, 10 frequency averages, random seed = 5069.

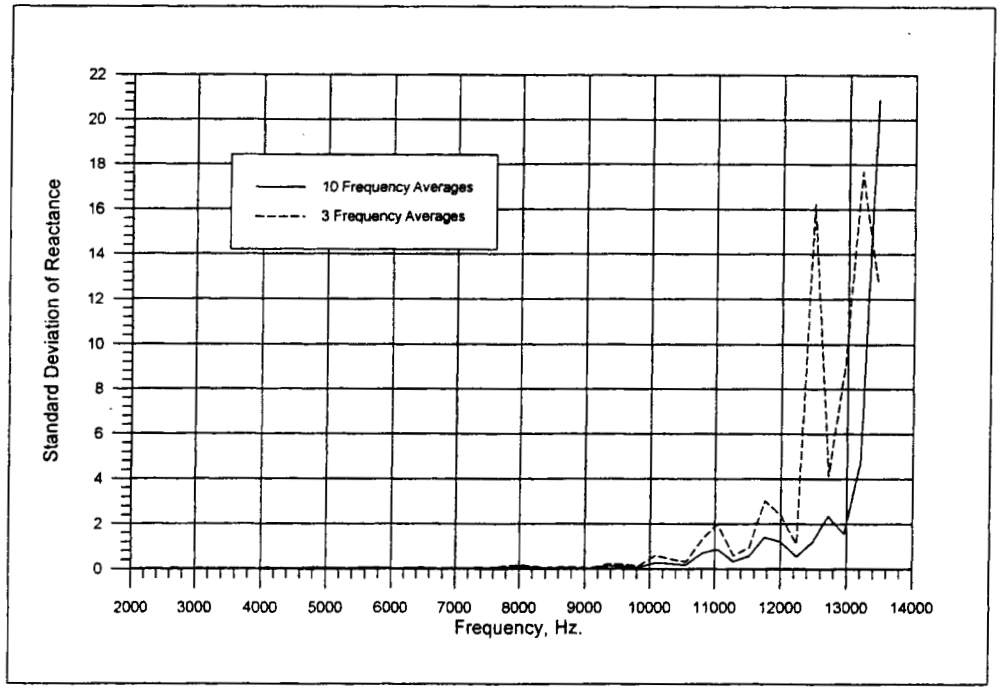

Figure 5-17. Comparison of reactance standard deviations when number of frequency averages is increased from 3 to 10, using 60 ensemble averages and for the random seed = 5069.

A final time-domain prediction run was made for which the number of ensemble averages was increased to 90 and the number of frequency averages was increased to 32. The run took about 10 hours on a Pentium 166 PC. The results are shown in Figure 5-18, which compares the time-domain prediction with the frequency-domain prediction and the measured data. An appreciable smoothing of the high frequency prediction can be noted for the time-domain data, indicating that a sufficiently large number of averages will remove the high frequency variation.

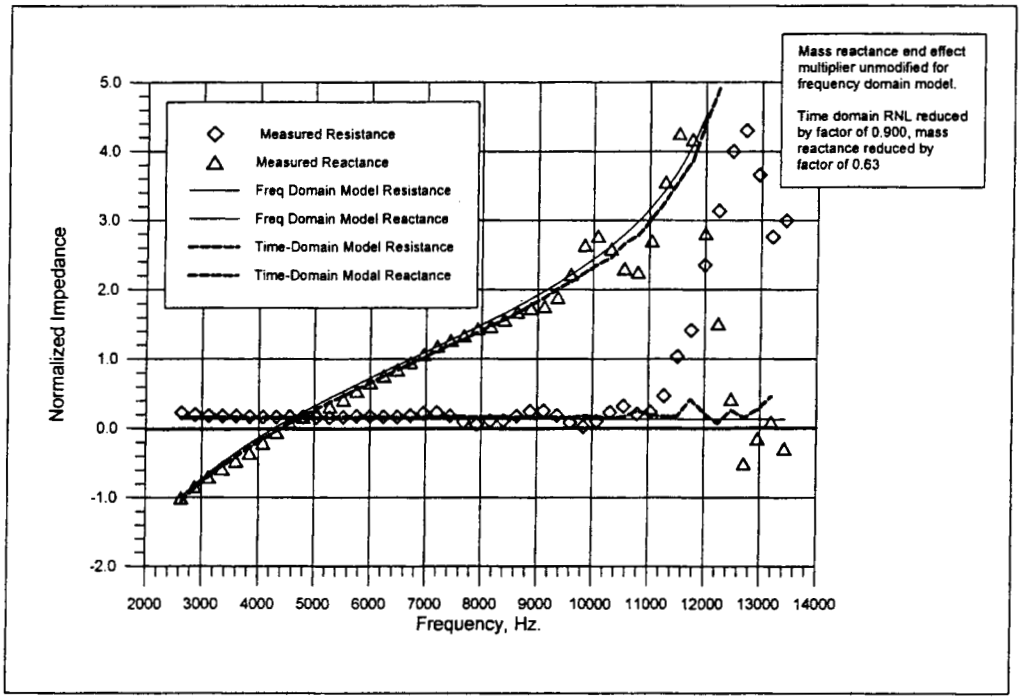

Figure 5-18. Comparison of predicted and measured impedance for 8.0% facesheet resonator for adjusted time-domain case, using 60 ensemble averages and 32 frequency averages.

An interesting comparison can be made between the pressure excitation spectrum in SPL, dB, and a similar spectrum defined for the acoustic velocity. If we let the reference velocity be that rms velocity which would give an impedance of 1.0 ρc when p is p_{ref} = 0.0002 dynes/cm^2, and, if we arbitrarily take ρc = 42.0, then

$$u_{ref} = \frac{p_{ref}}{\rho c} = 4.7619E-6 \qquad cm/sec \tag{5-10}$$

and the Sound Velocity Level, SVL, dB, can be defined as

$$SVL = 20\log_{10}\left(\frac{u_{rms}}{u_{ref}}\right) \tag{5-11}$$

Figure 5-19 shows a comparison between SPL and SVL as a function of frequency (note that the amplitudes are in different units, but the shapes of the spectra can be compared).

The velocity achieves high amplitudes relative to the pressure in the frequency region where the reactance is near zero, as expected. Note, however, that the velocity drops off more rapidly at high frequencies than the pressure. It is possible that the small velocities at high frequencies lead to numerical accuracy problems in the computation. It could also be possible that the small velocities are in evidence for the measurement, causing measurement problems in the same frequency range.

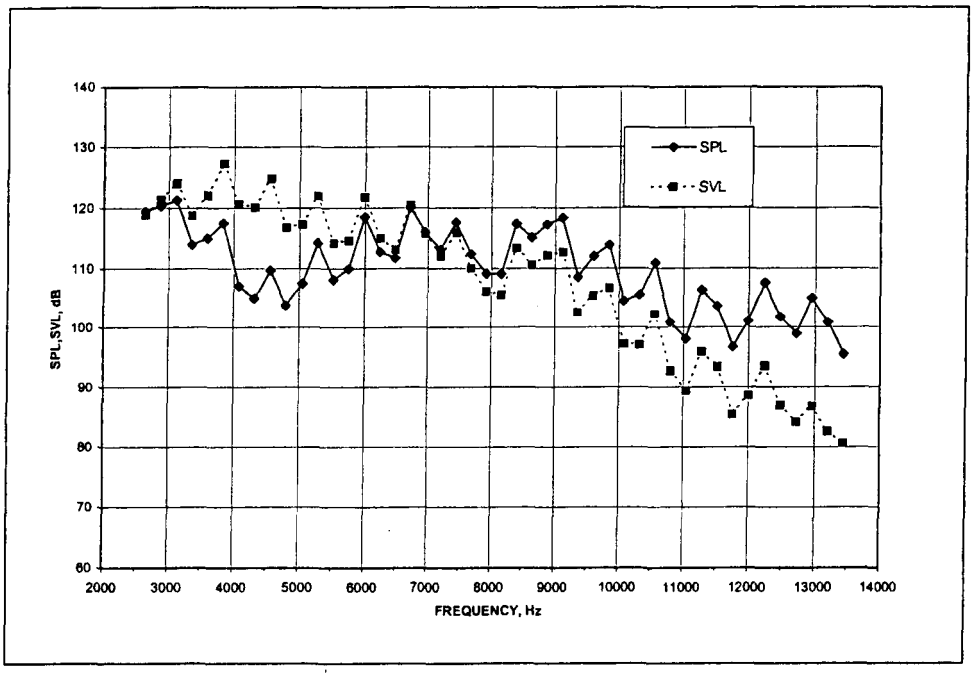

Figure 5-19. Comparison of SPL of excitation pressure and SVL of resulting faceplate acoustic velocity for 8% porosity SDOF resonator.

5.5.5 One-Fifth Scale Wiremesh Faceplate SDOF with Broadband Excitation

The perforated plate resonator program was modified by changing the mass reactance model to represent that of a wiremesh facesheet, and the program was renamed ZWM2. The resistance model, with coefficients for linear and nonlinear resistance, is unchanged, but the mass reactance model was modified to replace the orifice mass reactance coefficient with an arbitrary constant times the wavenumber. The wiremesh mass reactance constant must be obtained from measurement.

Figure 5-20 shows the measurement of reactance of a one-fifth scale, 0.508 cm (0.2 in.) deep cavity covered by a 2 ρc linear faceplate. The wiremesh is bonded directly to the honeycomb backing with no intervening perforated sheet for support. The mass reactance is extracted by subtracting -cot(kL) from the measured reactance, and a linear curve fit is made to the resulting mass reactance as a function of frequency.

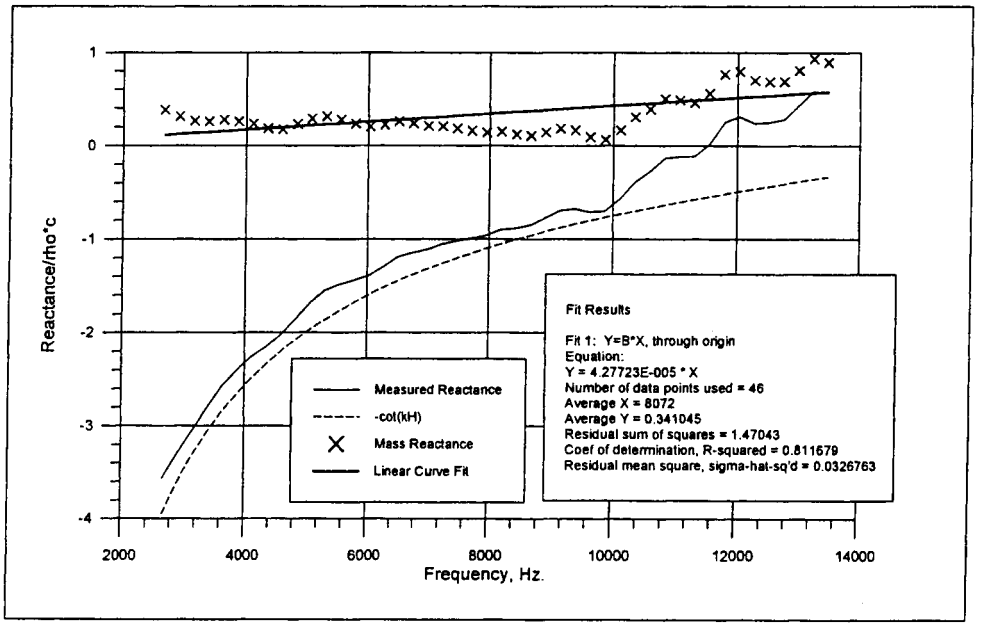

Figure 5-20. Extraction of mass reactance for wiremesh over honeycomb resonator.

Figure 5-21 shows the comparison of predicted and measured impedance in this case, with no adjustments to the time-domain model resistance or reactance. The resistance is modeled using R_{LIN} = 76.77 cgs Rayls and R_{NL} = 0.06342 cgs Rayls per cm/sec. A better fit to the reactance could have been obtained if the mass reactance were obtained from the measured data using a higher order curve fit than the assumed linear model. The resistance might have been predicted more closely by adjusting the ratio between the linear and nonlinear coefficients. However, without physical rationale for either procedure, no adjustments were made, and the match between predicted and measured impedance is as good as can be expected without further improvement in the facesheet lumped impedance models.

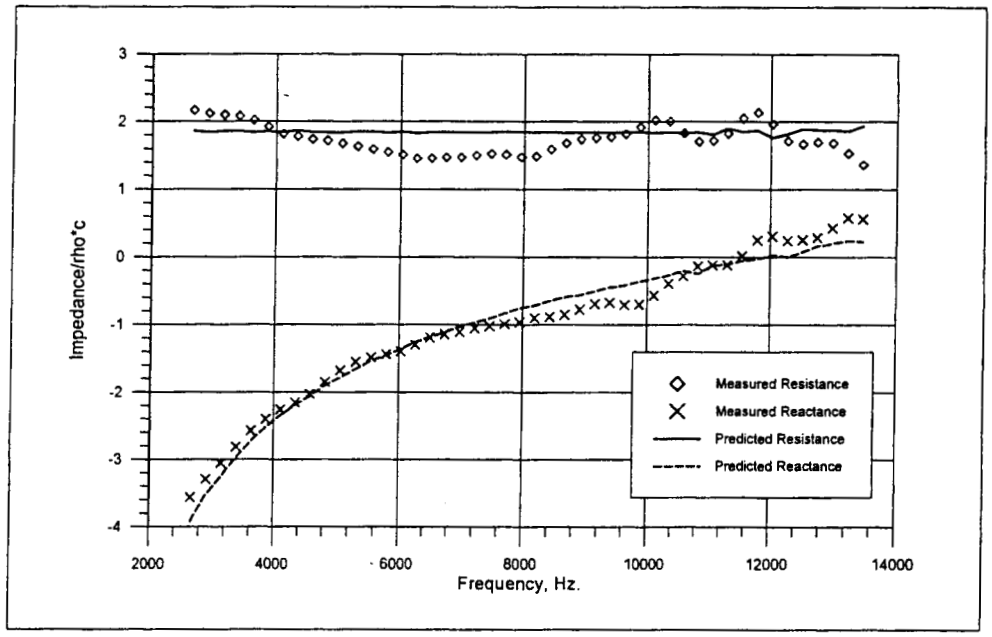

Figure 5-21 Comparison of predicted and measured impedance for wiremesh faceplate SDOF resonator with 0.508 cm cavity depth.

5.6 Conclusions and Recommendations

5.6.1 Summary of Results

The time-domain impedance prediction model has been upgraded by incorporating the dispersion-relation-preserving 7-point stencil finite difference, 4-level time marching scheme of Tam. The upgrade did not materially change the results obtained from the simpler 3-point stencil scheme used previously, but it does converge using far fewer grid points per wavelength and gives confidence that the entire method is computing correctly.

In order to obtain agreement between the time-domain impedance prediction method and the frequency-domain method and the measured data, it is necessary to make adjustments to the effects of nonlinear resistance and mass reactance for the time domain model. At present, these adjustments to the resistance and reactance parameters must be made by hindsight, and further effort is needed to provide the fluid mechanical rationale for appropriate resistance and mass reactance models for application to the time-domain prediction.

The time domain model has been shown to be capable of predicting the measured impedance closely up to frequencies of 13,000 Hz., which was the limit of measurement data currently available for making comparisons. It is concluded that the time-domain model meets the objective of correctly determining the effects of variations in the spectral shape and level of the excitation acoustic pressure on the nonlinear resonator impedance.

5.6.2 Time-Domain versus. Frequency-Domain Impedance Models

There an apparent need to replace the current frequency-domain model assumptions for nonlinear resistance for the time-domain model. The frequency domain model assumes that to incorporate the measured DC flow resistance into the frequency domain model one must identify the steady DC flow velocity with the overall rms acoustic velocity (integrated over all frequencies). This gives a constant predicted resistance value as a function of frequency that provides a good average match to measured perforated plate resistances with broadband excitation, but is unable to predict small variations in the measured resistance that are apparently effects of excitation pressure spectral shape.

The frequency-domain mass reactance model, on which the time-domain model was based, generally appears to over-predict the mass reactance of perforated plate resonators under broadband excitation, so that both the frequency-domain and time-domain models require adjustments to provide a close match to measured reactance data. The time domain model appears to require more reduction of mass reactance than the frequency-domain model. The development of an advanced time-domain mass reactance model that includes nonlinear effects of acoustic velocity might lead to improvements in this area.

The time-domain model does predict variations of acoustic impedance in spectral shape, although it has not been proven authoritatively that the predictions match spectral variations in the measured resistance data. Several steps are needed to advance the model further.

First, it would be helpful to have additional, carefully-conducted normal incidence impedance tube measurements that included determination of the standard deviations of the measurement. The measurement variations that are used to derive the standard deviations should be more than ostensibly identical "repeat" testing, which would be more useful in determining systematic variations. It would be useful to introduce test variations that randomly varied the relative phasing of the input spectrum frequency components. This might occur naturally through temperature variations or tube/source coupling geometry modifications, but it might be more easily introduced by electronically modifying the signal driving the loudspeaker. Special electronic equipment or data processing computer capabilities might be required to provide variable random phasing to individual signal frequency components.

Second, improvements are needed in the fluid mechanical models of time-domain resistance and reactance. This might be achieved using steady or quasi-steady CFD computations of the fluid flow through an orifice, if these could be cast in a form that allowed derivation of the acoustic resistive and inertial properties of the flow. In the past, understanding of the oscillating acoustic flow through an orifice has been advanced by using simple incompressible fluid flow models in a similar manner. Advanced CFD programs are now available that might be able to incorporate the effects of vorticity, compressibility, and turbulence for the various orifice flow regimes.

5.7 References

[1] Kraft, R. E., "Acoustic Treatment Scaling Methods. Volume 4: Numerical Simulation of the Nonlinear Acoustic Impedance of a Perforated Plate Single-Degree-of-Freedom Resonator Using a Time-Domain Finite Difference Model", NASA CR-1999-209120/ Vol. 4, April 1999.

[2] Tam, C. K. W. and Webb, J. C. "Dispersion-Relation-Preserving Finite Difference Schemes for Computational Acoustics", Journal of Computational Physics, 107, 1993, pp. 262-281.

[3] Tam, C. K. W., "Computational Aeroacoustics: Issues and Methods", AIAA 95-0677, Jan. 1995.

[4] Tam, C. K. W., Webb, J. C., and Dong, Z., "A Study of the Short Wave Components in Computational Acoustics", Journal of Computational Acoustics, Vol. 1, No. 1, (1993), pp. 1-30.

[5] Tam, C. K. W., Dong, Z., "Wall Boundary Conditions for High-Order Finite-Difference Schemes in Computational Aeroacoustics", Theoret. Comput. Fluid Dynamics, Vol. 6, (1994), pp. 303-322.

[6] Tam, C. K. W. and Auriault, L., "Time-Domain Impedance Boundary Condition for Computational Aeroacoustics", AIAA 96-1662, May, 1996.

[7] Motsinger, R. E. and Kraft, R. E., "Design and Performance of Duct Acoustic Treatment", Chapter 14 in Hubbard, H. H., ed., *Aeroacoustics of Flight Vehicles: Theory and Practice. Volume 2: Noise Control*, NASA Reference Publication 1258, Vol 2., 1991 (currently available from ASA), p. 186.

6. UPS Nacelle Liner Design

6.1 UPS Nacelle Aeroacoustic Parameters

There are three different fan configurations to be considered for the GEAE Universal Propulsion Simulator (UPS) nacelle acoustic treatment design. The first fan configuration is the baseline which has high vane count and unswept vanes. The second fan configuration has low vane count and unswept vanes. The last fan configuration has low vane count and swept vanes.

In each fan configuration, the tone and broadband noise mode distribution are varied, thereby requiring different treatment designs to suppress acoustic energy. The first objective of the study was to demonstrate an analytical approach to design the UPS nacelle acoustic treatment. The second objective was to establish the correlation between the full-scale liner and its 1/5 sub-scale liner under design conditions. Due to limitations in program scope, the baseline inlet was picked as a demonstration candidate.

The aeroacoustic input parameters for the assumed full-scale impedance design analysis are listed in Table 6-1.

Table 6-1. Aeroacoustic input parameters for UPS full-scale condition design impedance study.

Engine/Nacelle Parameters		Fan Blades 22	Fan Diameter 9.17 ft	Treated Length 2.02 ft
Fan Speed RPM		BPF (1/3 OB) Hz	2BPF (1/3 OB) Hz	3BPF (1/3 OB) Hz
APP	1560	572 (630)	1144 (1250)	2288 (2500)
C/B	2188	802 (800)	1605 (1600)	3210 (3150)
T/O	2530	928 (1000)	1855 (2000)	3710 (4000)
In-duct Mach #		Inlet	Fan Case	Aft-fan
APP		0.3	0.29	0.32
C/B		0.45	0.39	0.43
T/O		0.59	0.46	0.49

Boundary layer displacement thickness BL = 0.176 inch
Boundary layer Thickness B = 1.41 inch (assume 1/7 power)

6.2 Inlet Liner Design Approach

An improved approximation method originally developed by Dr. E. J. Rice was used for this analysis. Since the mode distribution is unknown, equal energy per mode at far-field is assumed. The analysis is conducted by first finding the treatment design for the full scale engine. The design process has two steps:

1. Generate far-field power attenuation contours versus acoustic impedance for approach cutback, and takeoff operating conditions at critical frequencies. The far-field distance, adjusted by the flight path (see Figure 6-1), and air absorption are also considered in the calculation. In this demonstration, the flight path angle (i.e. -3 degrees for approach and 5 degrees for cutback), and sideline distance are not applied. The optimum design impedance at each critical frequency will be obtained from the attenuation contours.

2. Design acoustic liner configuration to best match desired impedance at both approach and cutback conditions. Since takeoff noise is dominated by aft fan and jet noise, the inlet impedance at take off condition is not a critical design issue.

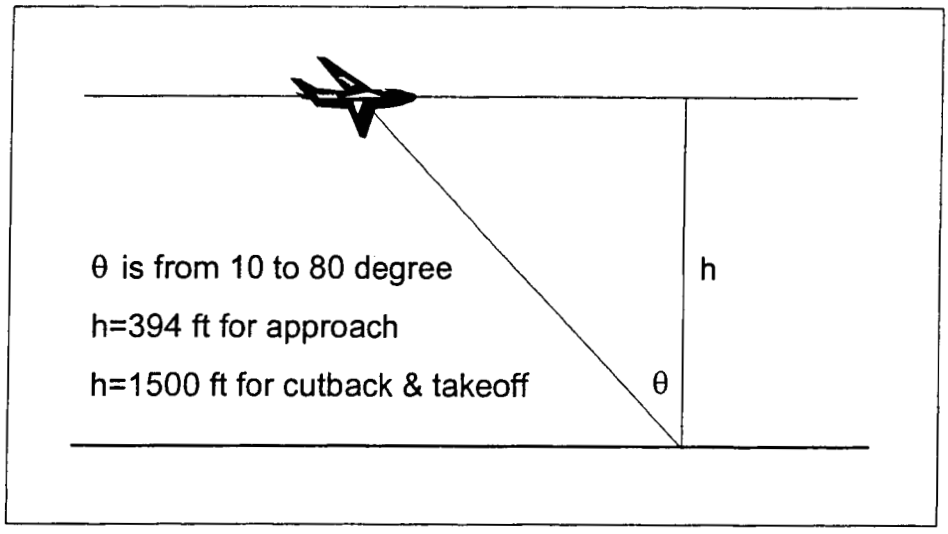

Figure 6-1. Definition of aircraft flight path for attenuation calculations.

Computer codes developed in-house at BFGoodrich are used in this analysis. The computer codes include impedance prediction, liner design process, and far-field attenuation estimate.

6.3 Optimum Impedance and Liner Design

The full scale inlet impedance of approach, cutback, and takeoff conditions, which are shown in Figures 6-2, 6-3, and 6-4, were estimated from attenuation contour plots that plotted lines of constant suppression in the complex impedance plane. Within the limitations of the program scope, these designs will be denoted as "optimum". The candidate liner's impedance at each operating condition should closely match its optimum impedance at the critical frequencies. Since the takeoff noise is dominated by the aft-fan and jet noise, this impedance matching process will concentrate on approach and cutback conditions.

The baseline fan design has a cut-off BPF (Blade Passage Frequency) tone for approach. As a result, the critical design frequencies for approach cover from 2BPF to 5BPF tones (and broadband noise) with frequency range from 1250 to 3150 Hz. For cutback, the critical design frequencies cover from BPF to 3BPF tones (and broadband noise) with a frequency range from 800 to 3150 Hz.

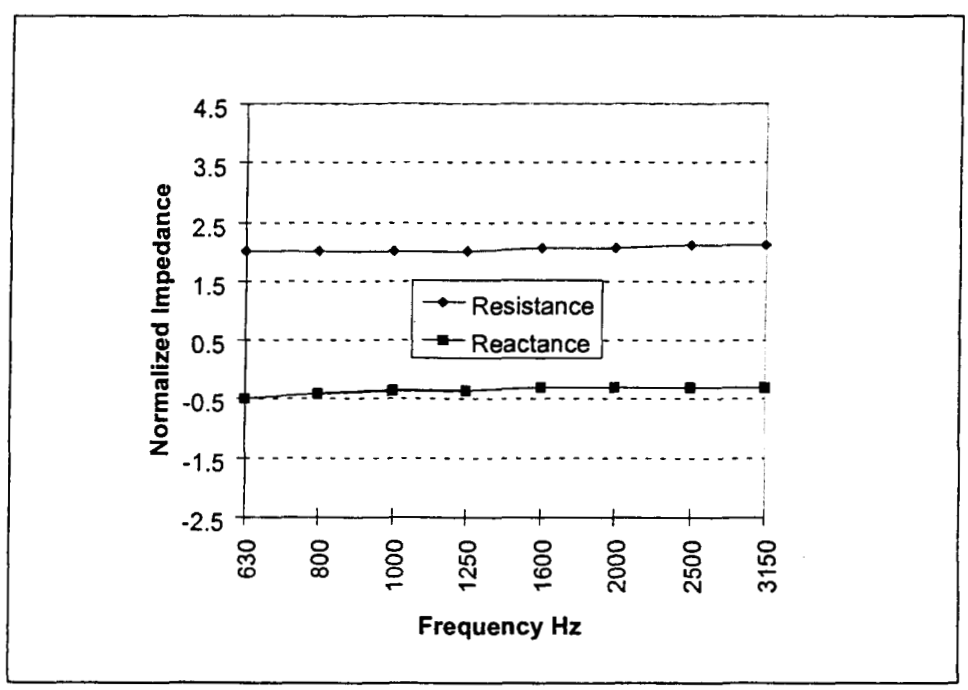

Figure 6-2. Optimum impedance at approach condition based on power attenuation integrated from 10° to 80° at 394 ft flyover distance (see Figure 6-1.).

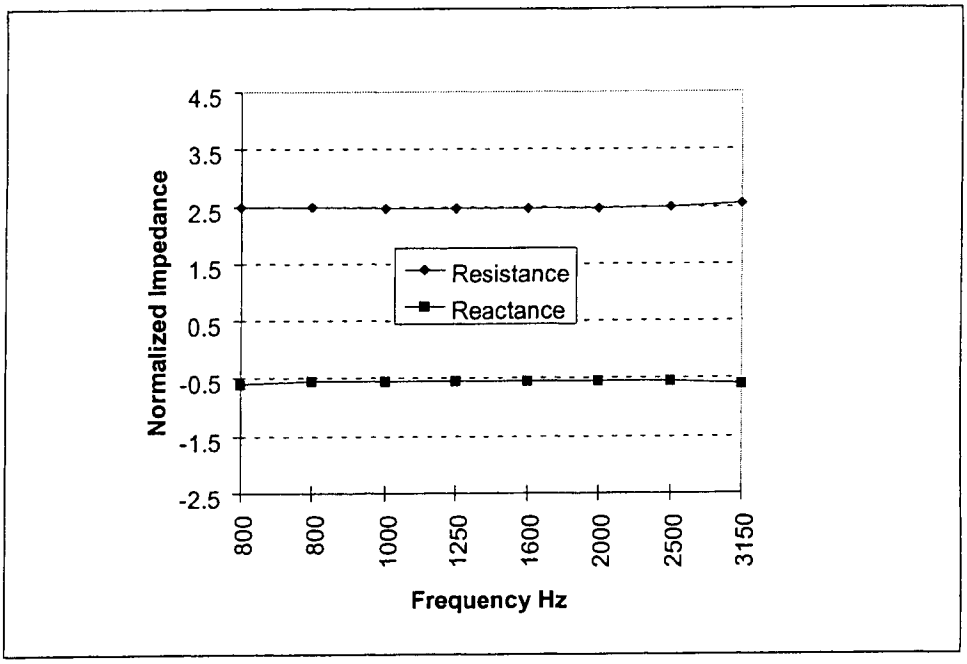

Figure 6-3. Optimum impedance at cutback condition based on power attenuation integrated from 10° to 80° at 1500 ft fly over distance.

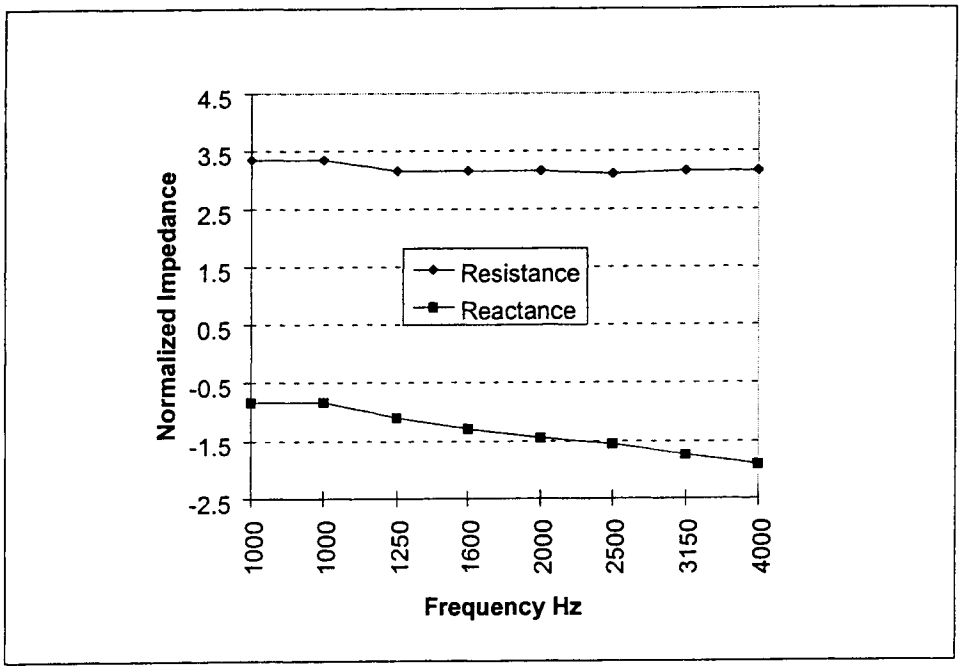

Figure 6-4. Optimum impedance at takeoff condition based on power attenuation integrated from10° to 80° at 1500 ft fly over distance

Since the optimum impedance curves shown in Figures 6-2 and 6-3 have very flat characteristics, double-degree-of-freedom (DDOF) liners, which have broader bandwidth than single-degree-of-freedom (SDOF) liners, are selected as the preferred candidate design. After several iterations, a DDOF liner configuration was defined as shown in Table 6-2.

Figures 6-5 and 6-6 show the estimated full-scale liner impedance along with target optimum values at approach and cutback conditions. Figure 6-7 shows the liner far-field power attenuation versus frequency from 500 Hz to 5000 Hz (based on Figure 6-1 flight path definition).

Table 6-2. Proposed Full-Scale DDOF Optimum Liner Design

Full-Scale DDOF Liner Configuration
Face Sheet: Perforate plate • 10% Open area ratio • 0.04 inch hole diameter • 0.032 inch plate thickness • 0.36 inch core depth (3/8" cell) Septum: Linear mesh • R(105)=95 Rayls • NLF^{+} =1.3 • 1.62 inch core depth (3/8" cell) * R(105) is CGS DC flow resistance measured at flow speed of 105cm/sec * NLF = R(200)/R(20). R(200) and R(20) are flow resistance at flow speed at 200 cm/sec and 20 cm/sec respectively.

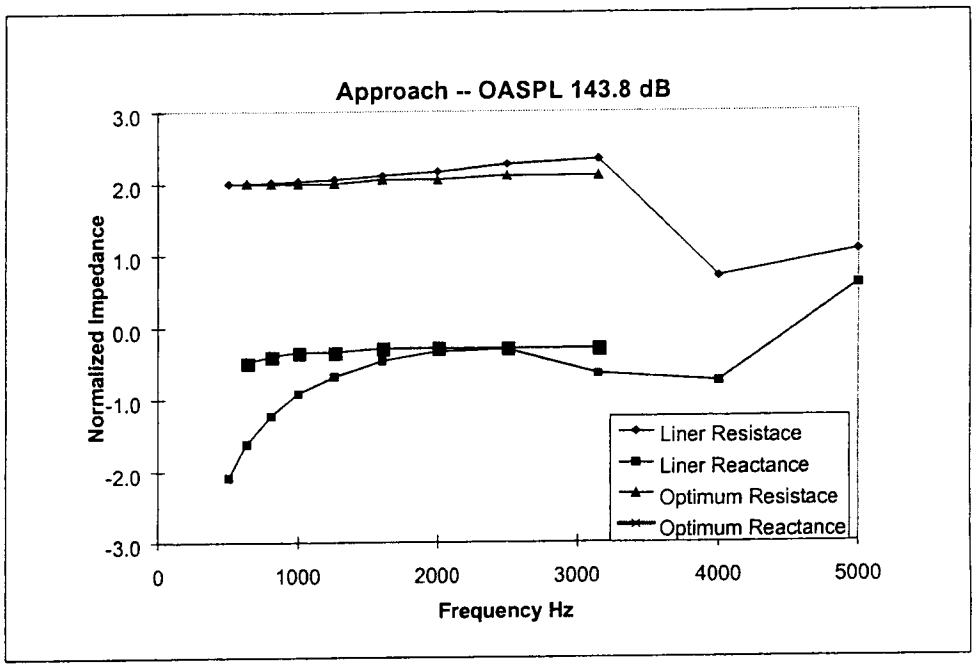

Figure 6-5. Full-scale target DDOF liner impedance for approach condition.

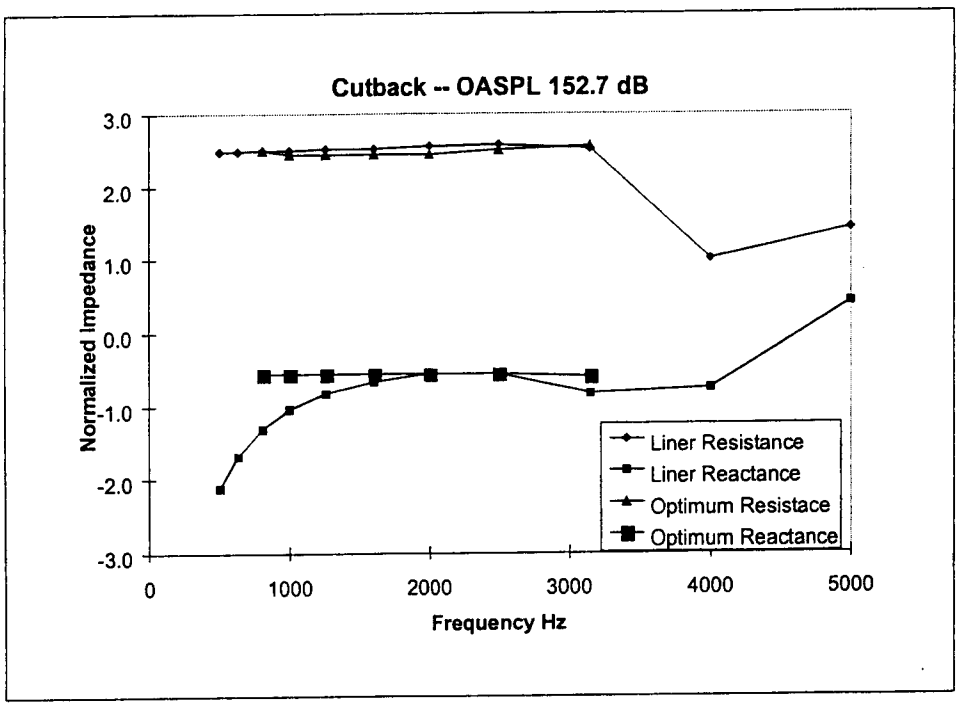

Figure 6-6. Full-scale target DDOF liner impedance for cutback condition.

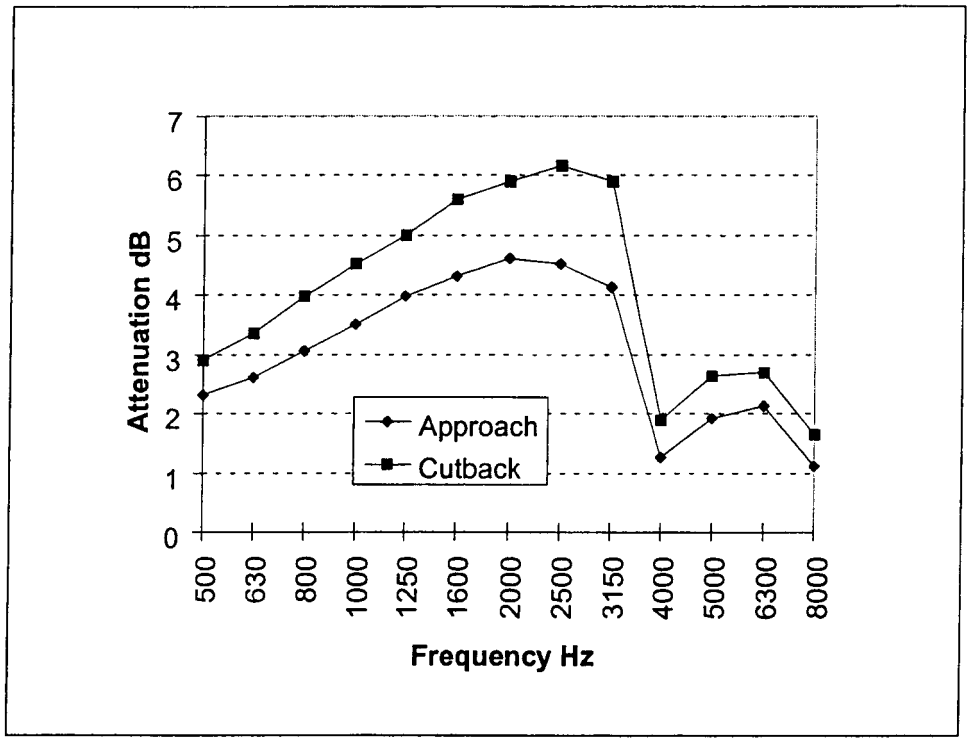

Figure 6-7. Farfield power attenuation for full-scale DDOF liner design at approach and cutback.

In the final design, acoustic performance will be based on flight noise EPNdB results. In any future study, this preliminary liner configuration could be used as an initial value for further iterations. A minor adjustment of the liner configuration may be required to obtain a maximum EPNdB attenuation. The complete design method is shown in Figure 6-8.

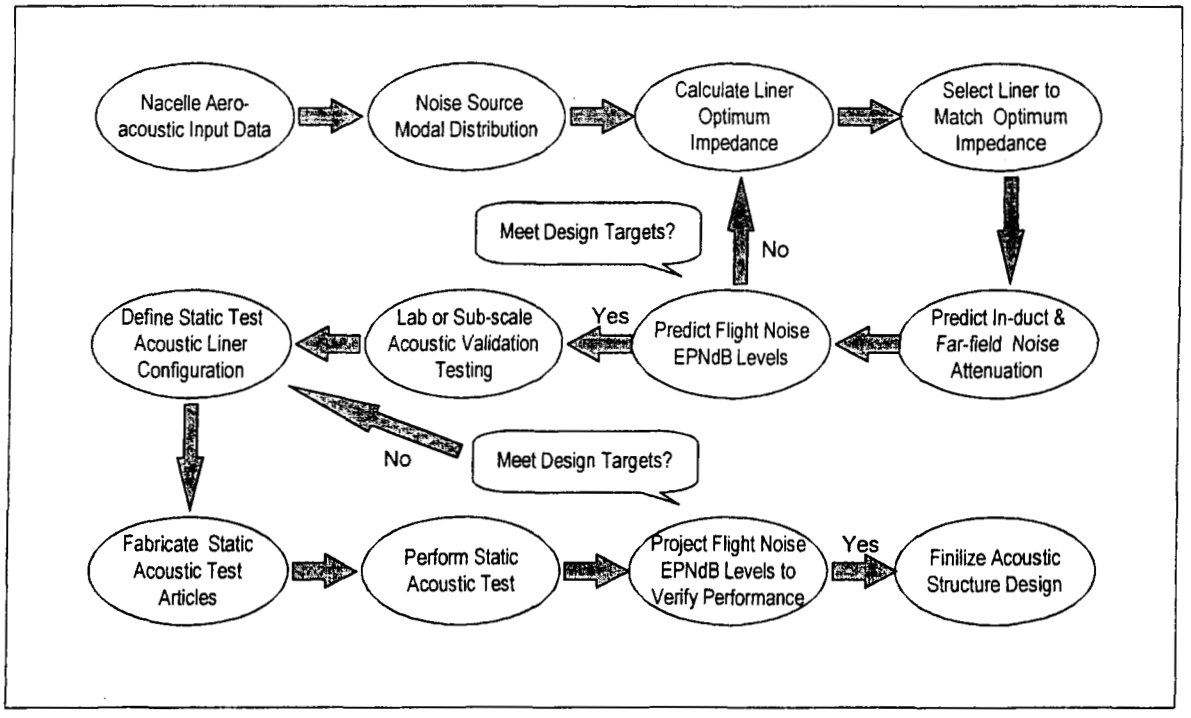

Figure 6-8 Methodology for acoustic liner design and validation.

6.4 1/5 Scale DDOF Acoustic Liner Configuration

Use of 1/5 scale treatment on the 22" UPS rig to simulate full-scale performance is a challenge. First, several parameters such as grazing flow boundary layer and septum mesh can not be scaled. In addition, the acoustic impedance model for perforated plates with grazing flow has not been fully validated, especially at frequency above 10 kHz. To overcome these problems, a DDOF linear system (mesh surface and septum), whose performance can be precisely predicted at higher frequency ranges, is chosen as the 1/5 scale liner candidate.

The method to simulate full-scale treatment is to match the impedance value at each operating condition rather than to scale down the actual geometry. For this reason, a single sub-scale liner configuration may not be adequate to represent the full-scale liner. In this study, two sub-scale liner configurations listed in Tables 6-3 and 6-4 are used to simulate the full-scale liner at approach and cutback conditions. As shown in Figures 6-9 and 6-10, the impedance curves between the full-scale and sub-scale liners match well in the critical frequency range. In addition, these two sub-scale liners have reasonable material specifications (i.e., mesh type, septum resistance, core depth, and cell size), which permits fabrication at BFGoodrich without major difficulties.

Similar analysis can be applied to the fan case and aft fan liners. This evaluation demonstrates that the scaled treatment method developed in this program, combined with advanced liner optimization process, as well as adequate fabrication skills, can be used to design sub-scale treatment for the UPS rig or other models.

Table 6-3. 1/5 scale DDOF liner design for approach.

1/5 Scale DDOF Liner for Approach
Face Sheet: Linear mesh • R(105)=44 Rayls • NLF =1.2 • 0.12 inch core depth (3/16" cell) Septum: Linear mesh • R(105)=85 Rayls • NLF =1.3 • 0.22 inch core depth (3/16" cell)

Table 6-4. 1/5 scale DDOF liner design for takeoff.

1/5 Scale DDOF Liner for Cutback
Face Sheet: Linear mesh • R(105)=50 Rayls • NLF =1.2 • 0.085 inch core depth (3/16" cell) Septum: Linear mesh • R(105)=95Rayls • NLF =1.3 • 0.22 inch core depth (3/16" cell)

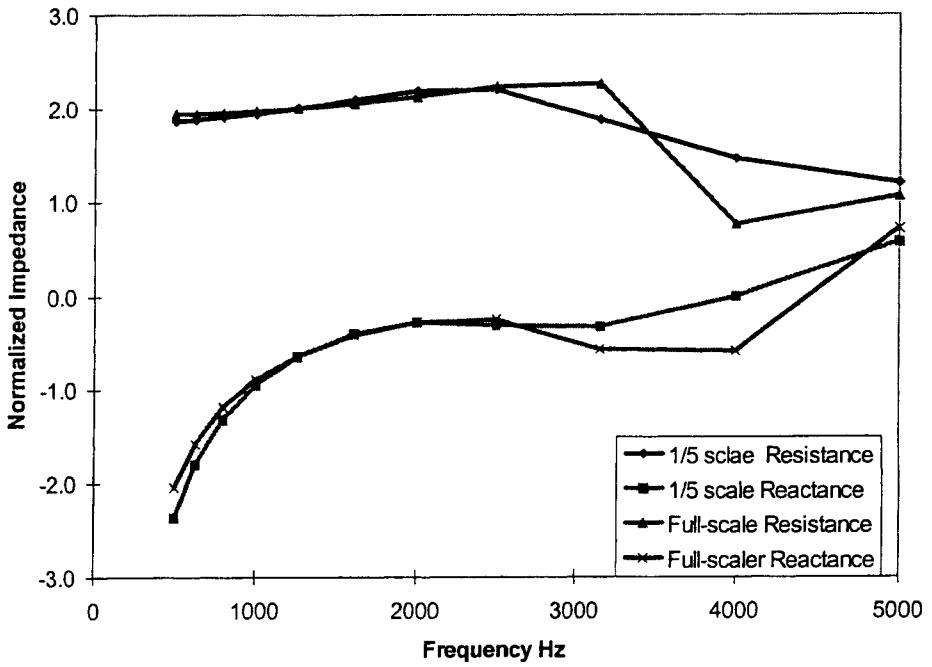

Figure 6-9. Predicted impedance curves for proposed 1/5 scale DDOF liner design at approach, 143.8 dB OASPL.

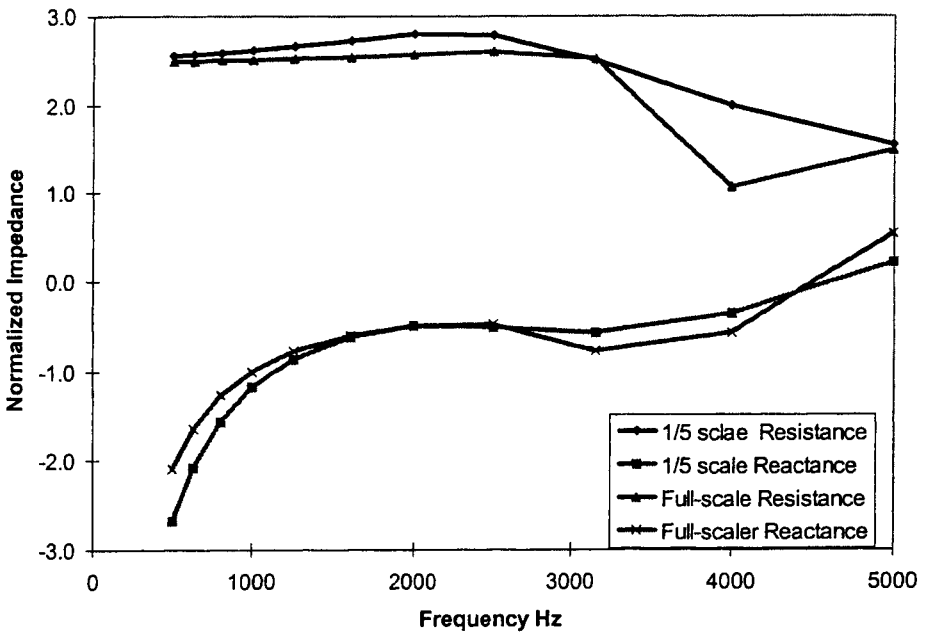

Figure 6-10. Predicted impedance curves for proposed 1/5 scale DDOF liner design at cutback, 152.7 dB OASPL.

6.5 SDOF Treatment Designs

Although the DDOF optimized treatment design is aimed at achieving a scale model liner that represents a full-scale liner design in 1/5 scale size, building the double layer liner to sufficient precision presents a substantial challenge to the model builder. The advantage is that only a single scale model suppression test would be required to characterize the performance of the treatment design.

A more conservative approach would be to construct several single layer liners of different depths that gave a range of reactance values over the design frequency range of interest. For the 22 inch diameter UPS vehicle with 22 fan blades, Table 6-4 gives the range of operating conditions expected:

Table 6-4. Operating characteristics of UPS fan with 22 blades.

Scale Model Parameters	Approach	Cutback	Takeoff
Fan RPM	7800	10490	12650
Blade-Passing Frequency, Hz	2860	3846	4638
Tip Relative Mach Number	0.743	1.072	1.280

These are the operating conditions of the UPS vehicle. Given these conditions, the scale model design can be scaled to full-scale by an arbitrary factor, assuming that the aerodynamic performance and the acoustic noise source are perfectly represented by the scale model.

To cover all frequencies of interest between BPF at approach and 3BPF at takeoff, the scale model treatment would have to cover a frequency range of 2800 Hz to 14,000 Hz. Without further data available to make detailed studies of system flyover noise, it is not possible to aim the treatment tuning frequency at any particular value that would maximize reduction in EPNL. The objective of the multiple-configuration SDOF treatment design would be to provide information on the performance of the treatment based on its impedance, where variations are provided in the values of reactance as a function of frequency.

The minimum number of treatment configurations required would be two. Assuming that costs limit the test to two configurations, the question is how to choose the cavity depth and facesheet resistance to provide the most information about suppression performance over the frequency range of interest.

First, with a nearly-linear wiremesh facesheet, almost any resistance could be achieved between 1.0 ρc and, say, 3.0 ρc, where the lower value would be appropriate to an exhaust duct treatment design, and values around 2.0 ρc would be more appropriate to an inlet design. Assuming only two test configurations, only one chance is provided for the choice of the liner resistance, and it would be held constant for both liner configurations.

Two liner depths are proposed, 0.225 inches and 0.45 inches. While thin, these liners should not be exceptionally difficult to fabricate in a single-layer design. Figure 6-11 shows plots of the impedance curves for the two liner designs. The resistance, in both cases, is arbitrarily chosen to be 1.5 ρc. This can easily be modified by varying the wiremesh weave, taking into account the nonlinearity factor and expected SPL spectrum in the duct.

The heavy box around the reactance curves indicates the "tuning" region for the two liner depths. The depths are chosen to give a reactance between 0.0 and -1.0 over the frequency range from about 2800 to 14,000 Hz. Although additional parametric variations in resistance and reactance would be desirable from an idealistic point-of-view, these limited cases should give an indication of the suppression available over the tuning range of the treatment, and provide guidance for the final full-scale design of the treatment.

The wiremesh treatment designs should have minimal grazing flow effects on impedance. Since high frequency normal incidence impedance tube measurements have been demonstrated to be quite reliable at least up to 12,000 Hz, with a properly-prepared and representative impedance tube treatment sample one should be able to measure the impedance of the liners with some confidence. These impedances can then be scaled easily to any larger scale factor.

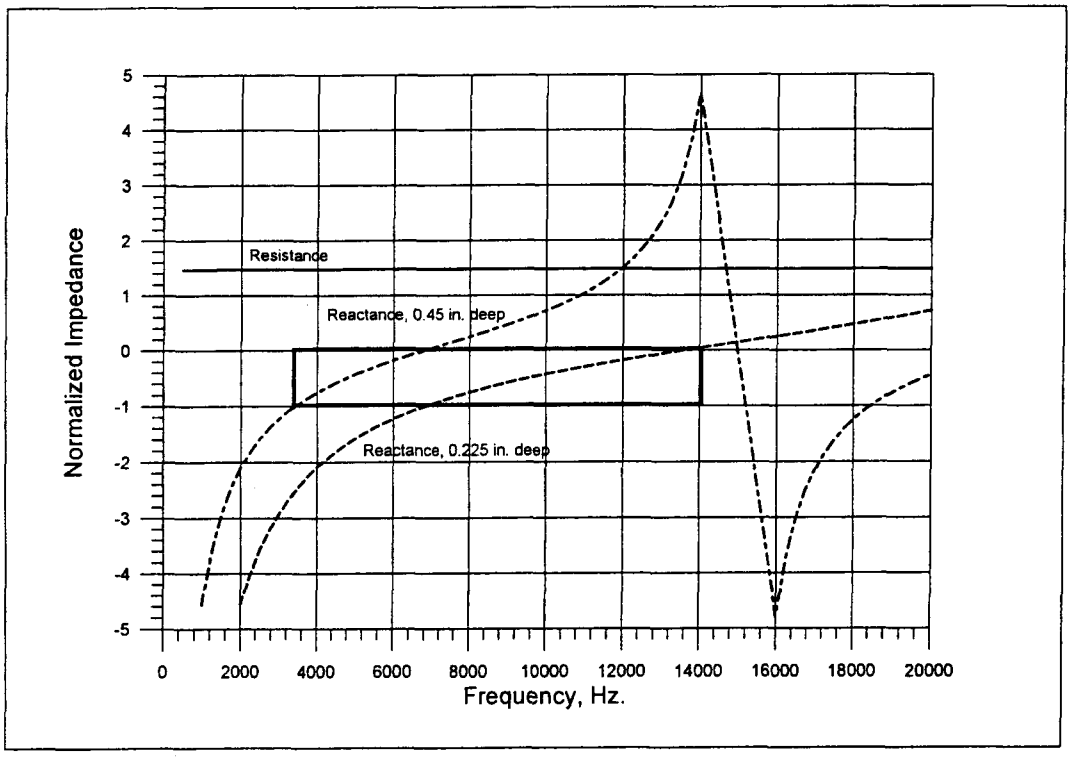

Figure 6-11. Impedance curves for proposed wiremesh SDOF scaled treatment designs.

REPORT DOCUMENTATION PAGE

Form Approved OMB No. 0704-0188

1. REPORT DATE *(DD-MM-YYYY)*	2. REPORT TYPE	3. DATES COVERED *(From - To)*
01- 07 - 2003	Contractor Report	April 97-April 99

4. TITLE AND SUBTITLE

Acoustic Treatment Design Scaling Methods: Phase II Final Report

5a. CONTRACT NUMBER

NAS3-26617

5b. GRANT NUMBER

5c. PROGRAM ELEMENT NUMBER

6. AUTHOR(S)

(1) R.E. Kraft, (2) J. Yu, (2) H.W. Kwan, (3) A.F. Seybert, (3) P. Tathavadekar, and (2) B. Beer

5d. PROJECT NUMBER

5e. TASK NUMBER

25

5f. WORK UNIT NUMBER

781-30-14-01

7. PERFORMING ORGANIZATION NAME(S) AND ADDRESS(ES)

(1) GE Aircraft Engines
1 Neumnn Way MD A411
Cincinnati, OH 45241-6301

(2) BFGoodrich
Mail Stop 107X
850 Lagoon Drive
Chula Vista 91910-2098

(3) Univ. of Kentucky
Mechanical Engineering Department
171 Ralph G Anderson Bldg 0503
Lexington, KY 40506

8. PERFORMING ORGANIZATION REPORT NUMBER

9. SPONSORING/MONITORING AGENCY NAME(S) AND ADDRESS(ES)

National Aeronautics and Space Administration
Langley Research Center
Hampton, VA 23681-2199

10. SPONSOR/MONITOR'S ACRONYM(S)

NASA

11. SPONSOR/MONITOR'S REPORT NUMBER(S)

NASA/CR-2003-212428

12. DISTRIBUTION/AVAILABILITY STATEMENT

Unclassified: Unlimited
Subject Category: 71
Availability: NASA CASI (301) 621-0390 Distribution: Nonstandard

13. SUPPLEMENTARY NOTES

NASA Technical Monitors: L. Clark, T. Parrott, and M. Jones

14. ABSTRACT

The ability to design, build, and test miniaturized acoustic treatment panels on scale model fan rigs representative of full scale engines provides not only cost-savings, but also an opportunity to optimize the treatment by allowing multiple tests. To use scale model treatment as a design tool, the impedance of the sub-scale liner must be known with confidence. This study was aimed at developing impedance measurement methods for high frequencies. A normal incidence impedance tube method that extends the upper frequency range to 25,000 Hz. without grazing flow effects was evaluated. The free field method was investigated as a potential high frequency technique. The potential of the two-microphone in-situ impedance measurement method was evaluated in the presence of grazing flow. Difficulties in achieving the high frequency goals were encountered in all methods. Results of developing a time-domain finite difference resonator impedance model indicated that a re-interpretation of the empirical fluid mechanical models used in the frequency domain model for nonlinear resistance and mass reactance may be required. A scale model treatment design that could be tested on the Universal Propulsion Simulator vehicle was proposed.

15. SUBJECT TERMS

aircraft noise, acoustic treatment, impedance measurement, fan noise suppression, scale models

16. SECURITY CLASSIFICATION OF:			17. LIMITATION OF ABSTRACT	18. NUMBER OF PAGES	19a. NAME OF RESPONSIBLE PERSON
a. REPORT	b. ABSTRACT	c. THIS PAGE			STI Help Desk (email: help@sti.nasa.gov)
					19b. TELEPHONE NUMBER *(Include area code)*
U	U	U	UU	147	(301) 621-0390